MICROSTRUCTURAL MODELLING OF DUAL-PHASE STEELS THROUGH POLYCRYSTALLINE PLASTICITY AT RVE LEVEL

A THESIS SUBMITTED TO
THE GRADUATE SCHOOL OF NATURAL AND APPLIED SCIENCES
OF
MIDDLE EAST TECHNICAL UNIVERSITY

BY

GÖNÜL ÖYKÜ GÜNGÖR

IN PARTIAL FULFILLMENT OF THE REQUIREMENTS
FOR
THE DEGREE OF MASTER OF SCIENCE
IN
AEROSPACE ENGINEERING

AUGUST 2019

Approval of the thesis:

MICROSTRUCTURAL MODELLING OF DUAL-PHASE STEELS THROUGH POLYCRYSTALLINE PLASTICITY AT RVE LEVEL

submitted by **GÖNÜL ÖYKÜ GÜNGÖR** in partial fulfillment of the requirements for the degree of **Master of Science in Aerospace Engineering Department, Middle East Technical University** by,

Prof. Dr. Halil Kalıpçılar _____
Dean, Graduate School of **Natural and Applied Sciences**

Prof. Dr. İsmail Hakkı Tuncer _____
Head of Department, **Aerospace Engineering**

Assist. Prof. Dr. Tuncay Yalçınkaya _____
Supervisor, **Aerospace Engineering, METU**

Examining Committee Members:

Prof. Dr. Altan Kayran
Aerospace Engineering, METU _____

Assist. Prof. Dr. Tuncay Yalçınkaya
Aerospace Engineering, METU _____

Assoc. Prof. Dr. Cihan Tekoğlu
Mechanical Engineering, TOBB UET _____

Assoc. Prof. Dr. Ercan Gürses
Aerospace Engineering, METU _____

Assoc. Prof. Dr. Demirkan Çöker
Aerospace Engineering, METU _____

Date: _____

I hereby declare that all information in this document has been obtained and presented in accordance with academic rules and ethical conduct. I also declare that, as required by these rules and conduct, I have fully cited and referenced all material and results that are not original to this work.

Name, Last Name: GÖNÜL ÖYKÜ GÜNGÖR

Signature :

ABSTRACT

MICROSTRUCTURAL MODELLING OF DUAL-PHASE STEELS THROUGH POLYCRYSTALLINE PLASTICITY AT RVE LEVEL

Güngör, Gönül Öykü
M.S., Department of Aerospace Engineering
Supervisor : Assist. Prof. Dr. Tuncay Yalçınkaya

August 2019, 99 pages

In this work the plasticity, localization and the damage behavior of dual phase steels are investigated through both J2 and crystal plasticity frameworks. For this purpose, Voronoi based Representative Volume Elements (RVE) are created with different martensite volume fractions, which are studied at different constant triaxiality values. The micromechanical and the macroscopic constitutive responses are analyzed in detail for considering various loading conditions and microstructural parameters. The results are discussed in comparison to the ones in the literature and the work is concluded with remarks and outlook.

Keywords: Dual-phase (DP) Steel, Representative Volume Element (RVE), Crystal Plasticity, Triaxiality, Localization

ÖZ

ÇİFT FAZLI ÇELİKLERİN THE SEVİYESİNDE POLİKRİSTAL PLASTİSİTE İLE MİKROYAPISAL MODELLENMESİ

Güngör, Gönül Öykü
Yüksek Lisans, Havacılık ve Uzay Mühendisliği Bölümü
Tez Yöneticisi : Dr. Öğr. Üyesi Tuncay Yalçınkaya

Ağustos 2019 , 99 sayfa

Çift fazlı çelikler mikro seviyede modellenmiş, hasar başlangıcı ile birlikte oluşan bölgesel gerilmeler klasik J2 plastisite ve kristal plastisite kullanılarak incelenmiştir. Farklı martensit hacim miktarlarına sahip çift fazlı çelikler, Voronoi bazlı temsili hacim elemanları (THE) kullanılarak modellenmiş ve üç eksenli gerilmeler deformasyon boyunca sabit tutularak farklı gerilme halleri altında incelenmiştir. Elde edilen sonuçlara bakıldığında çift fazlı çeliklerin genel davranışında önemli bir farklılık görülmemesine rağmen, seçilen yapısal malzeme modeline bağlı olarak mikro seviyede farklılıklar olduğu gözlenmiştir. Klasik J2 plastisite, kristal plastisite ve gerilme halinden kaynaklanan varyasyonlar literatürdeki deneysel ve hesaplamalı bulgular ile tartışılmış ve karşılaştırılmıştır.

Anahtar Kelimeler: Çift Fazlı Çelik, Temsili Hacim Elemanı (THE), Kristal Plastisite, Üç Eksenli Gerilme, Lokalizasyon

To my family...

ACKNOWLEDGMENTS

I would like to express my gratitude to my supervisor, Assist. Prof. Dr. Tuncay Yalçınkaya, for his guidance, suggestions and support throughout my education. I would like to thank him for giving me the opportunity of having this valuable education under his supervision.

I would like to thank Assoc. Prof. Dr. Cihan Tekoğlu for sharing his valuable knowledge with me.

In addition, I would like to thank my colleague Serhat Onur Çakmak for his technical support with crystal plasticity simulations.

Last but not least, I am greatful to my family and my beloved companion for always supporting me and having faith in me. Without them, I would not be able to achieve this much.

TABLE OF CONTENTS

LIST OF TABLES

TABLES

LIST OF FIGURES

FIGURES

CHAPTER 1

INTRODUCTION

Dual-phase steels or DP steels belong to a group of high strength steels that is composed of two different phases. It consists of soft, ductile ferrite and hard, brittle martensite phases. The ferritic phase is in the form of a matrix while martensitic phase is dispersed along ferrite grain boundaries in the form of islands [1], [2]. A schematic illustration of a dual-phase microstructure is shown in Figure 1.1.

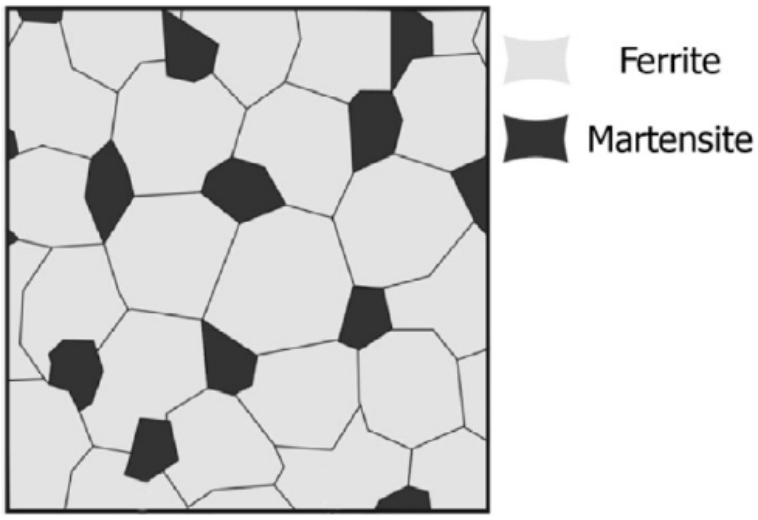

Figure 1.1: Dual-phase microstructure [3].

DP steels were developed in late 1970 and early 1980's when low carbon, low alloy steels were in demand [4]. These features of dual-phase steels have ensured high elongation and high strength with improved formability, fatigue and crash resistance with an addition of being light and affordable [2]. The aforementioned attributes altogether made dual-phase steels in high demand, especially in the automotive industry and gave great applicability in car safety parts [5]. Figure 1.2 presents usage

of dual-phase steels in a car body.

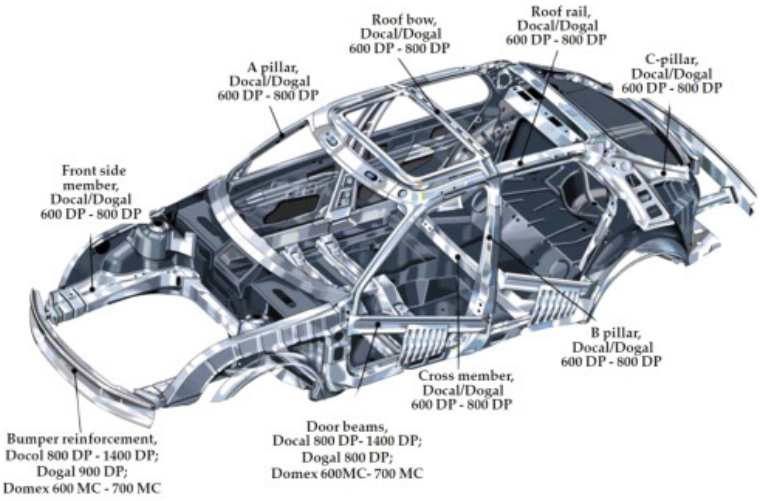

Figure 1.2: A car body showing different grades of DP steels in its main frame [1].

Commercial names such as DP600, DP750 etc. represent the grade and the number in the name shows the ultimate tensile strength of the material. The ultimate tensile strength of commercially available steels ranges from 450 to 1200 MPa [1]. Comparison of dual-phase steels with other available high strength (HS) low alloy steels is shown in Figure 1.3

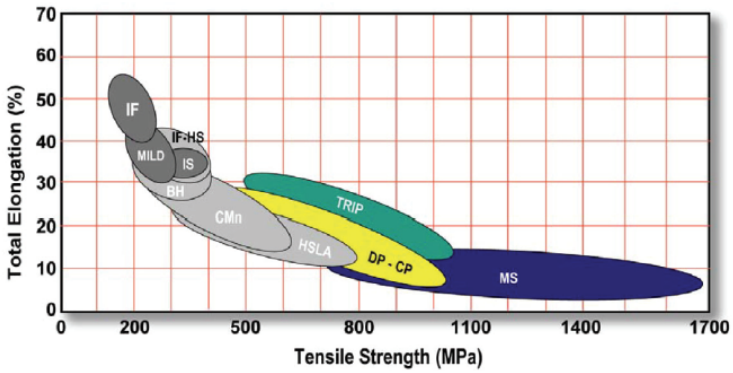

Figure 1.3: Low strength steels are in dark grey, traditional HS steels are in grey, remaining colors are for advanced HS steels [5].

Dual-phase steels have a greater strain hardening rate, which is a distinctive property when compared with other low alloy steels. Dual-phase steels strengthen and reach higher stress values during plastic deformation as an outcome of the strain hardening process. The strain hardening behaviour of any metallic material can be identified by

experiments and described by appropriate empirical or phenomenological relations. For steels, various mathematical descriptions exist in the literature (see e.g. [6], [7], [8], [9]). Due to the microstructural complexity of DP steels the overall constitutive response can not be captured by such classical hardening laws. Considering the fact that the mechanical response of each phase is different, each constituent phase must be investigated separately. As an example, the electron backscatter diffraction (EBSD) images of two different dual-phase steels are presented in Figure 1.4, where the dark areas indicate martensitic phase.

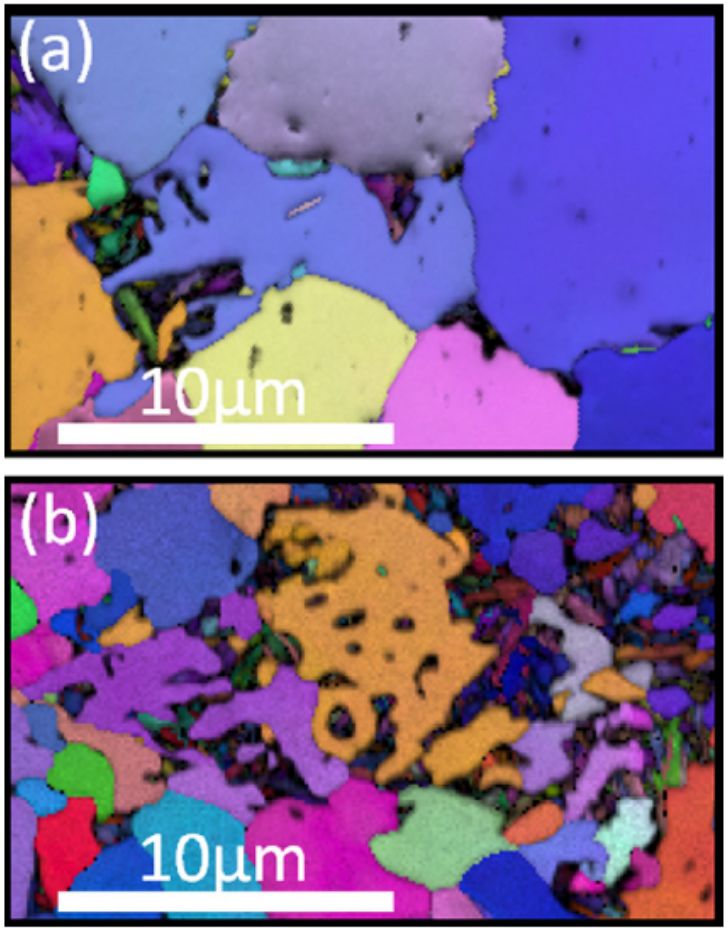

Figure 1.4: EBSD maps of DP600 (a) and DP800 (b) steels [10].

Getting accurate predictions of the mechanical response of a dual-phase steel is only possible when the features of both are considered separately. The characteristics of individual phases are influenced by traits such as phases' carbon content, volume fraction, grain size and morphology, which conjointly affect the dual-phase steel's

overall response [11], [12]. Due to plastic incompatibility between ductile and brittle phases, damage accumulations and stress localizations exist at the microstructural level, especially between the grains of different phases. Although dual-phase steels are very advantageous, these microstructural flaws can cause catastrophic failure of the bulk material [1]. Therefore, it is vital to gain an in-depth knowledge of the micromechanics of the plastic deformation. Therefore micromechanical modelling of dual-phase steels is crucial to understand and capture the bulk constitutive response. In this context crystal plasticity finite element method is an ideal candidate to simulate the behavior at mesoscale. Various studies exist in the literature which study these materials through crystal plasticity using representative volume elements (RVEs) and experimental observations (see e.g. [13], [14]). Although, in general, modelling and discussions have been held under uniaxial loading conditions, the effect of stress triaxiality has not been discussed before.

In this regard, the purpose of this thesis is to study of the micromechanics of plastic deformation in dual phase steels through RVEs, using crystal plasticity and J2 plasticity approaches under different triaxiality values. In order to realize this, four different representative volume elements are generated with different martensite volume fractions to be deformed under axial tensile loading conditions. The effect of microstructural properties on overall plastic behaviour and localization at grain scale is discussed at different triaxiality values. The effect of boundary conditions on the plastic behaviour of RVEs is discussed for both phenomenological and micromechanical plasticity models. The similarities and the differences between modelling approaches are investigated under the effect of stress triaxiality and the results are discussed with respect to the ones in the existing literature.

The thesis is organizes as follows. First in Chapter 2, the micromechanical aspects of plastic deformation in dual phase steels is summarized together with modelling approaches used in the literature and the current study. Then in Chapter 3, the micromechanical model is presented with loading and boundary conditions. The homogenization of the RVE response is also discussed in detail. In Chapter 4, the numerical results are presented and discussed. Lastly, in Chapter 5, the concluding remarks are given and an outlook is presented for future studies.

CHAPTER 2

MICROSTRUCTURAL ASPECTS AND CONSTITUTIVE MODELLING OF PLASTIC DEFORMATION IN DP STEELS

2.1 Strength and ductility of dual-phase steels

In this section the microstructural aspects of plastic deformation in dual phase steel is addressed shortly. The most influential issues are the martensite volume fraction, martensite carbon content, the ferrite grain size and the morphology of the martensite phase.

Conducting experimental tests is a simple yet effective way to investigate the strength and the ductility of a variety of materials. Data such as strain hardening, yield strength, ultimate tensile strength, fracture strength and strain are commonly collected and these are sufficient to get an overview of the material. It is also common to perform experiments, such as uniaxial tension, on dual phase steels to obtain the main characteristics.

During uniaxial tension experiments of DP steels both phases start to deform elastically. Then the ductile phase, ferrite, starts to yield first since its yield strength is lower than the brittle martensite phase. While deformation spreads through the ferritic matrix, martensite keeps deforming elastically until its yield point. Above this yield point martensite islands also start to yield. The brittleness and the strength of dual-phase steel depend on the brittleness and strength of its martensitic phase. Since the yield and ultimate stress values between ferrite and martensite is highly unlike, an inter-granular plastic instability occurs [15]. Due to this plastic instability, localizations occur at the interphase where martensite and ferrite meets [16]. This local accumulation plays an important role in dual-phase steels hardening behaviour. The

overall mechanical response, especially strength and ductility of a dual-phase steel is highly influenced by its martensite volume fraction, martensite carbon content, ferrite grain size and martensite morphology [2]. Following sections will present an overview of fundamental microstructural features which have substantial effects on the overall behaviour.

2.1.1 Effect of martensite volume fraction

First, the effect of the martensite volume fraction on the global material response will be discussed. Martensitic phase can be imagined as fibres reinforced in a matrix and is the backbone of the material. Volume fraction of martensite has been studied extensively and found that it influences the strength and ductility of the dual-phase steels primarily [17], [18], [19]. It is stated that martensite volume fraction has a linear relationship with the yield and tensile strength, which can be due to rule of mixture (see e.g. [4], [20]). Strength increases with increasing martensite volume fraction but V_m has a larger contribution on the ultimate tensile strength than the yield strength (see e.g [20]), except when the martensite carbon content is low [4]. Figure 2.1 presents martensite volume percent as a function of yield and ultimate tensile strength and shows that martensite volume fraction has a smaller effect on the yield strength when compared to ultimate tensile strength. Martensite volume fraction shows approximately a linear relationship with the tensile strength.

As for materials ductility, increased martensite volume percent provides undesirable results. Overall strength of the material increases at higher martensite percentages, however this is always disadvantageous for materials ductility. According to experiments conducted by Ahmad et al., increasing volume fraction increases ultimate tensile strength while elongation of steel decreases drastically [17]. Findings of aforementioned research is presented in Figure 2.2.

2.1.2 Effect of martensite carbon content

The martensite carbon content is another important aspect that affects the overall behaviour. The strength of martensite is directly linked to its individual carbon content.

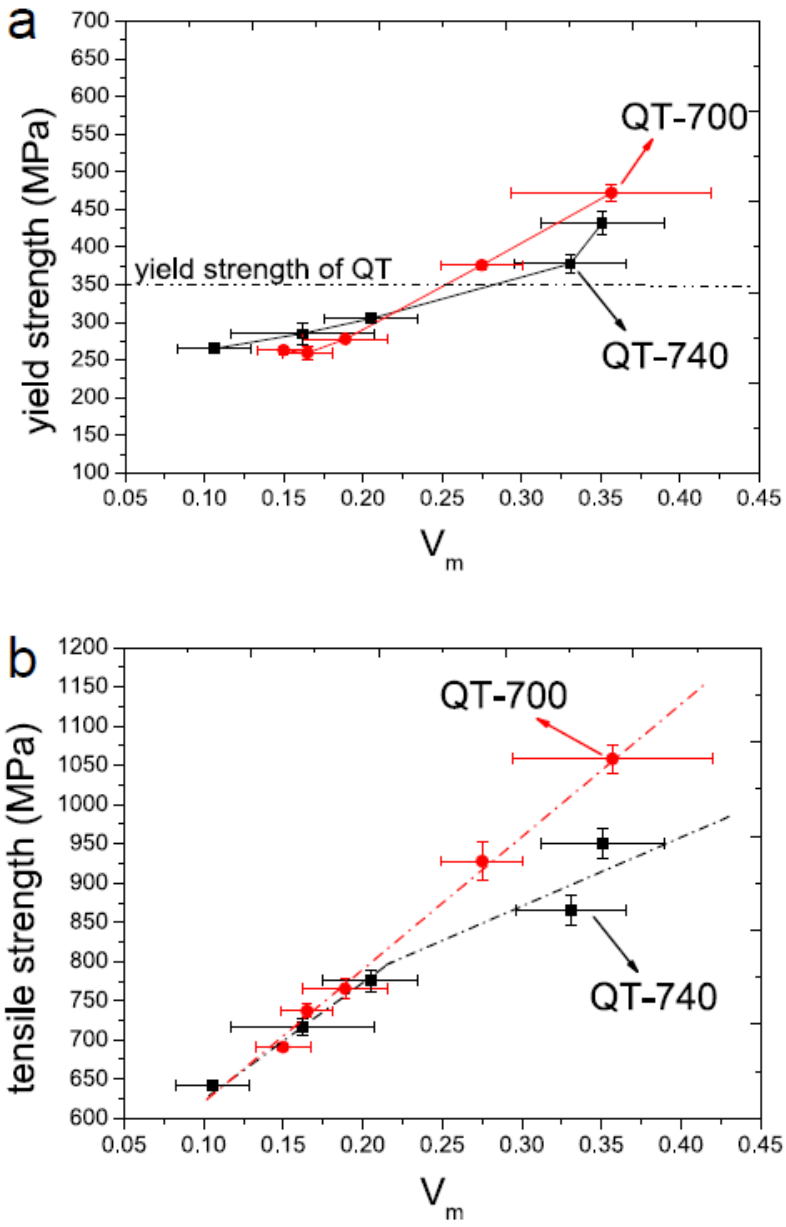

Figure 2.1: Yield (a) and tensile (b) strengths of DP grades QT-700 and QT-740 as a function of martensite volume fraction [18].

An increase in the carbon content results in an increase in the steel's strength and hardening rate (see e.g. [19], [21], [22]).

The highest carbon content means the strongest martensite but with compromised ductility based on experiments of Ramos et al. [20]. It is observed that increased carbon content is unfavourable for materials elongation since martensite with higher

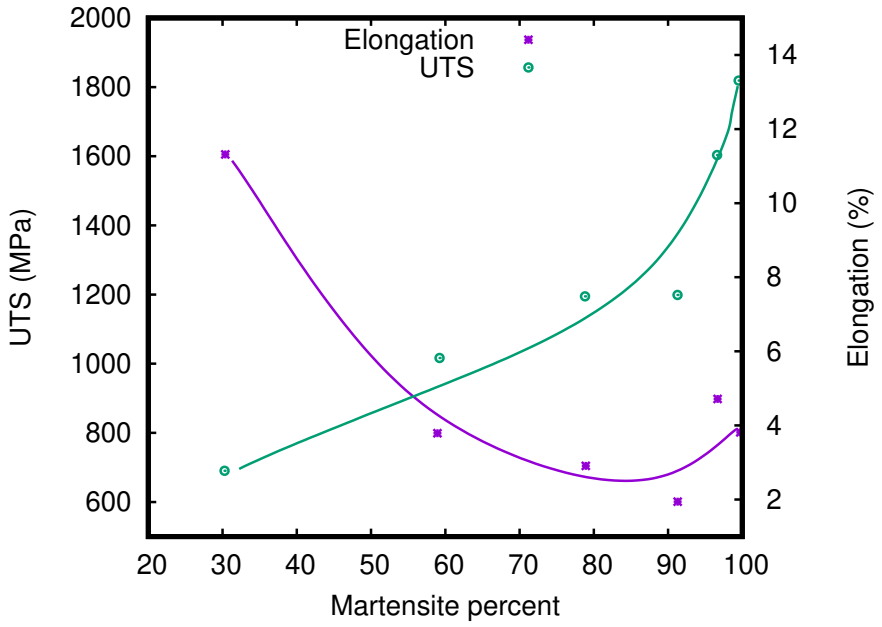

Figure 2.2: Effect of martensite volume fraction as a function of UTS and elongation [17].

carbon content shows brittle characteristic. Figure 2.3 shows the relation between ductility and martensite carbon content. It is presented the ductility and the carbon content show an opposite tendency. Brittleness of martensite can be downgraded at some level by decreasing its carbon content, therefore early deformation in martensite can only be prevented by decreasing its strength.

2.1.3 Effect of ferrite grain size

In comparison to martensite, ferrite phase contains lower percentages of carbon. Hence, the carbon content has an unnoticeable effect on ferrite's flow behaviour. Ferrite's grain size is the major microstructural trait that affects its own plastic behaviour and therefore the strength and ductility of the DP steel as well [18].

As the ferrite grain size decreases, the yield strength and the ultimate strength increases in accordance with the classical Hall–Petch relation [22], [23]. The influence of the ferrite grain size on the yield strength of the DP steel is observed to be stronger than its effect on the ultimate tensile strength (see e.g. [24]). Based on the research

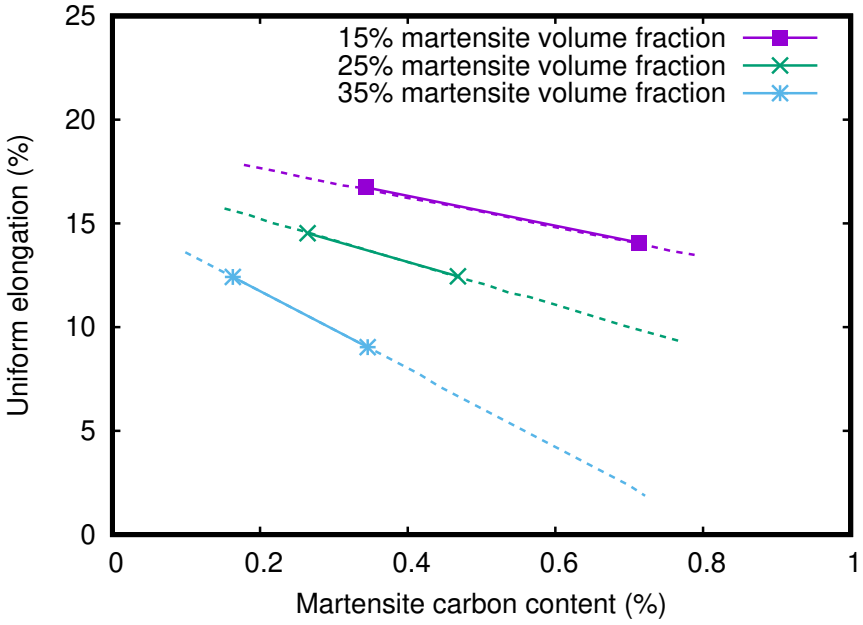

Figure 2.3: Experimental findings of different steels elongation and martensite carbon content [20].

of Jiang et al., decreasing grain size increases the flow stress and raises the strain hardening at low strains the effect is limited at high strain values [25]. Figure 2.4 shows the relation between the grain size and the tensile stress through experiments conducted on DP steels having a constant martensite volume fraction around 25%.

The grain size effect of the martensite phase is not investigated here, as it does not have a strong influence on martensite's flow behaviour, which is affected primarily by its carbon content [26]. Therefore, there is no formulation relating the martensite flow behaviour to its grain size in the literature.

2.1.4 Effect of martensite morphology

The effect of the martensite morphology on dual-phase steel's strength and ductility is the last microstructural aspect considered here. The morphology (the shape and the distribution) of martensite phase has considerable effect on the strength and the ductility of dual-phase steels due its contributions in microstructural traits such as grain size and connectivity [27]. The effect itself is controversial and requires in

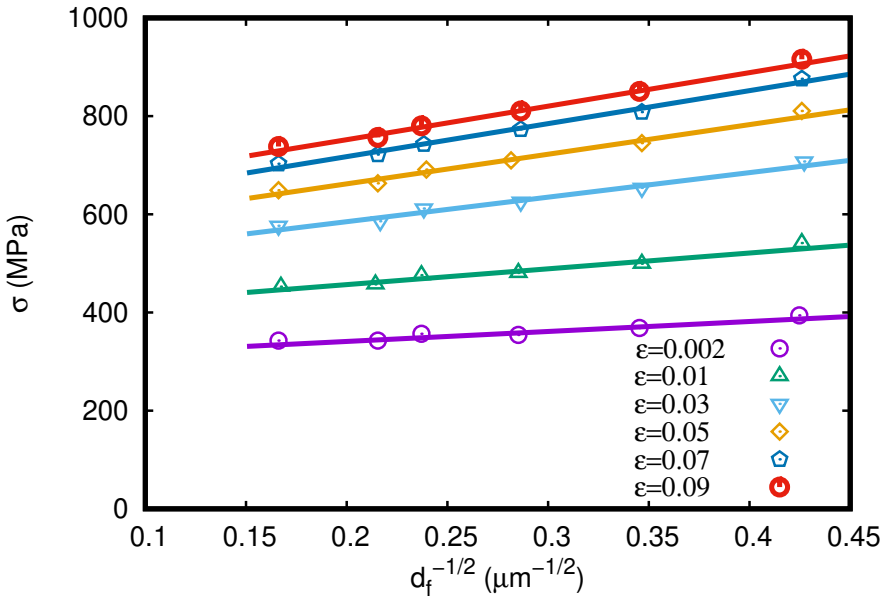

Figure 2.4: Tensile stress as a function of inverse square root of ferrite grain size at different chosen strain values [25].

depth microstructural studies. In the production process martensite grains can have an elongated or equiaxed structure. Figure 2.5 shows common, elongated and equiaxed martensite phases, which are indicated with whiter areas.

Mazinani and Poole claimed that the martensite morphology is not related to the overall steel strength but is related to the ductility [4]. Same study stated that in low carbon DP steels martensite goes under a considerable amount of plastic deformation so it is possible to increase the martensite's individual strength by decreasing martensite connectivity, which is achieved by preferring the equiaxed morphology rather than elongated one [4]. Bag et al. found that equiaxed structures tend to distribute strain more homogeneously, therefore steels with equiaxed martensite have superior uniform elongation [11]. Sarwar and Priestner stated that ductility is highest when martensite islands are elongated and finely dispersed when compared to equiaxed martensite islands [28]. The relation between the morphology and the overall strength is not completely clear. It is claimed that equiaxed martensite particles limit the plastic flow in ferrite phase which causes strain hardening and increase in the yield and the ultimate tensile strength [19]. Figure 2.6 presents the stress-strain response of a

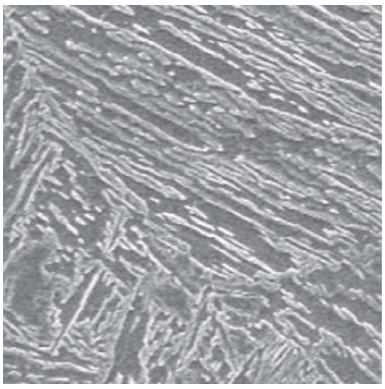

(a) Long elongated martensite

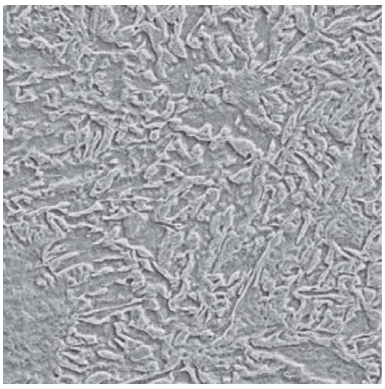

(b) Short elongated martensite

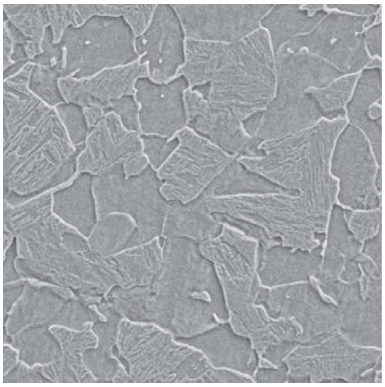

(c) Equiaxed martensite

Figure 2.5: SEM micrographs that belong to dual-phase steels with different martensite morphologies [19].

DP steel (with 60% martensite volume fraction and 0.15wt% carbon content) up to onset of necking. It is seen that the equiaxed morphology presents highest strength with lowest elongation while long banded morphology shows vice versa. In the meanwhile some other studies claim that long elongated martensite morphology provides higher strength (see e.g. [28]). Therefore the effect of morphology on strength is arguable and requires further micromechanical analysis.

2.2 Constitutive modelling of dual-phase steels

After shortly discussing the interesting microstructure of the DP steels, an overview on the constitutive modelling of these materials is presented in the following.

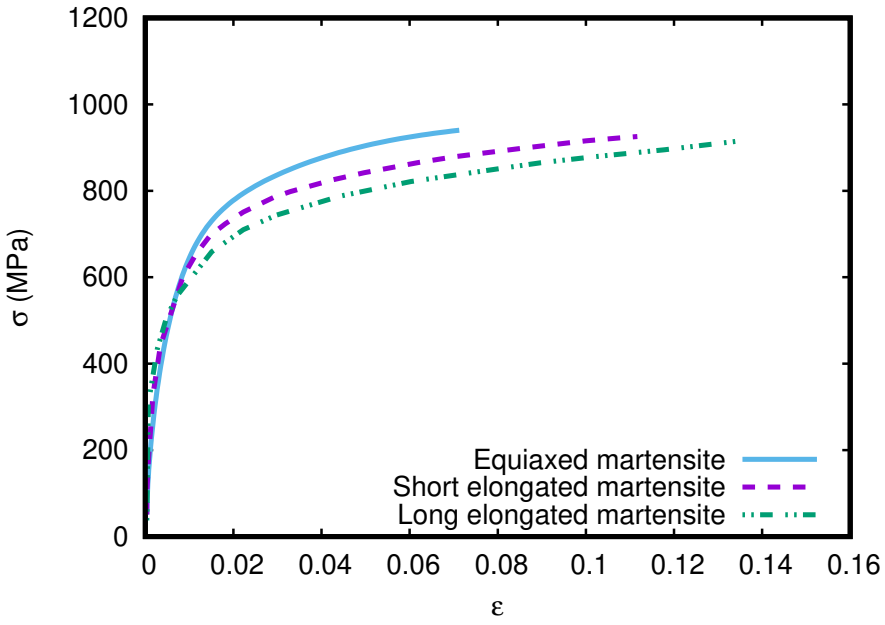

Figure 2.6: Experimental tensile curves of DP steels with different morphologies [19].

Obtaining an accurate stress-strain response for each phase is the key for modelling the overall behavior of DP steels. In order to do that one can conduct experiments such as micro pillar compression [3], in situ neuron [13], high energy X-ray diffraction [15] and nanoindentation [29] for determining the constitutive behaviour and microstructural characteristics of the phases. The collected data then could be used to develop constitutive models which would represent the the mechanical response of individual phases in a dual-phase steel [10], [18], [30]. While some would choose to come up with classical phenomenological relations for hardening (see e.g. [31]), the others try to relate the phenomena to the physics of the plasticity at grain scale (e.g. through dislocation densities) (see e.g. [32]). However, in both cases a flow curve is obtained which would eventually be used as hardening data for phenomenological plasticity modelling (e.g. J2 plasticity). The other option is to use a physics based approach such as crystal plasticity in order to bridge the micro plasticity to macro behaviour (see e.g. [16]). In this case the plastic slip values are summed up on each slip systems to obtain the plastic strain, which would be then used to get the local stress response. The model would be anisotropic as the amount of slip would differ from grain to grain due to their own individual orientations. In this section an overview of these modelling approaches will be summarized. Both the flow curve and crystal

plasticity modelling techniques will be employed throughout the thesis.

2.2.1 Phenomenological flow curve

Phenomenological equations representing the flow behaviour of the dual phase steels are the most common way to simulate the plastic behaviour of both phases. The parameters of these models are identified through a comparison with the uniaxial tensile test data. Unfortunately the parameter set identified for a certain grade of steel would not work for the other types with different microstructures. Therefore one has to be careful when using these models and their parameters.

Hill'48 and J2 plasticity frameworks are the most common ones that has been used in the literature to model the DP steels. Certain flow rules are incorporated specific to the material. Anisotropic plasticity models that use Hill'48 yield surface focus more on the sheet metal forming and forming limit diagrams (see e.g. [33]). The following represents the yield function and the equivalent stress description of the Hill model,

$$f(\sigma, \varepsilon_P) = \sigma_{Hill} - s = 0 \tag{2.1}$$

$$\sigma_{Hill} = \sqrt{F(\sigma_y - \sigma_z)^2 + G(\sigma_z - \sigma_x)^2 + H(\sigma_x - \sigma_y)^2 + 2L\tau_{yz}^2 + 2M\tau_{zx}^2 + 2N\tau_{xy}^2}. \tag{2.2}$$

σ_{Hill} is Hill'48 equivalent stress, ε_P is equivalent plastic strain, σ is Cauchy stress tensor, s is the deformation resistance related to hardening law. Constants F to N are anisotropy parameters which can be found from associated flow rule. The flow rule associated to Hill'48 yield criterion is

$$d\varepsilon_{\mathbf{P}} = d\varepsilon_P \frac{\partial f}{\partial \sigma} \tag{2.3}$$

where, $\varepsilon_{\mathbf{P}}$ represents the plastic strain tensor. Different hardening or flow relations can be used to present the strain hardening behaviour. In the above mentioned refer-

ence [33], Swift hardening law is used,

$$s = A(\varepsilon_0 + \varepsilon_P)^n. \tag{2.4}$$

Swift law gives a good fit during uniform elongation, however, it should modified for higher strain levels.

The classical J2 elastoplasticity framework with isotropic hardening is actually the most commonly used tool to predict plastic behaviour of DP steels. Likewise, Swift law is used frequently with J2 as well see (e.g. [34]). The other flow rules are also employed through a parameter identification procedure with respect to experimental data, e.g. Ludwik strain hardening law [15]. Hardening behaviour of ferrite and martensite is fitted to Ludwik equation which has a general form of $\sigma = \sigma_y + K\varepsilon_P^n$. The flow relations of ferrite and martensite are

$$\sigma_0 = \sigma_{y,f} + K_f \varepsilon_P^{n_f} \tag{2.5}$$

$$\sigma_0 = \sigma_{y,m} + K_m \varepsilon_P \tag{2.6}$$

respectively. $\sigma_{y,f}$ and $\sigma_{y,m}$ are the initial yield strengths, K_f and K_m are the hardening coefficients, n_f is the hardening exponent for ferrite phase. Martensite hardening behaviour is assumed to be linear therefore the corresponding flow equation does not include an exponent [7].

Another study proposes an exponential law to fit flow behaviour of martensite according to experimental flow curves of 100% martensite specimens [19]. The relation is as follows,

$$\sigma_{y,m} = \sigma_{y0,m} + k_m(1 - exp(-\varepsilon_P n_m)) \tag{2.7}$$

where $\sigma_{y,m}$ is current yield strength, ε_P is accumulated plastic strain and $\sigma_{y0,m}$, k_m, n_m are material parameters. The affect of carbon content on strain hardening is found

from following relation,

$$\sigma_{y0,m} = 300 + 1000 C_m^{1/3} \tag{2.8}$$

where $\sigma_{y0,m}$ is the current yield strength and C_m is the martensite carbon content in $wt\%$. The hardening modulus k_m is directly proportional with C_m

$$k_m = \frac{1}{n_m}\left[a + \frac{bC_m}{1 + \left(\frac{C_m}{C_0}\right)^q}\right]. \tag{2.9}$$

Strain hardening formulation for ferrite phase obeys to a modified Swift hardening law,

$$\sigma_{y,f} = \sigma_{y0,f} + (1 + H_f \varepsilon_P)^{n_f} \tag{2.10}$$

where $\sigma_{y0,f}$, H_f and n_f are material parameters and depend on the production process. Parameters are fitted according to experimental findings and kept the same throughout aforementioned research.

Studies of Lai et al follow the same approach presented in Eqs. (2.7)-(2.9) for martensite, while work hardening relation for ferrite is fitted to a modified version of Voce strain hardening law [18], [26]. Proposed law for ferrite is based on its dominant microstructural traits. Ferrite has low carbon content because of its nature, therefore carbon content in ferrite does not contribute to its hardening process. Accumulated dislocations along ferrite grain boundary is the main mechanism that hardens ductile ferritic phase. It is revealed that regardless of the value of dynamic recovery coefficient, dislocations accumulate at large strains and cause stage-IV strain hardening. Therefore a modified expression for ferrite is described by a Voce law for stage-III and a stage-IV with constant hardening,

$$\sigma_{y,f} = \sigma_{y0,f} + \frac{\theta_f}{\beta}(1 - exp(-\beta \varepsilon_P)) \quad \text{for} \quad \sigma_{y,f} < \sigma_y^{tr} \tag{2.11}$$

$$\sigma_{y,f} = \sigma_y^{tr} + \theta_{IV}(\varepsilon_P - \varepsilon_P^{tr}) \quad \text{for} \quad \sigma_{y,f} > \sigma_y^{tr} \tag{2.12}$$

where $\sigma_{y0,f}$ is the current ferrite yield strength, θ_f is initial work hardening rate and β is the dynamic recovery coefficient. σ_y^{tr} and ε_P^{tr} are values of flow stress and plastic strain at the point where transition from stage-III to stage-IV hardening takes place. Hardening rate θ_{IV} is a constant, altogether with σ_y^{tr} and ε_P^{tr} are expressed as

$$\sigma_y^{tr} = \sigma_{y0,f} + \frac{\theta_f - \theta_{IV}}{\beta} \tag{2.13}$$

and

$$\varepsilon_P^{tr} = \frac{1}{\beta} ln\Big(\frac{\theta_f}{\theta_{IV}}\Big). \tag{2.14}$$

Swift type law shows much higher work hardening rates at larger strains which overestimates the uniform elongation is ferrite. Swift type law defined in Eq. (2.10) is applicable up to moderate strain levels, after a threshold value, the macroscopic stress strain response of dual-phase steel is not captured correctly. Different stress strain responses simulated by Swift and Voce+stage-IV are presented in Figure 2.7. It is seen that resulting curves disagree due to selection of different strain hardening laws for ferrite, and Swift type law overestimates the overall stress response.

Various phenomenological models exist in the literature which have relatively lower computational cost and complexity compared with the micromechanical models such as crystal plasticity frameworks. Phenomenological laws include material properties that require calibration and will not be reliable in the absence of separate credible experimental data for each phase. If there are sufficient findings, phenomenological models will provide simplicity and reduction in computation time. Still for many cases the stress strain response of dual-phase steels cannot be adequately defined with a certain function. Considering the fact that dual-phase steels deform in multiple stages, choosing a law containing stepwise functions may give realistic results.

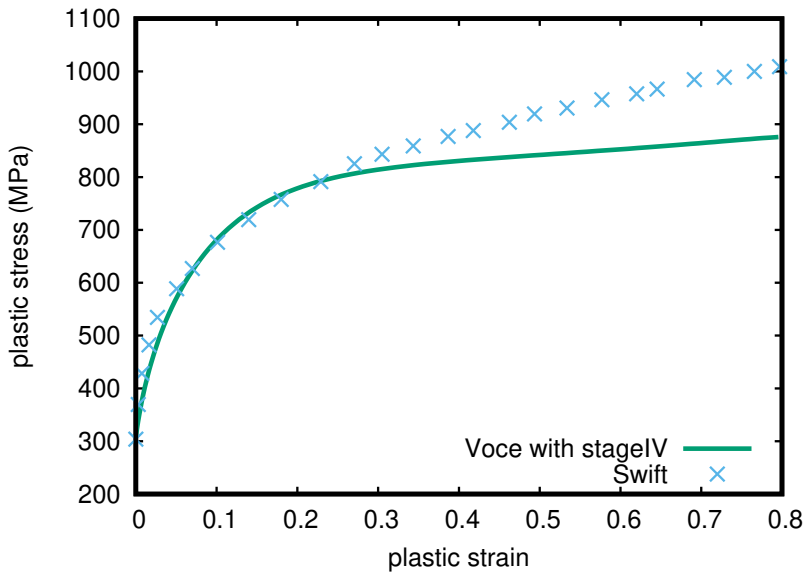

Figure 2.7: Comparison of simulated stress strain behaviours for the same DP [18].

2.2.2 Physics based phenomenological constitutive modelling

Another option for describing the flow behaviour of dual phase is to use physically based empirical formulations, which eventually enters plasticity models such as J2 and Hill. A striking example in this context is a model which describes the strain hardening behaviour of constituent phases as a function of dislocation storage and recovery [35]. The model approximates the flow resistance on a slip plane by taking slip properties, such as Burger's vector, line direction and dislocation densities into account. In the regarding work, the macroscopic stress σ and the plastic strain ε are linked to the critical resolved shear stress τ and the crystallographic slip γ with orientation factor M as follows,

$$\sigma = M\tau \quad \text{and} \quad M.d\varepsilon = d\gamma. \tag{2.15}$$

From Eq. (2.15) the microscopic work hardening rate of the crystalline, $\frac{d\tau}{d\gamma}$, can be related to the macroscopic work hardening rate as

$$\frac{d\sigma}{d\varepsilon} = M^2\frac{d\tau}{d\gamma} + \tau\frac{dM}{d\varepsilon}. \tag{2.16}$$

Second term of Eq. (2.16) stands for the effect of the strain on orientation variation.

The classical relationship between tensile stress and dislocation density is given by,

$$\sigma = \sigma_0 + \Delta\sigma + \Delta\sigma_\varepsilon = \sigma_0 + \Delta\sigma + \alpha M \mu b \sqrt{\rho}. \tag{2.17}$$

The first term σ_0 is the Peierl's stress which is identified as follows,

$$\begin{aligned} \sigma_0 = 77 + 750\%P + 60\%Si + 80\%Cu + 45\%Ni \\ +60\%Cr + 80\%Mn + 11\%Mo + 5000\%N_{ss} \end{aligned} \tag{2.18}$$

where unknowns above are alloys in the DP steel and N_{ss} is the nitrogen content in solid solution. The second term $\Delta\sigma$ stands for the additional strengthening due precipitations and carbon in the solution. For ferrite, $\Delta\sigma$ is

$$\Delta\sigma(MPa) = 5000 \times \%C_{ss}^{f} \tag{2.19}$$

and for martensite,

$$\Delta\sigma(MPa) = 3065 \times \%C_{ss}^{m} - 161 \tag{2.20}$$

where $\%C_{ss}^{f}$ and $\%C_{ss}^{m}$ are the carbon content in ferrite and martensite respectively.

Third term reflects the effect of the strengthening and the softening due to dislocations. It consists of a constant α, Taylor factor M, shear modulus μ, Burger's vector b and dislocation density ρ. During the deformation, the evolution of dislocation density is given as follows

$$\frac{d\rho}{d\gamma} = \left.\frac{d\rho}{d\gamma}\right|_{stored} - \left.\frac{d\rho}{d\gamma}\right|_{recovery}. \tag{2.21}$$

Substitution of $Md\varepsilon = d\gamma$ in Eq. (2.21) allows expressing the dislocation density change in terms of macroscopic equivalent strain. Different formulations exist for

each term. Generally, Eq. (2.21) becomes,

$$\frac{d\rho}{d\varepsilon} = M\Big(\frac{1}{bL} - k_r\rho\Big), \tag{2.22}$$

where k_r is recovery rate and L is dislocation mean free path which is a constant. Taking initial dislocation density as ρ_0 gives

$$\Delta\sigma_\varepsilon = \alpha M\mu\sqrt{b}\sqrt{\frac{k}{k_r}[1 - exp(-k_r M\varepsilon)] + \rho_0 exp(-k_r M\varepsilon)} \quad \text{with} \quad k = \frac{1}{bL} \tag{2.23}$$

Eq. (2.23) can be rearranged as

$$\Delta\sigma_\varepsilon = \alpha M\mu\sqrt{b}\sqrt{\frac{1 - exp(-Mk_r\varepsilon)}{k_r L}} \tag{2.24}$$

which can be applied to ferrite and martensite to predict their flow stresses. With the correct set of parameters, this approach is enough to predict flow curves with great accuracy.

Initial dislocation density is usually negligibly small, with some rearrangements the final relation can be expressed as follows

$$\sigma = \sigma_0 + \Delta\sigma + \alpha M\mu\sqrt{b}\sqrt{\frac{1 - exp(-M \cdot k_r\varepsilon^p)}{k_r L}} \tag{2.25}$$

In here, α and M terms have a strong influence on strain hardening characteristics. The studies conducted till now with different dual-phase steels adopt 0.3 and 3 respectively for these parameters, which comply well with the experimental flow curves. Therefore a data fit process is not needed. Dislocation density based flow curve modelling is quite common in the literature (see e.g. [21], [22], [30], [32], [36], [37], [38], [39], [40], [41]). Even though phenomenological and physics based flow curves incorporated in to classical macroscopic plasticity frameworks give satisfactory results, they do not take into account many of the microstructural aspects of the dual phase steels. Therefore for a more physical simulation with a better representation of the

microstructure, the crystal plasticity modelling offers better solutions, which will be described shortly in the upcoming subsection.

2.2.3 Physics based micromechanical models

Crystal plasticity based finite element (CPFEM) method has gained popularity to study anisotropic deformation mechanisms in polycrystalline materials. Although isotropic hardening theory is able to capture the overall stress-strain behaviour of the material, it cannot thoroughly give information about local deformations and relation between stress and microstructural attributes. Thus, in order to remedy this downside of the plasticity modelling, Crystal Plasticity Finite Element Method (CPFEM) has been used in polycrystalline aggragates, which captures the localization together with the influence of microstructural characteristics on the overall strength of dual-phase steels (see e.g. [10], [42], [43], [44], [45], [46]). Asaro's single crystal plasticity theory states that the total plastic deformation is the cumulative of crystal slip on all activated slip systems [47]. Formulation of this theory is developed by Hill and Rice [48]. Plastic deformation of a metallic material results from shearing on crystallographic slip systems and lattice stretching and rotation. Local plastic deformation due to shearing gives the plastic $\mathbf{F^P}$, elastic stretching and lattice rotation gives the elastic deformation gradient $\mathbf{F}^*$. Total deformation gradient tensor $\mathbf{F}$ is an decomposed as

$$\mathbf{F} = \mathbf{F}^*\mathbf{F^P}. \tag{2.26}$$

Elastic stress strain relation below links $\mathbf{F}^*$ to stress

$$\mathbf{T}^* = \mathcal{C}[\mathbf{E}^*] \quad and \quad \mathbf{E}^* = \frac{1}{2}\mathbf{F}^{*\mathbf{T}}\mathbf{F}^* - \mathbf{1}. \tag{2.27}$$

$\mathbf{T}^*$ is called the second Piola-Kirchoff stress and it is the elastic conjugate stress to the elastic strain tensor $\mathbf{E}^*$. $\mathbf{E}^*$ is also named the Lagrangian strain. $\mathcal{C}$ is the cubic symmetric fourth order elasticity tensor. For cubic crystals $\mathcal{C}$ has three independent

constants C_{11}, C_{22} and C_{44}. $\mathbf{T}^*$ is linked to symmetric Cauchy stress tensor $\mathbf{T}$ as,

$$\mathbf{T}^* = \mathbf{F}^{*-1}(\mathbf{det}(\mathbf{F}^*)\mathbf{T})\mathbf{F}^{*-\mathbf{T}}. \tag{2.28}$$

Rearranging formulation above following is obtained

$$\mathbf{T} = (\mathbf{det}(\mathbf{F}))^{-1}\mathbf{F}^*\mathbf{T}^*\mathbf{F}^{*\mathbf{T}}. \tag{2.29}$$

In current configuration, local plastic deformation gradient is linked to the velocity gradient as follows

$$\mathbf{L} = \dot{\mathbf{F}}\mathbf{F}^{-1} = \dot{\mathbf{F}}^*\mathbf{F}^{*-1} + \mathbf{F}^*\dot{\mathbf{F}}^{\mathbf{P}}\mathbf{F}^{*\mathbf{P}}\mathbf{F}^{*-1}. \tag{2.30}$$

First part of Eq. (2.30) is the elastic part of the velocity gradient. The second part is the plastic part of the velocity gradient, which can be written as,

$$\mathbf{L}^{\mathbf{P}} = \dot{\mathbf{F}}\mathbf{F}^{-1} - \dot{\mathbf{F}}^*\mathbf{F}^{*-1} = \mathbf{F}^*\dot{\mathbf{F}}^{\mathbf{P}}\mathbf{F}^{*\mathbf{P}}\mathbf{F}^{*-1}. \tag{2.31}$$

In case of crystals the plastic part of the velocity gradient of current state is a function of the plastic slip rate on each slip system, which is expressed as [49],

$$\mathbf{L}^{\mathbf{P}} = \sum_{\alpha=\mathbf{1}}^{\mathbf{n}} \dot{\gamma}^{(\mathbf{a})}\mathbf{n}^{*(\mathbf{a})} \otimes \mathbf{m}^{*(\mathbf{a})} \tag{2.32}$$

where $\mathbf{n}^{*(\alpha)}$ defines slip direction, $\mathbf{m}^{*(\alpha)}$ defines slip plane normal. $\mathbf{n}^{*(\alpha)}$ and $\mathbf{m}^{*(\alpha)}$ are time independent orthogonal vectors. $\dot{\gamma}^{(\alpha)}$ stands for rate of plastic shear on slip system α. During slip, slip plane vectors deform by the application of $\mathbf{F}^*$ [47]. So in a fixed reference frame, $\mathbf{n}^{*(\alpha)}$ can be written in terms of the slip direction in the current frame,

$$\mathbf{n}^{(\alpha)} = \mathbf{F}^{*-1}\mathbf{n}^{*(\alpha)}. \tag{2.33}$$

Normal to the slip plane and slip direction are mutually orthogonal, following can be written,

$$\mathbf{n}^{(\alpha)} \cdot \mathbf{m}^{(\alpha)} = \mathbf{m}^{(\alpha)} \cdot \mathbf{n}^{(\alpha)} = 0. \tag{2.34}$$

By the use of mutual orthogonality, slip plane normal can be obtained in terms of its equivalent in current configuration,

$$\mathbf{m}^{(\alpha)} \cdot (\mathbf{F}^{*-\mathbf{1}} \cdot \mathbf{n}^{*(\alpha)}) = 0. \tag{2.35}$$

Like slip direction, slip plane normal deforms through the same deformation gradient. To satisfy Eq. (2.35), the material description of slip plane normal must be

$$\mathbf{m}^{(\alpha)} = \mathbf{m}^{*(\alpha)} \cdot \mathbf{F}^{*}. \tag{2.36}$$

Amount of the slip on each slip system is found through plastic shearing strain rate $\dot{\gamma}^{(\alpha)}$.$\dot{\gamma}^{(\alpha)}$ is a function of resolved shear stress $\tau^{(\alpha)}$ and slip system deformation resistance $s^{(\alpha)}$, critical resolved shear stress. The dependence of $\dot{\gamma}^{(\alpha)}$ to the current resolved shear stress $\tau^{(\alpha)}$ differentiates rate dependent and rate independent plasticity models. The formulation used for $\dot{\gamma}^{(\alpha)}$ is in the form of power law and expressed as (see e.g. [50])

$$\dot{\gamma}^{(\alpha)} = \dot{\gamma}_0 \left| \frac{\tau^{(\alpha)}}{s^{(\alpha)}} \right|^{1/m} sign(\tau^{(\alpha)}) \tag{2.37}$$

where $\dot{\gamma}_0$ is the reference slip rate and it must obey $\dot{\gamma}^{\alpha} = \dot{\gamma}_0$ when $\tau^{(\alpha)} = s^{(\alpha)}$. Strain rate sensitivity m presented in Eq. (2.37) is found through [47]

$$m = \frac{\partial(ln\dot{\gamma})}{\partial(ln\tau)}. \tag{2.38}$$

Equations below give an explanation to resolved shear stress $\tau^{(\alpha)}$ [49]. In any current

configuration plastic stress power per unit volume is

$$\dot{\omega}^P = (\mathbf{C}^*\mathbf{T}^*) \cdot \mathbf{L}^{\mathbf{P}} \tag{2.39}$$

where $\mathbf{C}^*$ is the right Caughy-Green deformation tensor, which is the decomposition of deformation gradient as

$$\mathbf{C}^* = \mathbf{F}^{*\mathbf{T}}\mathbf{F}^*. \tag{2.40}$$

For crystallographic systems plastic stress power can also be defined as

$$\dot{\omega}^P = \sum_{\alpha}^{n} \tau^{(\alpha)}\dot{\gamma}^{(\alpha)}. \tag{2.41}$$

Eqs. (2.32), (2.39) and (2.41) lead to

$$\tau^{(\alpha)} = (\mathbf{C}^*\mathbf{T}^*) \cdot \mathbf{S}^{(\alpha)} \quad \text{and} \quad \mathbf{S}^{(\alpha)} = \mathbf{n}^{(\alpha)} \otimes \mathbf{m}^{(\alpha)}. \tag{2.42}$$

The current slip resistance or yield stress $s^{(\alpha)}$ evolves according to

$$\dot{s}^{(\alpha)} = \sum_{\beta=1}^{n} h^{\alpha\beta} \left|\dot{\gamma}^{\beta}\right| \tag{2.43}$$

where $h^{\alpha\beta}$ is the latent hardening matrix [49]. This matrix measures the strain hardening due to shearing of slip system β on slip system α. $h^{\alpha\beta}$ is proposed to have the form

$$h^{\alpha\beta} = q^{\alpha\beta}h^{(\beta)} \tag{2.44}$$

where $q^{\alpha\beta}$ indicates latent hardening behaviour and $h^{(\beta)}$ is the hardening rate for a

single slip

$$h^{(\beta)} = h_0 \left\{ 1 - \frac{s^{\beta}}{s_s} \right\}^{a} \tag{2.45}$$

where h_0, and s_s are hardening parameters. a exponent is a constant material parameter. Remaining are shear rate $\dot{\gamma}_0$, strain rate sensitivity m, initial slip resistance s_0 and latent hardening parameter q.

Please note that different formulations exist for evolution of slip resistance, given by Eq. (2.43), and evolution of hardening, given by Eqs. (2.44), (2.45). Therefore, these presented formulations are main equations for the calculation of plastic slip in each slip system in single crystal plasticity framework. After obtaining plastic slip of each slip system, the plastic strain, the elastic strain and the stress would be calculated. More detailed explanations could be found in the literature (see e.g. [51], [52]) on the strain decomposition and the incremental calculations of plastic strain.

CHAPTER 3

MICROMECHANICAL MODELLING OF DUAL-PHASE STEELS

In this chapter the micromechanical modelling framework of multiphase metallic materials is presnted in detail. The main purpose is to capture the plasticity behavior at both local (grain) and macroscopic scales. In order to achieve this, the material is represented by a representative volume element (RVE) which represents the behavior of a material point including the information of the microstruture as well. The selection of a realistic RVE and imposing proper boundary conditions provide the basis of reflecting large or infinitely large systems from micro level volumetric elements. Afterwards, the homogenization procedure is applied to transfer the microscopic mechanical behaviour to mesoscale (see e.g. [19], [38]). Figure 3.1 shows a RVE at microscale (right) and a periodic large system at mesoscale (left) which is composed of periodically stacked representative volume elements.

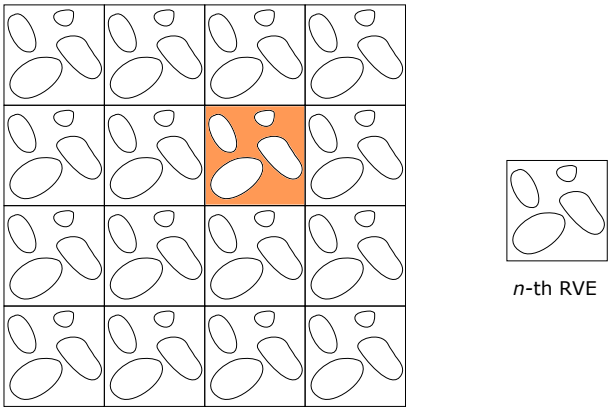

Figure 3.1: A 2D periodic large system and the n-th RVE.

The details of the micromechanical modelling of the material behaviour are explained in the following subsections. Initially, the construction of the RVE and the selection of constitutive models are addressed which is followed by the detailed description of

the boundary conditions. Finally the homogenization scheme is studied in detail.

3.1 Representative volume elements

Materials at mesoscale can be considered as duplicates of periodically repeating volumes which are representations of local microstructures. Arrays of duplicated local microstructures are tightly stacked so that they cannot overlap or have gaps in between. These local microstructures are called representative volume elements and they provide an accepted approach to study multi phase materials, since they are able to give good descriptions of stress and strain partitioning in phases. A good representative volume element should be large enough to reflect the physical attributes of the local microstructure, such that it should realistically mirror the shape and morphology of the bulk material . Aside from being large enough to agree with physical characteristics, it should also be properly small to give reasonable computation time (see e.g. [38] for RVE modelling of DP steels).

Different approaches exist to generate the required RVE. In addition to simple cell models such as stacked hexagonal arrays (see e.g. [38]), artificial or realistic cubic cell models (see e.g. [41], [53]), could be used as well. Moreover, real dual-phase microstructures can be detected by light optical microscopy (LOM) images or scanning electron microscopy (SEM) graphs (see e.g. [3], [54]), which could then be processed to construct RVEs based on real microstructures.

This study includes only artificial microstructures generated by Neper software which is used for polycrystal generation and meshing [55]. Neper generates microstructures by creating Voronoi tessellations in the space domain. Tessellations can be generated according to various morphological cell property data such as grain size, sphericity and volume fractions. Figure 3.2 shows Neper generated sample microstructure with 200 grains used for parameter fitting studies which will be explained in upcoming sections.

Throughout the thesis four different DP steel microstructures having around 400 grains are generated according to their microstructural properties. In this context, the ferrite grain sizes are picked as 6.5μm, 5.9 μm, 5.5μm and 4.2μm, while marten-

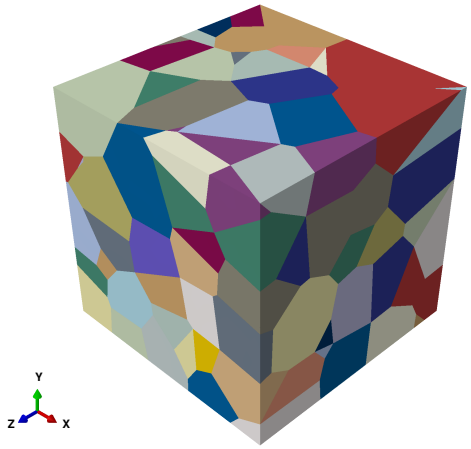

Figure 3.2: Artificial 200 grained microstructure generated with Neper.

site grain sizes are 1.2 μm, 1.5 μm, 2.1μm and 2.4μm respectively, as reported in [18]. All microstructures are meshed with ten-noded tetrahedral elements (C3D10 elements of ABAQUS finite element program [56]).

3.2 Constitutive behaviour of different phases

In the initial investigations, the J2 plasticity with isotropic hardening is employed for the modelling of both phases as presented in Section 2.2.1. Individual flow behaviour of martensitic phase is obtained from Eqs. (2.7)-(2.9), while the plasticity behaviour of ferritic phase follow Eqs. (2.11)-(2.14), as used in e.g. [18] and [26]. Flow curve of martensite depends on the carbon content while ferrite is influenced by the grain size. The results of the numerical analysis are presented in next chapter.

Next, for a more elaborate investigation, crystal plasticity finite element method is employed, based on the Huang's user material routine (see [51]), for the modelling of ferrite phase while the previous phenomenological plasticity framework still works for martensite phase (see e.g. [14], [16], [57], [58] for similar modelling approaches). The current approach takes into account the anisotropy due to different orientations at the grain scale which is expected to give more realistic and physical results on the microstructure evolution and localization. {1 1 2} slip family is used for the crystal plasticity modelling of ferrite phase which is considered to behave like other BCC

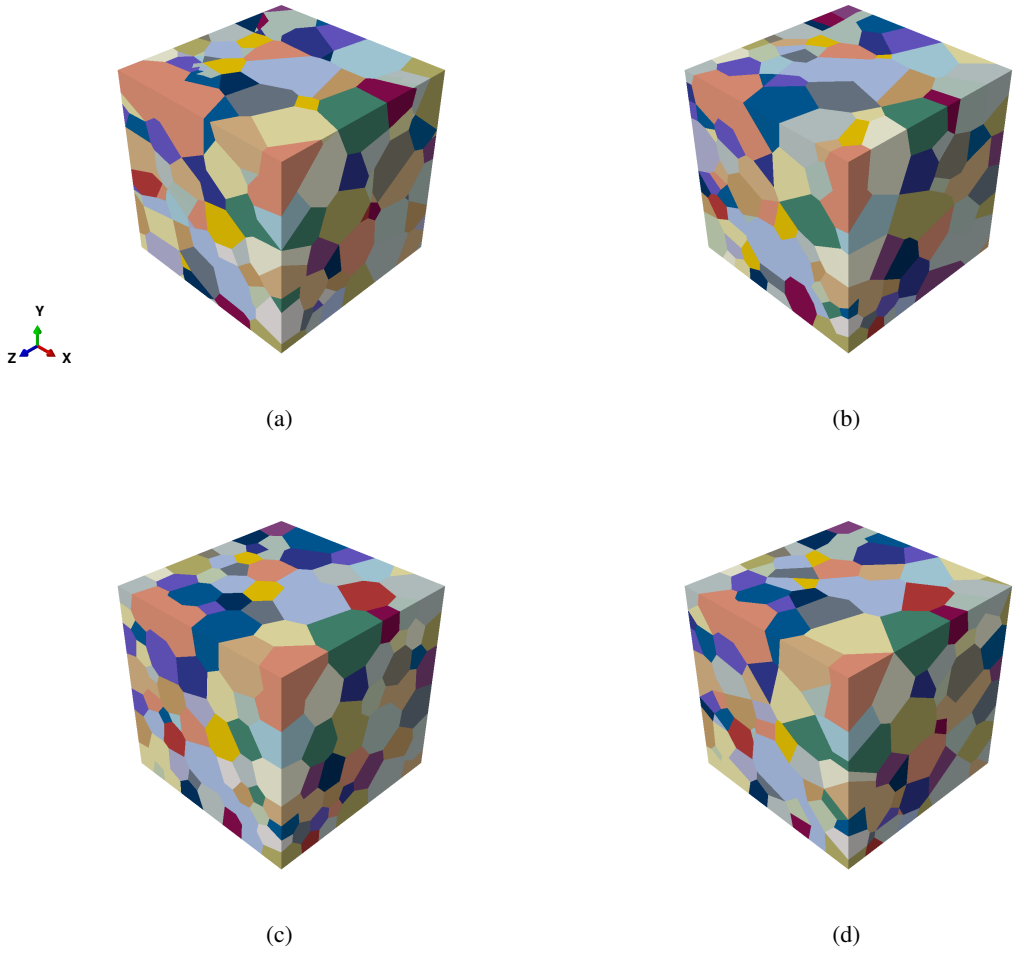

Figure 3.3: Artificial generated dual-phase steel microstructures with different ferrite and martensite average grain sizes.

crystals at room temperature (see e.g. [59] [52], [60]). For a more detailed analysis of slip activity of ferrite phase in DP steels please refer to [61]. The governing equations of crystal plasticity finite element method is presented in the previous chapter. The only difference here is the employed hardening relation. The self hardening moduli $h^{(\beta)}$ includes the effects of three stages of crystalline hardening and all shear strains, $\gamma^{(\alpha)}$, from all slip systems,

$$h^{(\beta)} = \left\{ (h_0 - h_s) sech^2 \left[\frac{(h_0 - h_s)\gamma^{(\alpha)}}{s^{(\alpha)} - \tau^{(\alpha)}} \right] + h_s \right\} G(\gamma^{(\beta)}; \beta \neq \alpha) \qquad (3.1)$$

where h_s is stage I hardening parameter and function G is expressed as

$$G(\gamma^{(\beta)}; \beta \neq \alpha) = 1 + \sum_{\beta \neq \alpha} f^{\alpha\beta} tanh(\gamma^{(\beta)}/\gamma_0) \tag{3.2}$$

where γ_0 is the slip amount at the strongest slip interaction and $f^{\alpha\beta}$'s are slip interaction strength magnitudes [51].

Parameters needed for ferrite's crystal plasticity flow behaviour are fitted to its rate independent von Mises elastoplastic finite element solution counterparts, which is previously gathered from Eqs. (2.11)-(2.14). The data fitting procedure is explained in detail in the upcoming chapter.

3.3 Implementation of boundary conditions and loads in ABAQUS

Void initiation, growth and coalescence have been the most crucial microstructure evolution phenomena leading to ductile damage initiation and fracture in metallic materials. The effect of such mechanisms have been studied experimentally and computationally in the literature (see e.g. [62], [63], [64], [65], [66], [67], [68]), especially after the pioneering work of Gurson who developed the most commonly used porous plasticity formulation for ductile damage evolution (see e.g. [69]). The deformation localization around the inhomogeneities results in the initiation of micro voids.These voids evolve and accumulate at certain regions by ongoing plastic deformation and finally lead to ductile damage [16]. Studies have emphasised that the rate of void growth, therefore the evolution of ductile damage, is strongly influenced by the ratio of hydrostatic stress to equivalent stress, namely the stress triaxiality [62], [70]. Therefore in order to analyse this effect in dual phase steels we focus our concentration on the triaxiality in the remaining of this thesis.

In order to handle the triaxiality state of the RVE properly the boundary conditions and loading should be defined carefully. In the following the materials stress state is

described by stress triaxiality, T, which is a non-dimensional parameter,

$$T = \frac{\Sigma_h}{\Sigma_{eq}} \tag{3.3}$$

$$\Sigma_h = \frac{\Sigma_{11} + \Sigma_{22} + \Sigma_{33}}{3} \tag{3.4}$$

$$\Sigma_{eq} = \frac{1}{\sqrt{2}} \sqrt{\left(\Sigma_{11} - \Sigma_{22}\right)^2 + \left(\Sigma_{11} - \Sigma_{33}\right)^2 + \left(\Sigma_{33} - \Sigma_{22}\right)^2} \tag{3.5}$$

with Σ_h and Σ_{eq} being respectively the hydrostatic and equivalent von Mises stresses, has a pronounced effect on damage, localization and fraction.

The stress triaxiality value evolves with the deformation. T value for the standard uniaxial tensile specimen is 1/3 till the onset of necking (see e.g. [71]). After the necking, the stress in that region turns into a complicated triaxial stress condition, and the value of the stress triaxiality increases (see e.g. [66]). The value of stress triaxiality can be controlled in the experimental studies by designing tensile specimens with different notch radius (see e.g. [72]). In this way the effect of the T could be observed in axial fracture samples, which will be done in the following for the RVE case.

Since the triaxiality value during the deformation might change substantially it is quite hard to control the eveolving triaxaiality through boundary conditions applied to the RVE. Therefore, as a simplification, the avarage value can be applied as a constant triaxiality in order to the evaluate its effect on the localization and fracture (see e.g. [73]). In this way the influence of different tensile tests could be simulated in a simple manner. The simulations in this thesis are performed such that the stresses acting on unit cell are proportionally loaded and the stress triaxiality is kept constant at its average value. In order to keep stress triaxiality constant, axial to transverse stress ratio must be kept constant throughout deformation (see e.g. [74]). This can be achieved by applying a set of specific boundary conditions and these boundary conditions should comply with the following statements; the opposite faces of the unit cell must remain straight and stresses acting on opposite faces must be in the oppo-

site direction to enforce periodicity (see e.g. [75]). It is important to note that the mesoscopic shear stress components on the unit cell are taken zero because non-zero components would disrupt the symmetry of unit cell surfaces and stimulate inhomogeneous deformation (see e.g. [74]).

In the finite element calculations performed in this study, axisymmetric tension is imposed on the RVEs while stress triaxiality is kept constant throughout entire loading. T=1/3 corresponds to uniaxial tensile loading. For T>1/3, RVE represents a material point in the centre of the minimum cross-section of a notched tensile specimen, where the stress triaxiality remains more or less constant during deformation.

3.3.1 Constant stress triaxiality by imposing displacement boundary conditions

Boundary conditions representing the stress state of a dual-phase steel, which are valid till the onset of necking, are explained in this section. The edges of the unit cell are aligned with coordinate axes and all edges must remain straight until the end of deformation. In order to satisfy this, a node, M, is used to impose boundary conditions to unit cell surfaces. This node is included in the mesh of the unit cell and placed at the L, L, L coordinates, L being the length of unit cell edges [76]. Placement of node M and unit cell surface names are given in Figure 3.4.

Displacement u_2 in y-direction is applied to node M and resulting u_i displacements of M are coupled to the right, left, front, back and top surfaces in order to keep surfaces straight and to make opposing surface displacements equal. The u_1 displacement of the right surface is coupled to the u_1^M displacement of the node M:

$$u_1(L_1, x_2, x_3) - u_1^M = 0. \tag{3.6}$$

The u_1 displacement of the left surface is coupled to the $-u_1^M$ displacement of the node M since these two displacement vectors show opposite directions:

$$u_1(0, x_2, x_3) + u_1^M = 0. \tag{3.7}$$

The u_3 displacement of the front surface is coupled to the u_3^M displacement of the

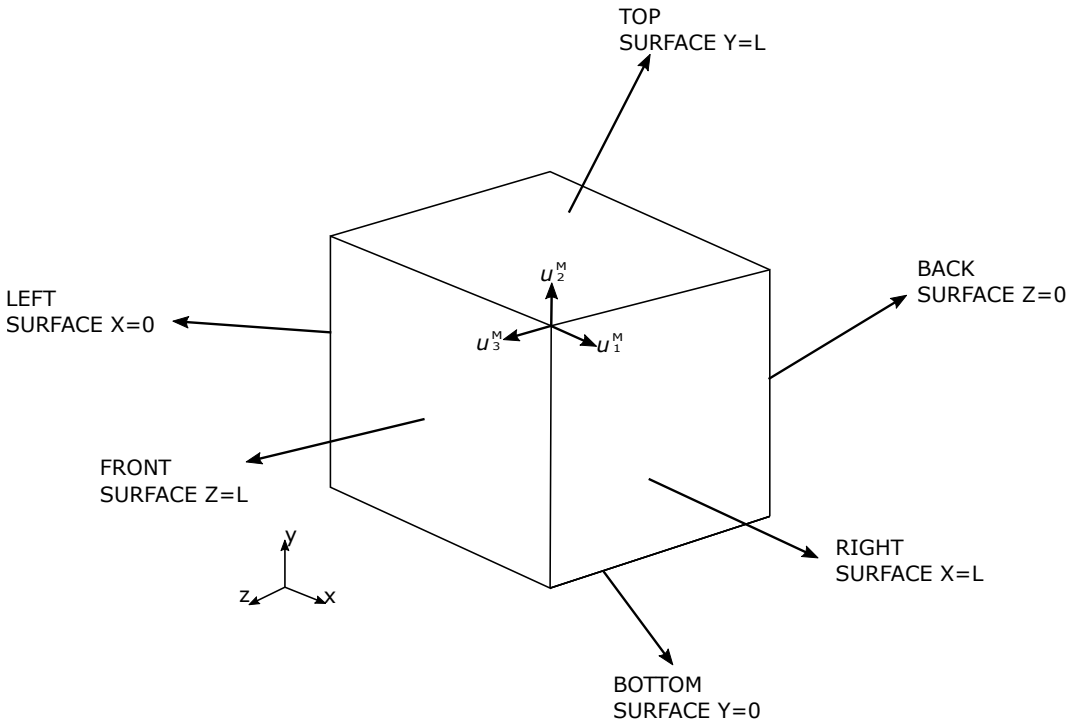

Figure 3.4: A unit cell showing location of node M and surface names.

node M:

$$u_3(x_1, x_2, L_3) - u_3^M = 0. \tag{3.8}$$

The u_3 displacement of the back surface is coupled to the $-u_3^M$ displacement of the node M since these two displacement vectors show opposite directions:

$$u_3(x_1, x_2, 0) + u_3^M = 0. \tag{3.9}$$

The u_2 displacement of the top surface is coupled to the u_2^M displacement of the node M:

$$u_2(x_1, L_2, x_3) - u_2^M = 0. \tag{3.10}$$

The u_2 displacement of the bottom surface is fixed at zero to prevent rigid body motion:

$$u_2(x_1, 0, x_3) = 0. \tag{3.11}$$

With set of equations above, it is ensured that any given displacement to node M will be fully delivered to appropriate unit cell surfaces.

Equations presented in (3.6)-(3.10) are linear constraint equations and can be imposed to cell simulation by "Equation" module of ABAQUS. Linear constrained equations are defined in ABAQUS has the following form

$$A_1 u_i^S + A_2 u_j^Q + ... + A_N u_l^R = 0 \tag{3.12}$$

where N is the number of terms, S, Q, R are node or node sets with i, j, k degrees of freedom with corresponding u_i^S, u_j^Q, u_l^R nodal variables. A_N's define the relative motion between nodes which are coefficients. Therefore Eqs. (3.6)-(3.10) can be easily imposed to simulation model. To avoid errors when using "Equation" refer to [56].

Application of these boundary conditions ensure that all surfaces remain straight while side surfaces are traction free. Therefore T=1/3 condition is satisfied regardless of the applied load or displacement to the node M in y-direction. This method works well for simulations till the onset of necking stress state, 1/3. Another approach is required when the triaxiality is other than 1/3. Such values can only be obtained by applying displacements on transverse surfaces. Therefore displacements on all transverse surfaces must be controlled with ABAQUS Riks algorithm which is explained under section below.

3.3.2 Constant stress triaxiality by using ABAQUS Riks algorithm

This section explains the application of boundary and loading conditions to keep the stress triaxiality constant at any desired value. As mentioned before, having the stress triaxiality constant depends solely on the axial and the transverse stresses. With ongoing deformation, as plastic collapse of the material comes close, applied stresses may decrease therefore it is best to conduct displacement controlled unit cell simulations [74]. ABAQUS offers Riks algorithm that allows simultaneous control over stresses and displacements. The simplified loading condition used for simulations is shown in Figure 3.5.

Loads are exerted in the axial and transverse directions, top and side surfaces re-

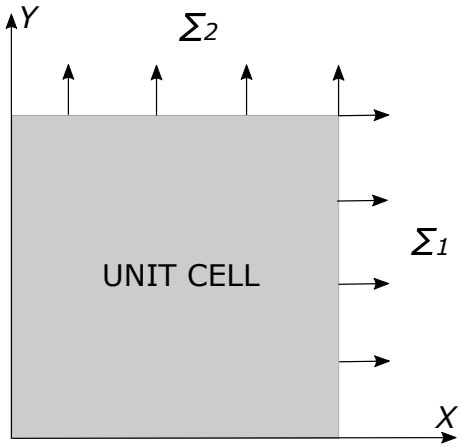

Figure 3.5: A simplified unit cell model and applied loads [74].

spectively. Applied stresses are considered mesoscopic stresses and aligned with the unit cell axes. ABAQUS includes "dload" option that allows specification of axial and transverse distributed loads [56]. First, a brief information on "dload" should be given. Mentioned distributed loads are applied on element faces. Elements used in this study are 10-node quadratic tetrahedron (C3D10) which has 4 element faces and is presented in Figure 3.6. In order to apply "dload" to a specific surface of a unit cell, element faces on the unit cell surface should be determined. Elements on unit cell surfaces are found and grouped in different element sets according to their face numbers. Matlab script for finding necessary element faces is presented in Appendix A.

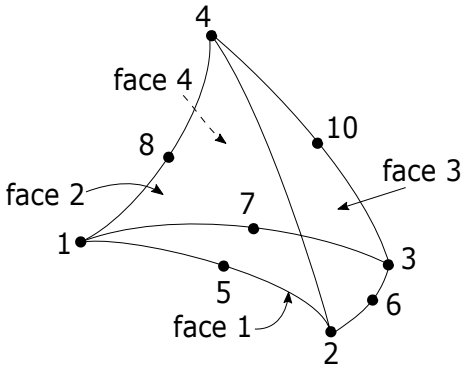

Figure 3.6: Ten node tetrahedral element and corresponding face numbering [56].

The relation between axial and transverse loads is explained next. In order to understand the dependency of one stress to another, the stress triaxiality formulation given

in Eqs. (3.3)-(3.5) are revisited. The mesoscopic stress components on the unit cell are $\Sigma_{11} = \Sigma_{33}$ and Σ_{22} which is in the direction of tension. Therefore the hydrostatic stress in Eq. (3.4) can be expressed as

$$\Sigma_h = 2\Sigma_{11} + \Sigma_{22} \tag{3.13}$$

and the von Mises stress given in Eq. (3.5) becomes

$$\Sigma_{eq} = \Sigma_{22} - \Sigma_{11}. \tag{3.14}$$

Therefore the stress triaxiality is

$$T = \frac{\Sigma_h}{\Sigma_{eq}} = \frac{2\Sigma_{11} + \Sigma_{22}}{3(\Sigma_{22} - \Sigma_{11})}. \tag{3.15}$$

After rearrangements, the transverse stress is formulated as a function of axial stress and stress triaxiality as follows,

$$\Sigma_{11} = \frac{3T - 1}{3T + 2}\Sigma_{22} \tag{3.16}$$

where predominant loading is taken to be applied in the y direction.

Since the investigated microstructure is heterogeneous and consists of two phases, a proper usage of "Equation" module, which is explained under Subsection 3.3.1, is needed to keep the unit cell symmetric and to ensure uniform deformation. In order to enforce periodicity, all faces of the RVE are kept straight during entire loading. For this purpose, three arbitrary nodes, M_1, M_2 and M_3 are selected respectively from the middle of right, top, and front surfaces of the RVE. Placement of the nodes and the surface names are presented in Figure see 3.7. Then u_i displacements of all the other nodes on the surface which contains node M_i are coupled to the u_i displacement of node M_i.Similarly, u_i displacements on the surface opposite to the one which contains node M_i are coupled to the negative value of the u_i displacement of node M_i. These couplings are achieved by the following linear equations

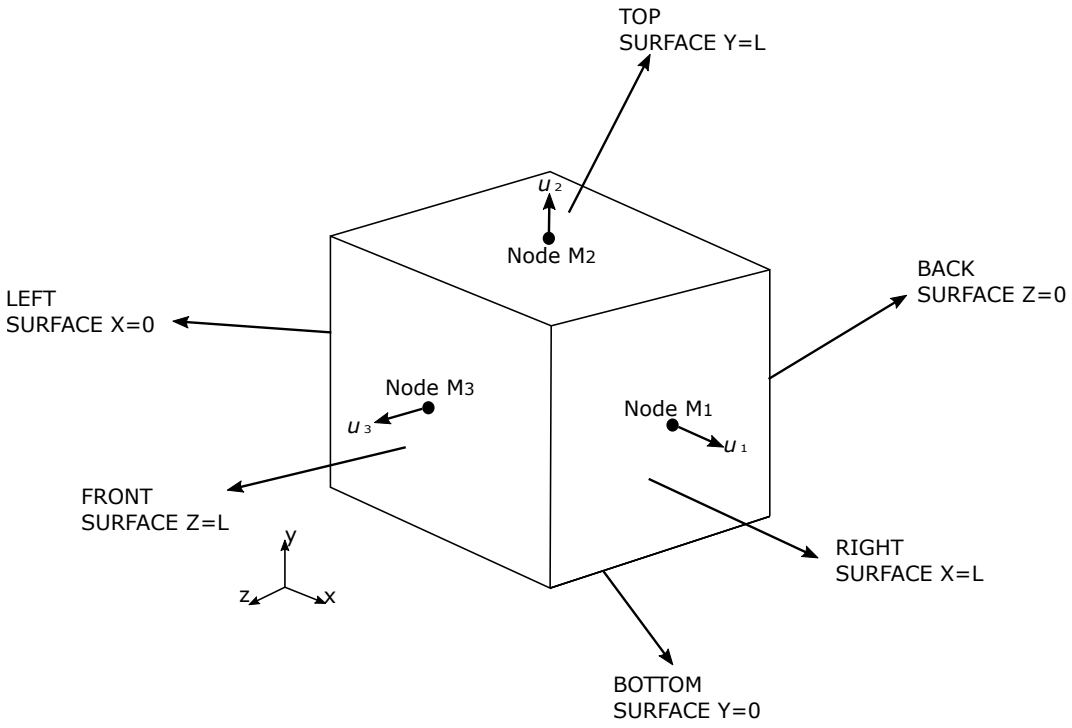

Figure 3.7: A unit cell showing middle nodes M_1, M_2, M_3 and surface names.

Displacement u_1 of node M_1, u_2 of node M_2 and u_3 of node M_3 are coupled to selected surfaces of the unit cell. The set of equations for the application of boundary conditions are explained below. The u_1 displacement of the right surface is coupled to the $u_1^{M_1}$ displacement of the node M_1:

$$u_1(L_1, x_2, x_3) - u_1^{M_1} = 0. \tag{3.17}$$

The u_1 displacement of the left surface is coupled to the $-u_1^{M_1}$ displacement of the node M_1 since these two displacement vectors show opposite directions:

$$u_1(0, x_2, x_3) + u_1^{M_1} = 0. \tag{3.18}$$

The u_3 displacement of the front surface is coupled to the $u_3^{M_3}$ displacement of the node M_3:

$$u_3(x_1, x_2, L_3) - u_3^{M_3} = 0. \tag{3.19}$$

The u_3 displacement of the back surface is coupled to the $-u_3^{M_3}$ displacement of the node M_3 since these two displacement vectors show opposite directions:

$$u_3(x_1, x_2, 0) + u_3^{M_3} = 0. \tag{3.20}$$

The u_2 displacement of the top surface is coupled to the $u_2^{M_2}$ displacement of the node M_2:

$$u_2(x_1, L_2, x_3) - u_2^{M_2} = 0. \tag{3.21}$$

The u_2 displacement of the bottom surface is fixed at zero to prevent rigid body motion:

$$u_2(x_1, 0, x_3) = 0. \tag{3.22}$$

In addition to fixing bottom surface in u_2 direction, its vertices are also fixed in u_1 and/or u_3 directions to avoid rigid body motion.

With the set of equations above, unit cell surfaces remain straight and opposite transverse surfaces have uniform deformation at any constant stress triaxiality value. It is worthwhile to indicate that, mentioned method in this section is also suitable for the case where stress triaxiality is 1/3. The method explained under Section 3.3.1 can be preferred for 1/3 simulations to ease the computational expense.

A small parametric study for the usage of "dload" is presented next. Elastoplastic simulations with 200 grain microstructure are conducted for a constant triaxiality value 1.4. Table 3.1 shows selected axial (Σ_{22}) and its corresponding transverse distributed loads (Σ_{11}, Σ_{33}). After the selection of axial loads, the corresponding transverse loads are obtained through Eq. (3.16). Selected uniform distributed loads are applied to corresponding surfaces through "dload". In Riks algorithm, loading magnitude is a part of the finite element solution, therefore a method should be chosen to specify when the step is completed. As mentioned previously, the simulations are conducted under displacement control, and therefore a maximum displacement value at a specific degree of freedom is entered. A node is selected such that ABAQUS monitors the node for the finishing displacement and terminates the step when maximum displacement is exceeded.

According to different load magnitudes, given in Table 3.1, step termination time changes. As the distributed load magnitude lowers, it takes more computation time to complete the analysis and no convergence was achieved for the lowest load magnitude, which is seen in Trial 1. It should be noted that later simulations incorporating crystal plasticity and Riks algorithm have shown that axial load selections do not

Table 3.1: Axial and transverse load values for "dload".

Trial #	Axial distributed load	Transverse distributed load
1	-1	-0.5161
2	-10	-5.161
3	-100	-51.61
4	-1000	-516.1

cause a remarkable advance in computational time. Equivalent stress vs. equivalent strain and triaxiality vs. equivalent strain graphs that belong to different "dload" values are presented respectively in Figure 3.8(a) and (b) below. Both figures show that, as long as loading values obey Eq. (3.16), results of simulations overlap and do not show any variations. Hence, selection of axial load and dependent transverse load values are up to the user.

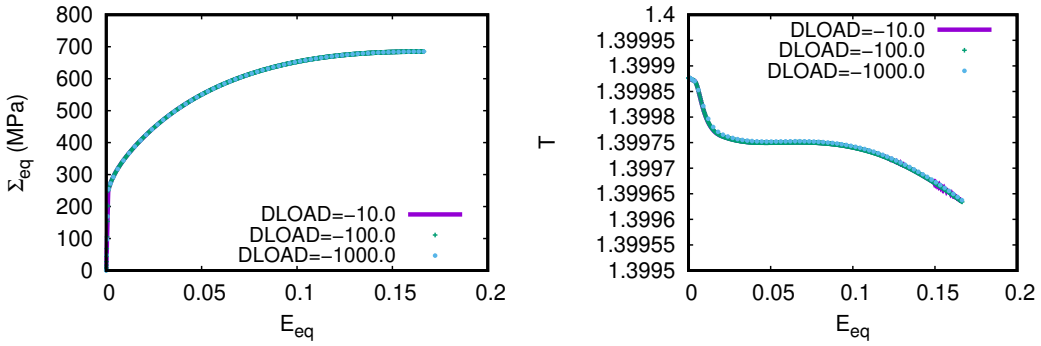

(a) (b)

Figure 3.8: Equivalent von Mises stress vs equivalent strain (a) and triaxiality vs equivalent strain (b) results for different "dload" values.

Aforementioned Σ_{ii} and T parameters are mesoscopic. Parameters that belong to mesoscale are obtained by homogenizing their microscale equivalents. Transition from micro to meso scale with homogenization is described under next section.

3.4 Homogenization

Evolution of internal variables are gathered by applying a homogenization procedure which allows the transfer of micro variables to meso scale. Microscopic and mesoscopic stress and strain values are linked through integral averaging methods of homogenization theory (see e.g. [75]). General form of the equation is presented as,

$$\bar{F} = \frac{1}{V_0} \int_{\mathcal{B}_0} F dV_0 \quad \text{with} \quad V_0 = \int_{\mathcal{B}_0} dV_0 \tag{3.23}$$

where $\bar{F}$ is the mesoscopic and F is the microscopic quantity in a domain $\mathcal{B}_0$ and V_0 is total volume. Homogenization process calculates mesoscopic stresses as the volume average of microscopic components [77], [78].

In order to determine the overall response of the RVEs, the fundamental theorem of homogenization

$$\Sigma_{ij} = \frac{1}{V} \int_V \sigma_{ij} dV \quad \text{with} \quad (i, j = 1, 2, 3) \tag{3.24}$$

is employed, which relates mesoscopic stress tensor components Σ_{ij} for an RVE with a volume V, to the local Cauchy stress components σ_{ij} in the RVE. Accordingly, Σ_{ij} for a RVE is calculated by summing the microscopic Cauchy stresses over every element and its corresponding integration points through

$$\Sigma_{ij} = \frac{\sum_{m=1}^{N} (\sum_{q=1}^{p} \sigma_{ij}^{\{q\}} v^{\{q\}})^{\{m\}}}{V} \tag{3.25}$$

where N is the number of elements, p is the total number of integration points which is 4 for C3D10 elements, and v is the local volume value at the corresponding integration point. The total volume V of the RVE, which remains as a rectangular prism in the entire course of the deformation, is calculated by multiplying the current edge lengths of the RVE: V=L_1 x L_2 x L_3 [76]. After finding corresponding mesoscopic stresses, hydrostatic stress given in Eq. (3.4), equivalent von Mises stress given in Eq. (3.5) and stress triaxiality given in Eq. (3.3) can be obtained at mesoscale.

The mesoscopic principal strain components for the RVE, E_{ii}, are given by

$$E_{ii} = ln\Big(\frac{L_i}{L_{i0}}\Big) \quad \text{with} \quad (i = 1, 2, 3) \tag{3.26}$$

with L_{i0} being the initial edge lengths of the RVE. Then the equivalent von Mises strain is calculated by through

$$E_{eq} = \frac{2}{3\sqrt{2}}\sqrt{(E_{11} - E_{22})^2 + (E_{11} - E_{33})^2 + (E_{33} - E_{22})^2}. \tag{3.27}$$

The presented homogenization procedure is followed as a post processing step through an implemented Python script. The script is presented in Appendix B.

CHAPTER 4

RESULTS AND DISCUSSION

The methodology explained in the previous chapter is followed here to analyze the plasticity and localization behavior of dual phase steel RVEs under axial loading conditions through J2 and crystal plasticity frameworks. In all simulations the homogenization approach is employed to obtain the so-called mesoscopic stress and strain values.

Representative volume elements with 400 grains are generated to illistrate the DP steel microstructure. In each case a different martensite volume fraction, therefore a different morphology is considered. The RVEs are generated according to the provided data in Table 4.1 where V_m, C_m, d_m and d_f represent the martensite percentage, martensite carbon content, martensite grain size, and ferrite grain size respectively. In the initial calculations both phases are assigned to follow J2 plasticity framework with isotropic hardening. Then, in the second part crystal plasticity model is assigned to the ferrite phase. Finally, the effect of both constitutive models are investigated for the selected dual-phase steels at different average stress triaxiality values.

Table 4.1: Microstructural characteristics of investigated DP steels [18].

Steel	V_m (%)	C_m (%wt)	d_f (μm)	d_m (μm)
DP1	15	0.3	6.5	1.2
DP2	19	0.3	5.9	1.5
DP3	28	0.3	5.5	2.1
DP4	37	0.3	4.2	2.4

4.1 Results of uniaxial tensile loading (T = 1/3)

As explained in the previous chapter the Neper software is used to generate the microstructures with the microstructural parameters in Table 4.1 to be used in axial loading simulations. The grain size is an input parameter for the software entered as equivalent diameters for spheres to be generated which are connected in the domain by forming polyhedra. Therefore, each investigated steel morphology and RVE are unique. Artificially generated dual-phase RVEs' martensite volume fractions might not have exact values. Obtained RVEs' martensite volume fractions have a tolerance of $\pm 1.5\%$. Material assigned configurations of DP1, DP2, DP3 and DP4 are given in Figure 4.1, in which green represents ferritic, white represents martensitic phase.

4.1.1 Numerical analysis through phenomenological constitutive relations

In here, rate-independent J2 plasticity with isotropic hardening is applied to both ferrite and martensite phases. The Young's modulus both is E=210 GPa, and the Poisson's ratio is ν=0.3 [19].

The parameter set used for the ferrite flow curves can be seen in Table 4.2, which are identified with respect to experimental results in [18] and [26]. $\sigma_{y0,f}$ is ferrite yield strength, α_f and β are related to initial hardening rate and average ferrite grain size, while θ_f represents the initial hardening rate. θ_{IV} is the stage-IV hardening rate and equals to 100 MPa for all investigated steels. All parameters employed in Eqs. (2.11)-(2.14) to capture ferrite flow behaviour and resulting curves are presented in Figure 4.2 which shows slight differences in yield points. Note that an increasing flow stress is obtained with decreasing grain size.

Individual flow behaviour of martensitic phase is obtained from Eqs. (2.7)-(2.9). The parameter set used for the martensite flow curves are identical in this study and are as follows; a=33 GPa, b=36 GPa, C_0=0.7, q=1.45, n_m=120, C_m=0.3 wt%.

Constitutive response of martensite depends mainly on its carbon content C_m, therefore increasing carbon content increases the initial yield and flow stress [19]. Although for the investigated dual-phase steels C_m value is the same, in order to see the

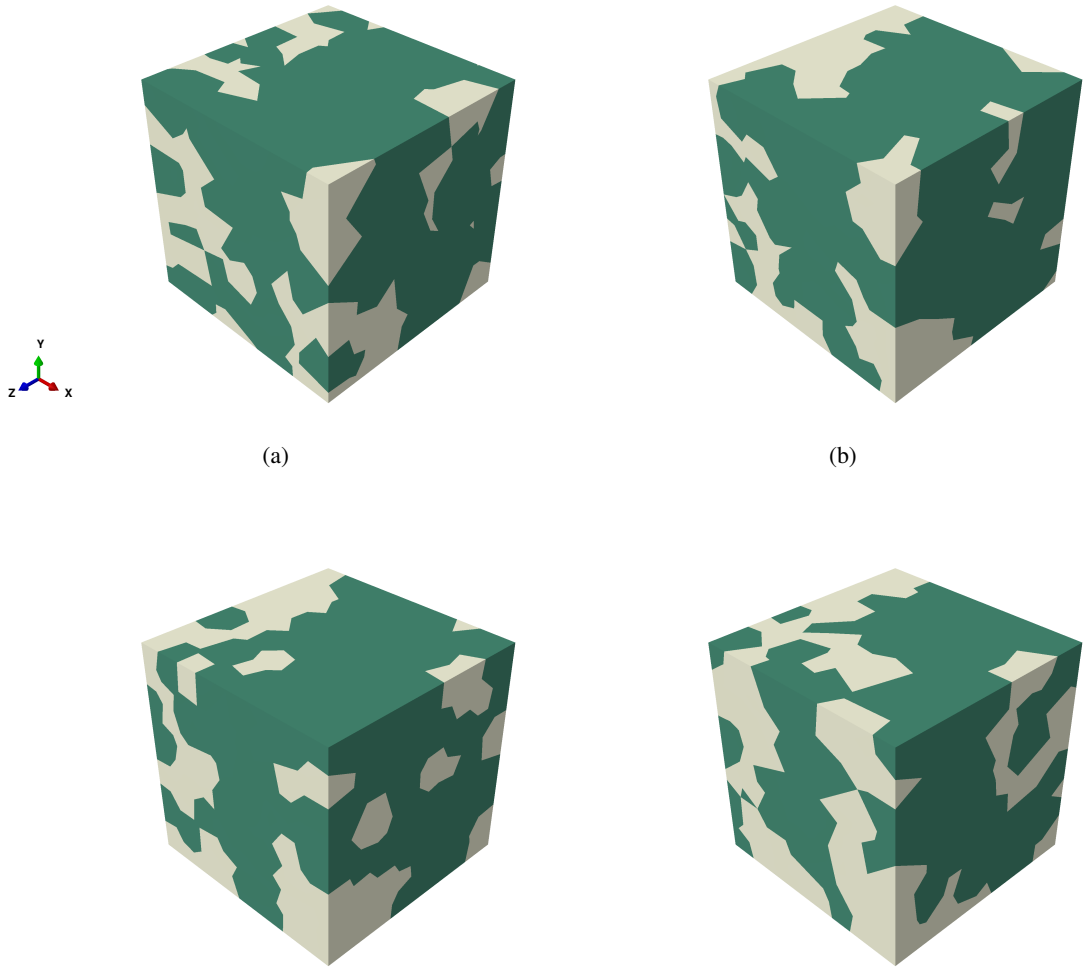

Figure 4.1: Artificial dual-phase steel microstructures DP1 (a), DP2 (b), DP3 (c) and DP4 (d).

Table 4.2: Parameter set used for ferrite flow curves [18], [26].

Steel	$\sigma_{y0,f}$ (MPa)	α_f (GPa)	β (GPa)	θ_f (MPa)
DP1	250	4.9	11	4895
DP2	279	6	13	5980
DP3	300	8.9	17	8925
DP4	307	10.3	20	10260

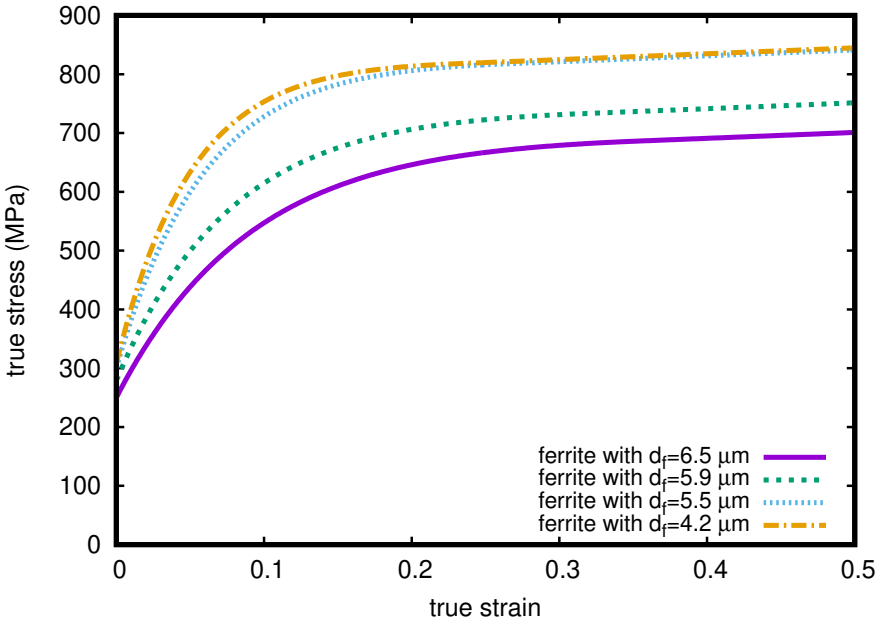

Figure 4.2: Flow curves that belong to ferrite of investigated dual-phase steels.

effect, flow curves of 0.1 wt%, 0.2 wt% and 0.4 wt% are also presented in Figure 4.3. It is once more emphasised that C_m=0.3 wt% for the steels investigated in this work.

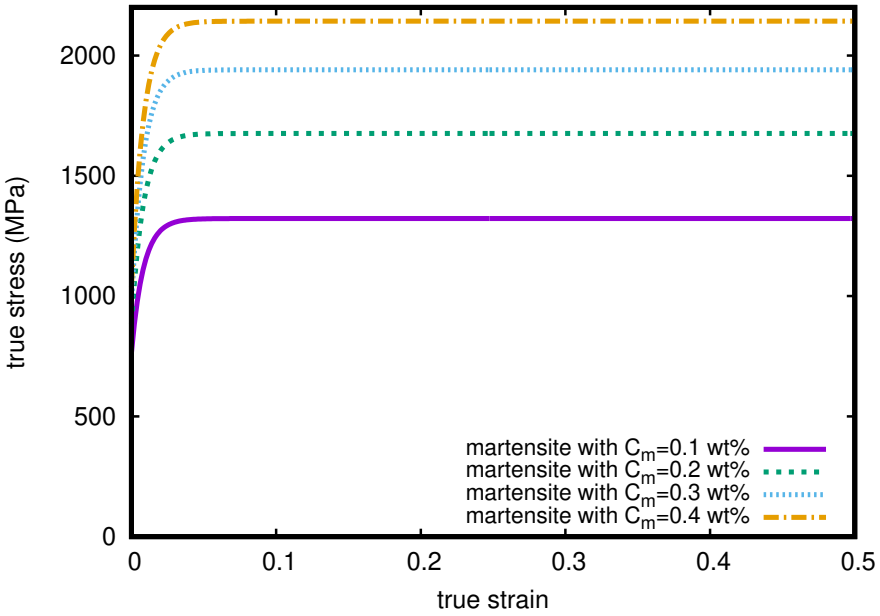

Figure 4.3: Flow curves of martensite with different carbon contents.

Martensite with 0.4 wt% shows flow strength over 2000 MPa, while 0.1 wt% shows

around 1100 MPa. Again 0.4 wt% martensite has an approximate yield point of 1050 MPa, while 0.1 wt% has 750 MPa. C_m influences the maximum flow strength more than the yield strength.

Although the overall behaviour of ferrite and martensite are distinct due to their plastic responses, according to their elastic properties they are equivalent. Yield strength of ferrite is much lower than martensite, therefore ferrite goes into plastic regime earlier. The onset of plastic deformation of ferrite determines the initial yield strength of the dual-phase steel [79]. From the flow responses shown in Figure 4.2 and Figure 4.3, DP1 steel is expected to have the lowest yield and ultimate tensile strength while DP4 will have the highest.

As referred earlier martensite and ferrite material properties and corresponding hardening formulations for the elastoplastic simulations are taken from Lai et al. [18], where the material properties for the flow curves are identified with respect to experimental curves in simple axisymmetric unit cells. The microstructure consists of periodic stack of hexagonal cylinders, each of which contains a single spherical particle. On the other hand in the current study, these parameters are used in RVE simulations which has more realistic two phase grain microstructures. Moreover, the homogenization procedure is also followed here. Therefore it is interesting to compare the current results with the experimental curves using directly the parameters coming from other unit cell calculations.

In this context, uniaxial tension simulations are conducted for DP1, DP2, DP3 and DP4 steels and the obtained overall stress- strain responses are compared to the experimental findings of Lai et al. [18]. Figure 4.4 presents the equivalent stress-strain curves of investigated dual-phase steels till the onset of necking along with experimental results.

The results present a good overall fit. The poorest fit is observed for DP2 microstructure, which slightly overestimates experimental data. However, in general the generated microstructures give the expected material response without any material parameter identification procedure, which gives the confidence to use it in the further analyses.

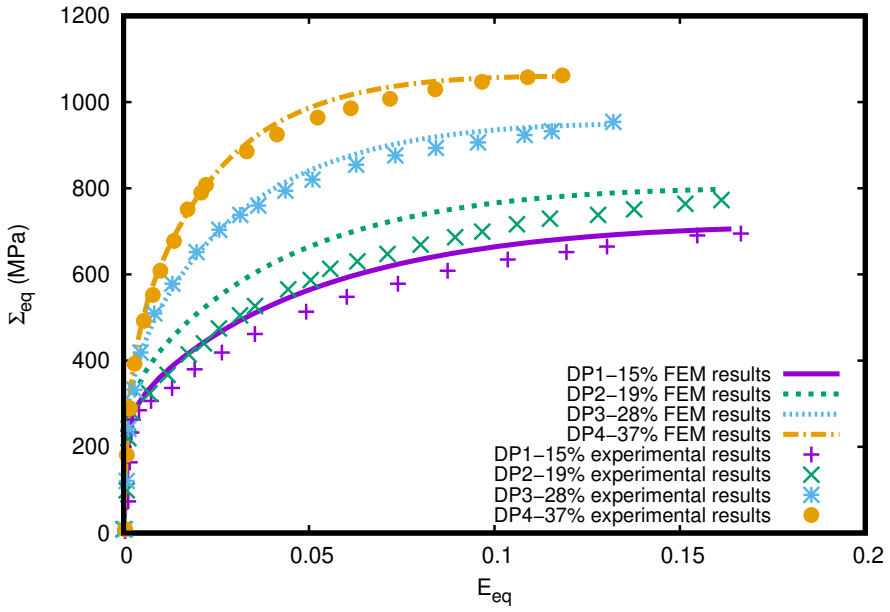

Figure 4.4: Comparison of J2 plasticity based RVE calculation with experimental data up to necking.

Verification of the boundary conditions for the applied uniaxial tension is presented in Figure 4.5 for four different microstructures. They are deformed in the y direction and the stress triaxiality is expected to be 1/3 throughout deformation, which is confirmed in Figure 4.5(a). The mesoscopic strains E_{11} and E_{33} are same up to the third significant figure, and they are almost equal. E_{11}, E_{33} values are nearly equal to $-E_{22}/2$, as presented in Figure 4.5(b) and (c). The mesoscopic strain E_{22}, equivalent strain E_{eq} are also found to be close enough to reflect uniaxial tension of an isotropic material. Differences in these values are due to the existence of two phases and their heterogeneous distribution in the microstructure. According to the these strain values, isotropy of generated RVE is also verified.

Figure 4.6 shows the deformed contour plots of von Mises stress in DP microstructures at equivalent strain value of E_{eq}=0.12 which is the onset of necking for DP4 steel. Heterogeneous stress distribution is observed in all microstructures due to the two phase structure of the material. Ferrite matrix shows different stress values depending on the martensite volume fraction. Stresses larger than ferrite's initial yield stress are observed in all microstructures indicating that ferrite deforms plastically and hardens. As seen in Figure 4.6, stress concentrations occur martensite islands

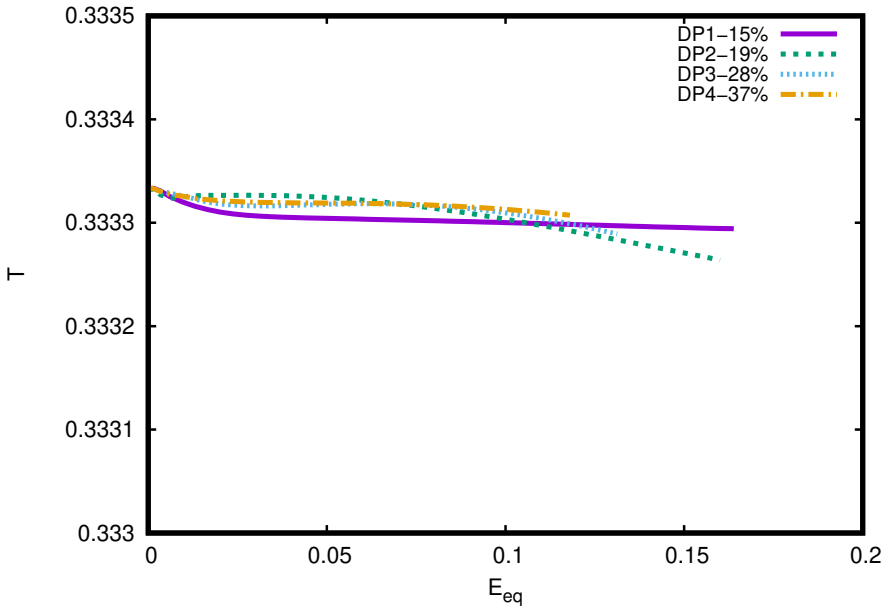

(a)

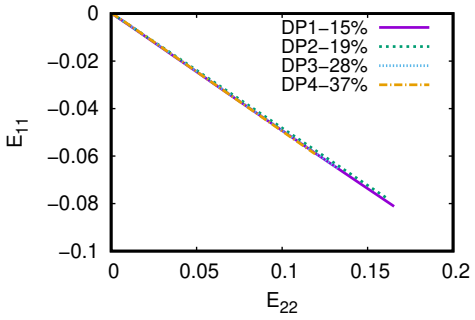

(b)

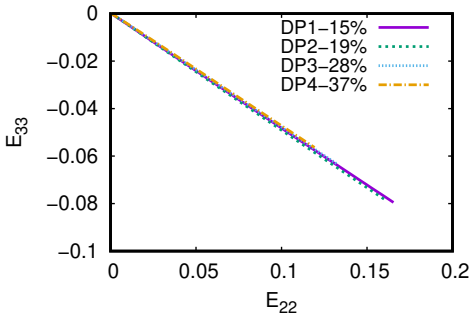

(c)

Figure 4.5: Evolution of (a) the stress triaxiality T and equivalent strain E_{eq}, (b) the mesoscopic strain E_{11} vs E_{22}, (c) the mesoscopic strain E_{33} vs E_{22}.

at their sharp edges, two sharp ends of martensite islands, thin martensite-martensite and ferrite-martensite grain boundaries (see e.g. [16], [32], [39]).These stress accumulations and possible damage sites differ according to DP steel's traits. Since these researches investigate only one or two DP steels, occurring damage regions show differences. The localization points depend highly on the microstructural traits. Lai et al. have conducted multiple experiments and the findings present all previously mentioned damage and fracture locations [26]. The best modelling approach in this regard would be generating RVEs based on real scanning electron microscopy images, which

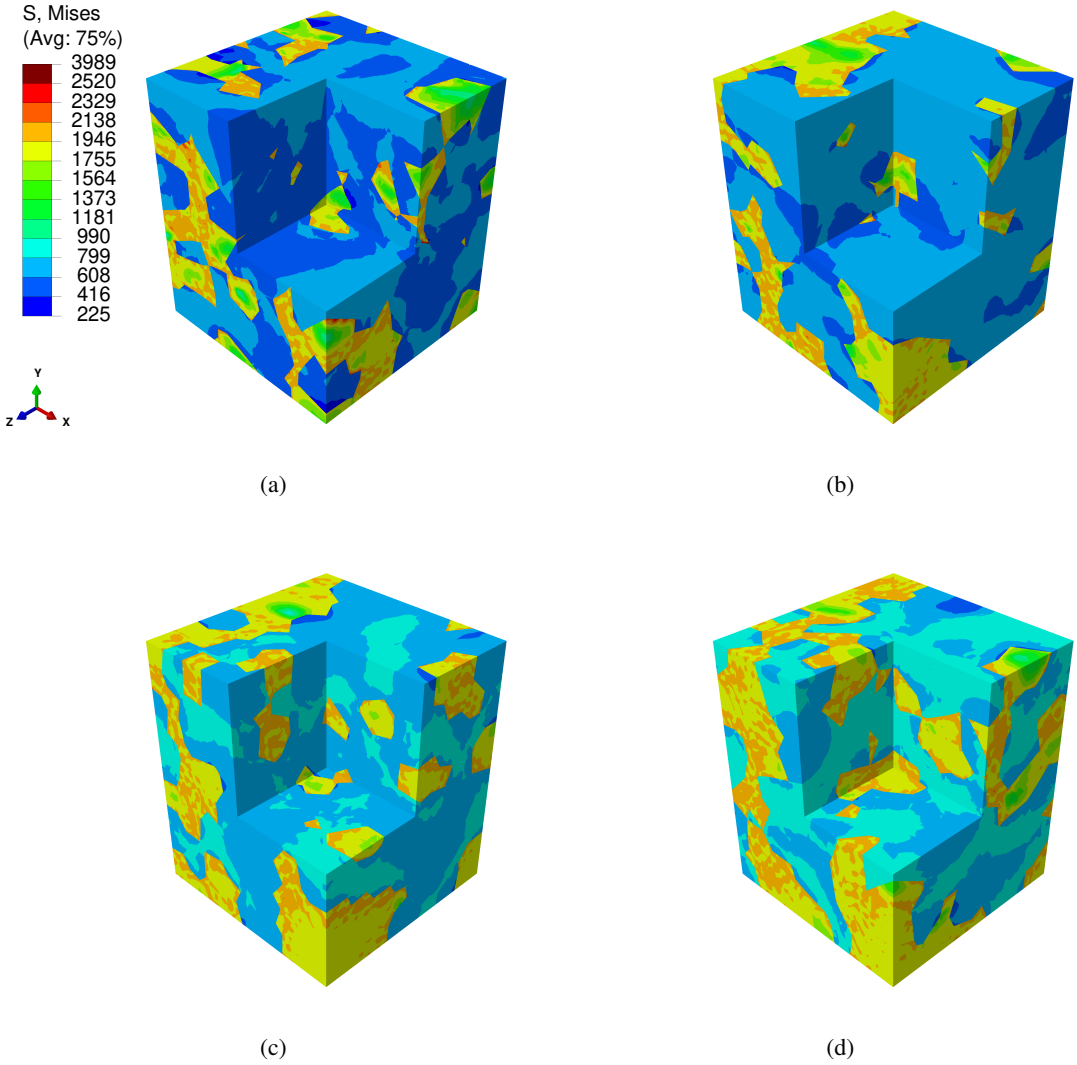

Figure 4.6: Equivalent von Mises stress distributions obtained from J2 plasticity simulations for DP1 (a), DP2 (b) DP3 (c) and DP4 (d).

would give better conclusions on the capacity of computational models. Yet, within this study, highest stress concentrations are observed in the DP4 indicating the lowest ductility and highest strain hardening [21].

Logarithmic principal strain contour plots shown in Figure 4.7 high strain throughout ferrite phase. This contradicts with studies conducted with 2D RVEs which state occurrence of narrow bands [80]. As stated previously by other RVE studies plastic strain localization depends on the plastic material properties, applied boundary conditions and martensite dispersion (see e.g [81]). In such studies both large strain

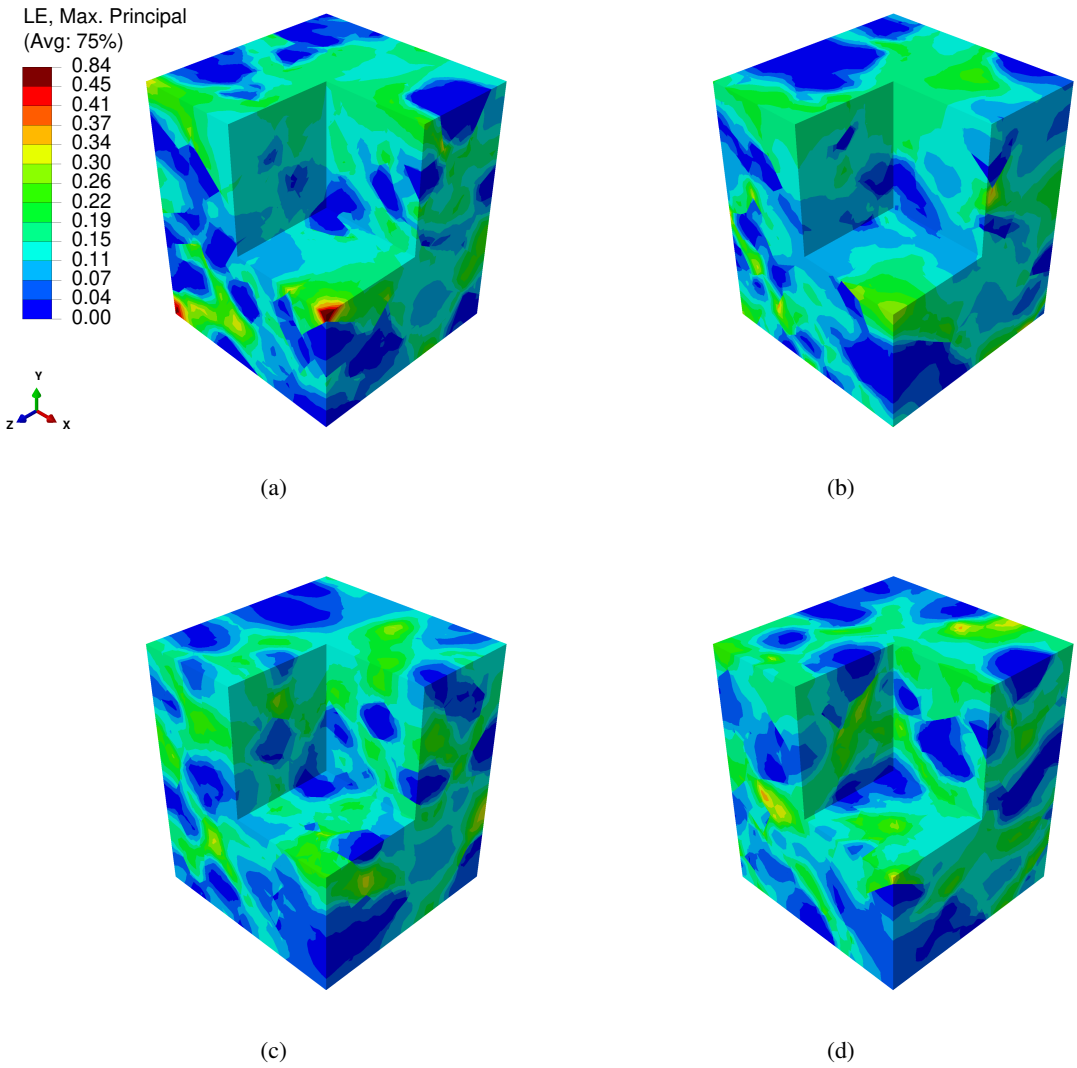

Figure 4.7: Logarithmic principal strain distributions obtained from J2 plasticity simulations for DP1 (a), DP2 (b) DP3 (c) and DP4 (d).

bands throughout ferrite phase (see e.g. [38] for a 3D example) and small localization regions in ferrite located between two sharp ends of martensite and sharp ends of martensite (see e.g. [16]) are observed. In here, no or small straining is seen in martensite particles of DP1, DP2. Some thin martensite-martensite interfaces of DP3, DP4 steels show high strain values. This straining pattern is usually seen in high martensite volume fractions (Vm>32%) according to in situ scanning electron microscopy tests conducted by Ghadbeigi et al. [82]. This unrealistic straining pattern seen in thin martensite-martensite interfaces of DP3 steel is believed to occur

because of the generated RVE.

4.1.2 Numerical analysis through crystal plasticity finite element method

Although J2 plasticity is able to capture the overall stress-strain response and the main microstructural characteristics of the two phase RVE, it lacks capturing the fundamental physical relations between the microstructural parameters and the stress. Therefore, a micromechanics based constitutive model such as crystal plasticity is needed to give a better understanding about the link between the microstructural aspects and the constitutive response and localization leading to damage and fracture. In this context, in order to reflect the effect of the underlying physics of plasticity a crystal plasticity model is employed in this section. In the generated RVE the ferritic phase is assigned with the crystal plasticity model while the previously studied J2 plasticity with isotropic hardening is kept for the martensite islands. All crystal plasticity simulations the {1 1 2} slip family is used.

Crystal plasticity material parameters of the ferritic phase are calibrated before moving on to RVE simulations. The parameters are identified with respect to experimental flow behavior, which was studied previously by J2 plasticity using the Eqs. (2.11)-(2.14). Initially, the procedure is applied for the case with 6.5 μm and 1.2 μm martensite grain size corresponding to DP1 material. The parameters of the ferritic phase are identified using a 200 grain unit cell composed of randomly oriented ferrite grains shown in Figure 3.2. Considering ferrite is cubically anisotropic, the elastic constants for crystal plasticity unit cell simulations are chosen as follows; C_{11}=231.4 GPa, C_{22}=134.7 GPa and C_{44}=116.4 GPa (see e.g. [46]). After obtaining the ferrite material parameters for the DP1, the same set is used in the simulations for the other dual phase steel RVEs (DP2, DP3 and DP4) in order to the see if the effect of martensite volume fraction is enough to predict the overall response. The results are presented in Figure 4.8 and it is clear that the agreement is not good, especially for the case with high martensite volume fraction which corresponds to low ferrite grain size. Note that the the influence of the grain orientations, the morphology, and the grain size effect are all hidden in these results which do not fit perfectly with the experimental ones. Therefore one material parameter set for the ferrite is not enough

for a local crystal plasticity model to predict the overall response.

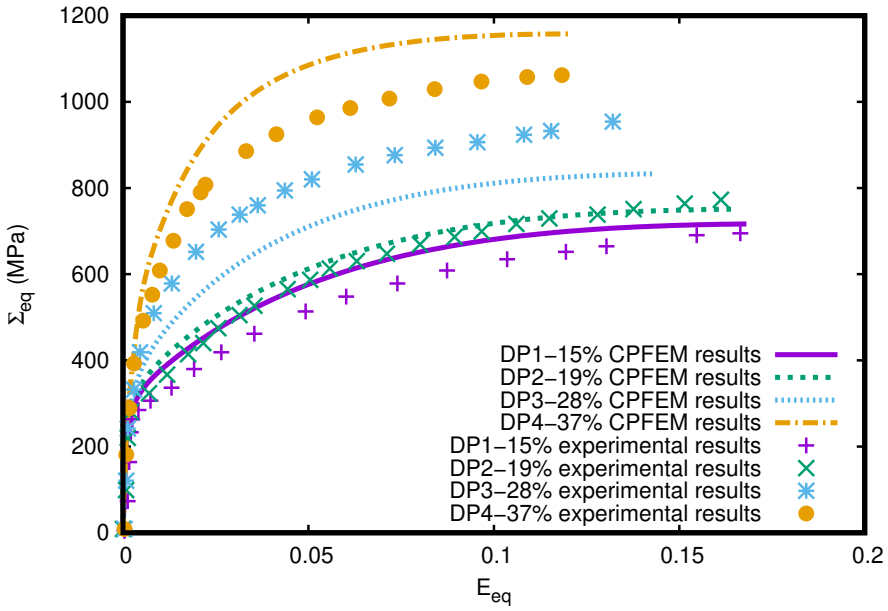

Figure 4.8: Crystal plasticity simulations(CPFEM) solutions of DP steels with crystal plasticity parameters of 6.5 μm.

The The Hall–Petch effect plays an important role here. Therefore the users should either use a size dependent crystal plasticity model (see e.g. [83], [84], [85]) in order to take into account the effect of the grain size. Or, as it is conducted here, the local crystal plasticity hardening parameters must be calibrated for different ferrite grain sizes. Hence, the procedure followed for 6.5 μm is repeated for the case with 5.9 μm, 5.5 μm and 4.2 μm sized grains, which correspond to DP2, DP3 and DP4 RVEs respectively. The same procedure is applied for the material parameter identification and the hardening parameters calibrated to be used in crystal plasticity simulations are presented in Table 4.3, where, s_0 is the initial slip resistance representing the effect of yield strength, s_s is the saturation slip resistance representing the maximum stress, and h_0 is the hardening parameter governing hardening behaviour. Note that the viscoelastic parameter m and reference slip rate $\dot{\gamma}_0$ are taken 60 and 0.001 respectively. A high value for m is considered in order to minimize the rate dependency of the crystal plasticity model [51]. The pure ferrite response of the crystal plasticity simulations are compared with the (experimentally identified) J2 ones in Figure 4.9.

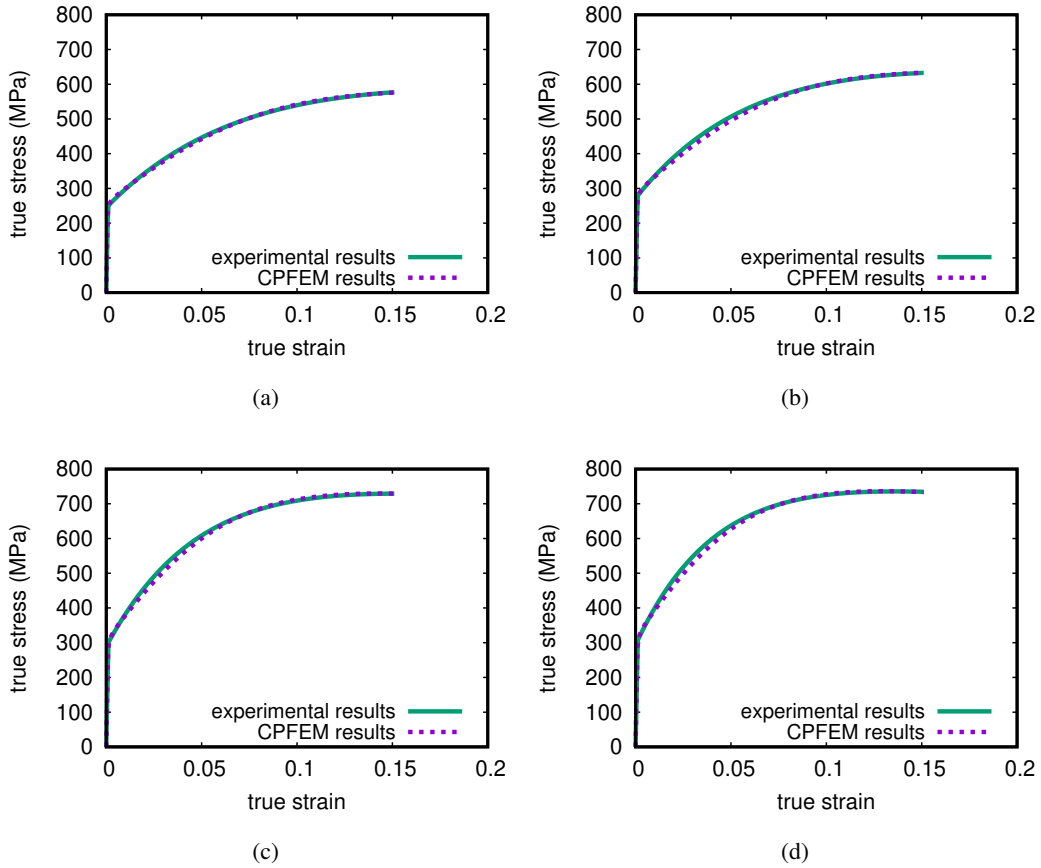

Figure 4.9: Comparison of ferrite cell J2 and CPFEM simulations with with calibrated crystal plasticity parameters for ferrite grain sizes of 6.5 μm (a), 5.9 μm (b), 5.5 μm (c) and 4.2 μm (d).

Comparison of the homogenized CPFEM equivalent stress-strain response and the experimental results of different dual-phase steels are presented in Figure 4.10. n this case the simulations are conducted with optimized ferrite parameter sets for each

Table 4.3: Final calibrated crystal plasticity coefficients for ferrite.

Steel	$d_f(\mu\text{m})$	s_s (MPa)	s_0 (MPa)	h_0 (MPa)
DP1	6.5	252	98	475
DP2	5.9	275	109	555
DP3	5.5	306.6	118.5	802.8
DP4	4.2	305	121.5	880

grain size and they naturally give better results. However, the current results slightly overestimates the ones obtained from J2 plasticity model, provided in Figure 4.4. Note that in these simulations only the parameters for ferrite CPFEM model and the ones for martensite flow rule are identified with respect to their single phase experimental behaviour. Afterwards these values are used in the created RVEs which include random grain orientations and martensite morphology. Even though at these length scale such microstructural parameters play crucial roles, the obtained material response shows a quite good fit compared to experimental macroscopic studies.

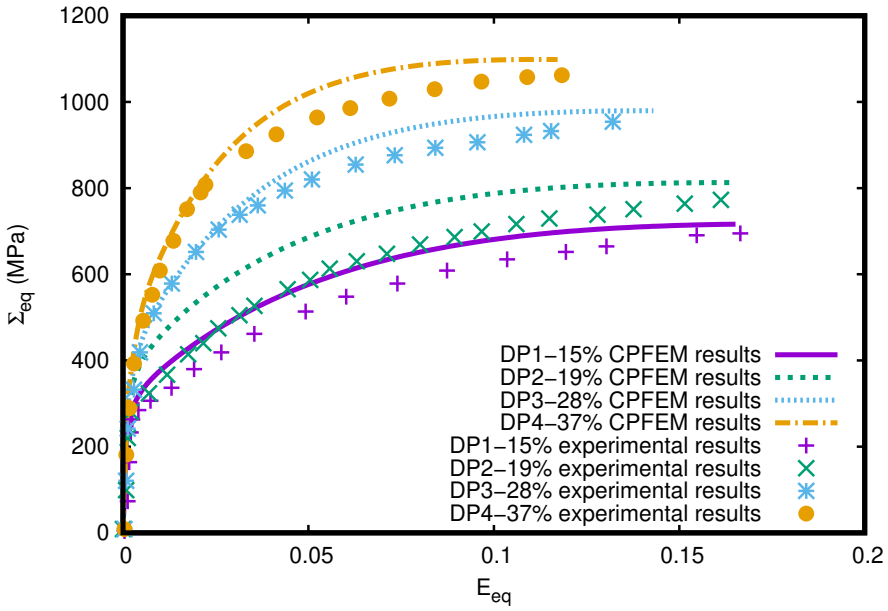

Figure 4.10: CPFEM solutions of DP steels with calibrated parameters given in Table 4.3.

The verification of applied boundary conditions and simulated uniaxial tension in y direction can be seen in Figure 4.11. Due to the nature of uniaxial tension, $E_{11} = E_{33} = -E_{22}/2$ and $E_{22} = E_{eq}$ conditions are expected to be ensured. Although previous elastoplastic simulations have given convenient results, due to the anisotropy of the applied crystal plasticity model, higher deviations are observed as presented in Figure 4.11.

Contour plots of investigated dual-phase microstructures are studied next. Figure 4.12 shows the deformed contour plots of simulated DP steels at equivalent strain E_{eq}=0.12 which is the onset of necking for DP4 steel.

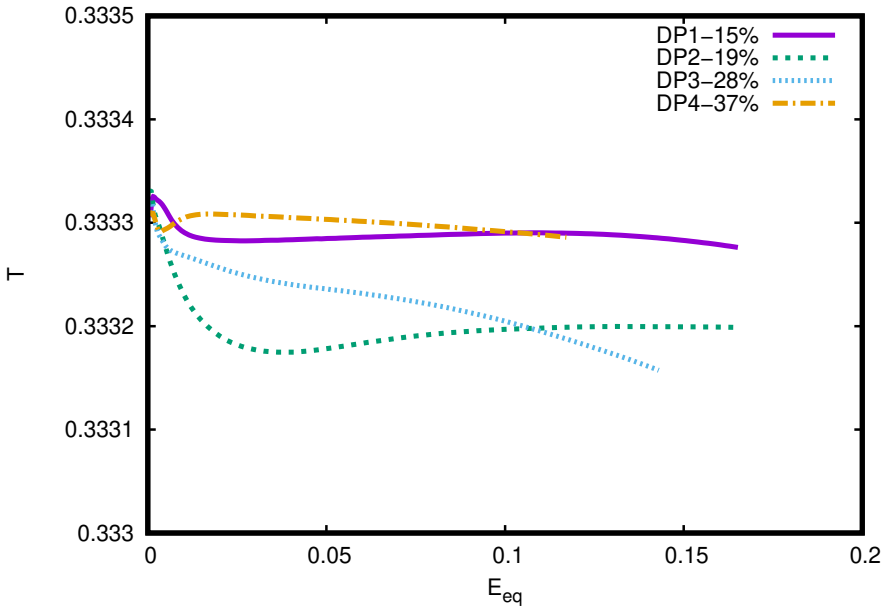

(a)

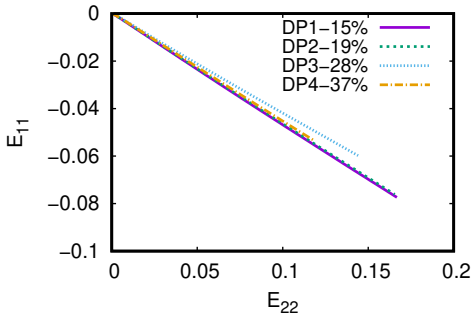

(b)

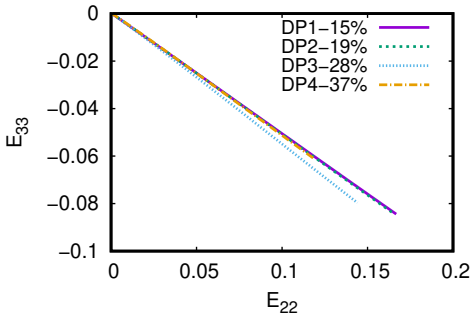

(c)

Figure 4.11: Evolution of (a) the stress triaxiality T and equivalent strain E_{eq} (b) the macroscopic strain E_{11} vs E_{22}, (c) the macroscopic strain E_{33} vs E_{22}.

The spatial distribution contour plots of equivalent stress and logarithmic principal strain are presented in Figure 4.12 and 4.13 respectively. Compared to the results obtained from J2 plasticity, which is illustrated in Figures 4.6 and 4.7, similar results are observed for strain distribution but considerable differences exist for the stress evolution in terms of both amount and heterogeneity. Crystal plasticity simulations result in higher stress values in general, which can be due to the stress concentrations that occur at the ferrite grain boundaries because of orientation mismatch. This phenomenon does not exist in J2 plasticity simulations as the grains do not possess any

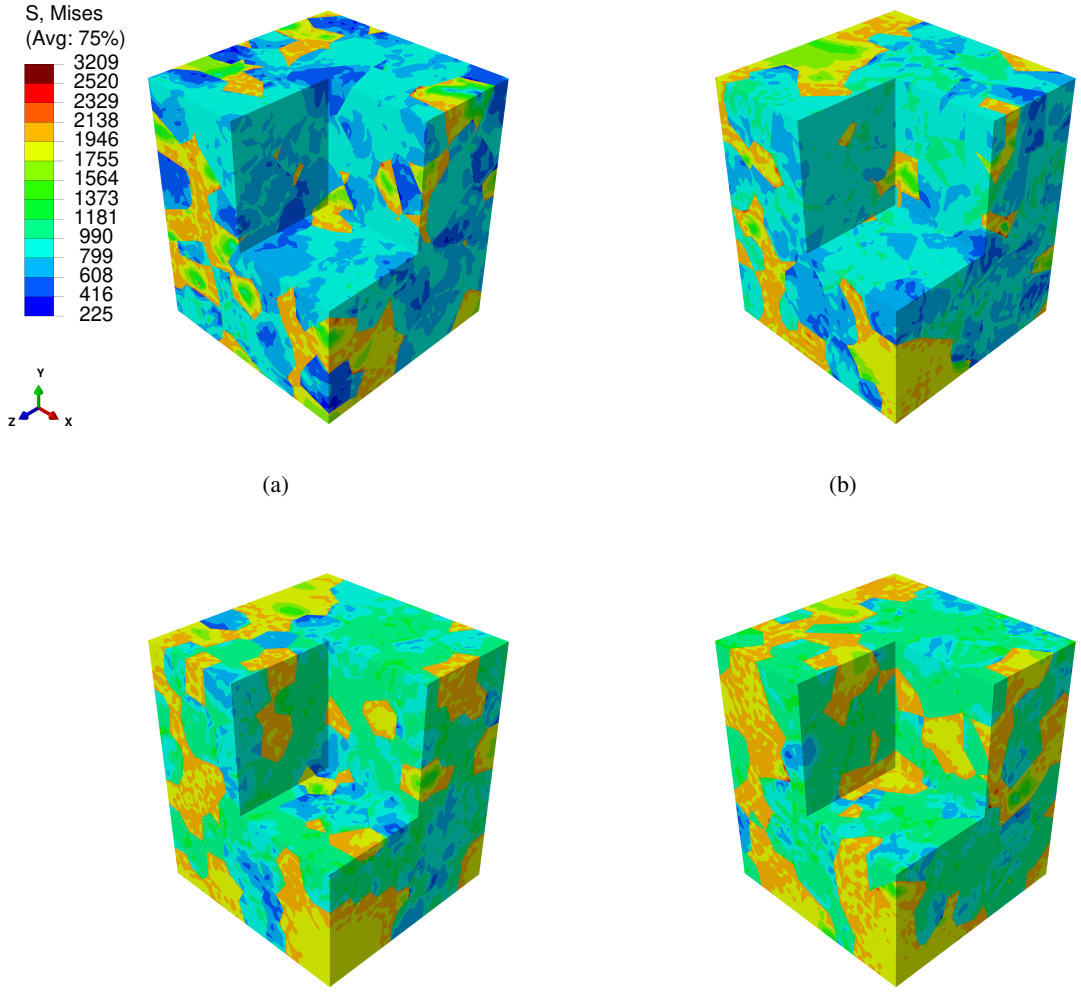

Figure 4.12: Equivalent von Mises stress distributions obtained from CPFEM simulations for DP1 (a), DP2 (b) DP3 (c) and DP4 (d).

orientation information. Therefore this physical reality cannot be illustrated through a phenomenological model, even it is reflected to an upper scale in a slightly exaggerated manner through CP simulations. Amount of the stress and deformation heterogeneity alter according to the ferrite microstructure and the identified parameter sets. Furthermore even though the local stress evolution trend is quite similar, due to random orientations, CPFEM gives more heterogeneous stress distribution in ferrite which has an effect on the state in martensite as well. High stress accumulated regions in martensite show similarities to J2 plasticity solutions and consistent with

previously mentioned literature. These localizations are broader when compared with J2 plasticity stress contour plots.

Figure 4.13 shows the distribution of the logarithmic principal strain of investigated dual-phase microstructures. Localization is observed in the ferrite matrices of all microstructures, especially at the sharp ends of martensite and between the sharp ends of martensite islands, some of which are not observable in J2 plasticity simulations. Although contour plots are similar, additional localized regions occur nearby martensite due to random crystallographic orientations of ferrite [46].

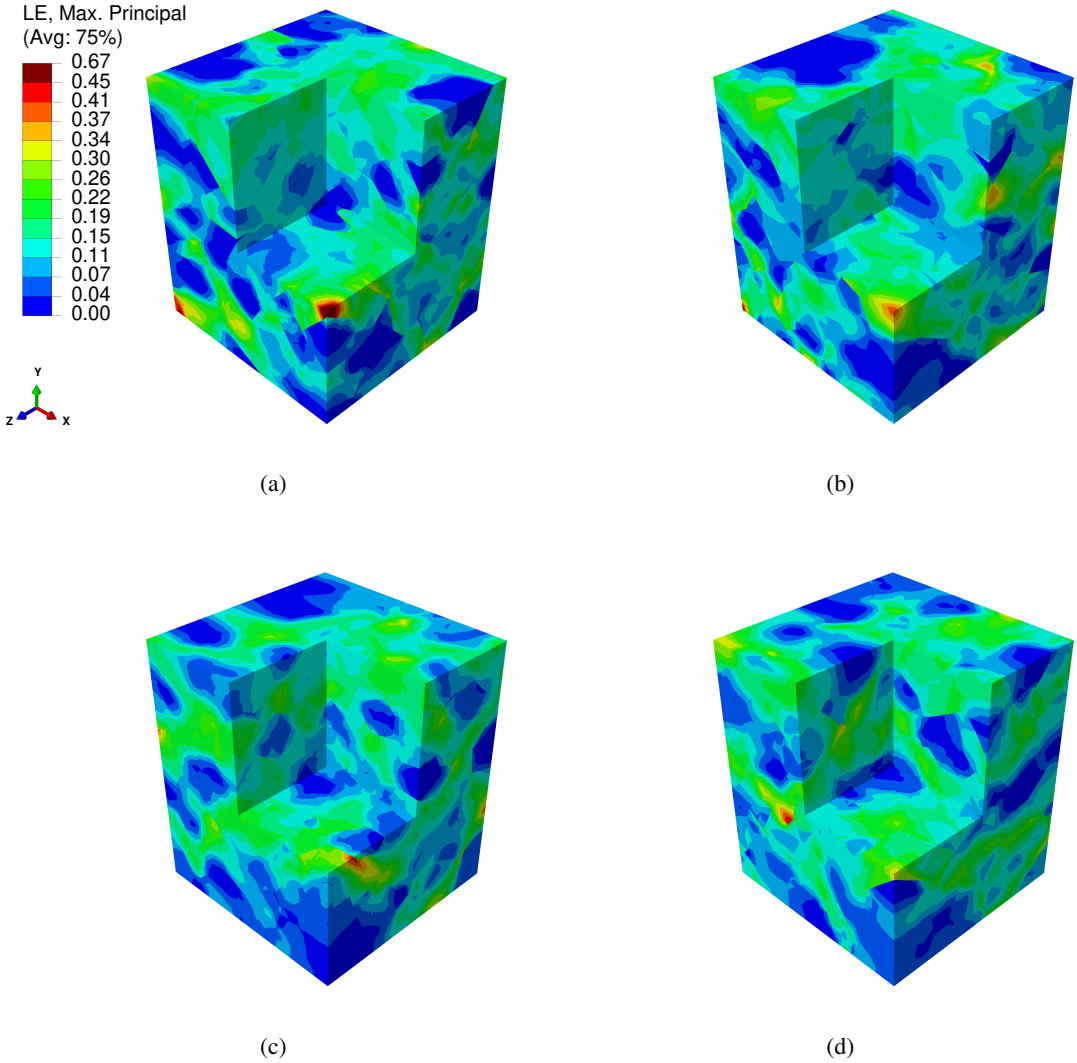

Figure 4.13: Logarithmic principal strain distributions obtained obtained from CPFEM simulations for DP1 (a), DP2 (b) DP3 (c) and DP4 (d).

4.1.3 Comparison of J2 plasticity and CPFEM results

The purpose of this section is to compare explicitly the spatial results obtained from J2 plasticity approach and the crystal plasticity micromechanical model. Section cuts from DP2, are plotted in order to investigate differences in stress and strain evolution and localization. Localization patterns are compared at DP2's onset of necking strain value of 0.16.

Figure 4.14 illustrate the comparison of stress distribution. Ferrite in J2 plasticity solutions shows less variations in stress distributions and therefore has a more homogeneous pattern. Ferrite with crystal plasticity shows heterogeneously spread higher stresses. Heterogeneous stress distribution is caused by randomly assigned orientations. Incompatible grain orientations causes the evolution of high stress concentrations at the grain boundaries which lead to high stresses. These differences observed in ferrite, reflect slightly on the martensite stress distribution as well. For both solutions, high stress accumulated regions in the martensite are mostly the same, which are thin martensite sections and sharp martensite ends. Although stress accumulation patterns are similar, due to orientation mismatch the value of the stresses in the martensite islands are amplified as well.

Comparison of J2 and CPFEM logarithmic principal strain solutions are given in Figure 4.15. Strain localization that occurs in J2 plasticity solutions do not necessarily overlap with strain localization obtained from CPFEM solutions. Some additional strain localization regions are observed in ferrite microstructure in CP case. Initial orientation of ferrite grains influences considerably the strain accumulations (see e.g. [46] for similar conclusions). Ferrite grain orientations also affect the strain distributions inside and nearby martensite islands. In order to make a more thorough analysis of the grain orientation influence, various random orientation sets can be assigned to ferrite phase for dual-phase simulations. However the purpose here is to make a simple comparison between the two modeling techniques.

Overall, J2 plasticity is numerically more efficient and satisfactory for macroscopic conclusions. On the other hand, numerically more expensive, crystal plasticity simulations take into account the effect of different microstructural parameters and give

more realistic results at the micro scale. Both models give similar macroscopic results while considerable differences are observed at contour plots.

4.2 Results of axisymmetric tensile loading ($T \geq 1/3$)

Dual-phase steels are prone to several different failure mechanisms which may occur simultaneously. Ductile failure in ferritic phase (see e.g. [17]), brittle fracture in martensitic phase (see e.g. [27]) and interface debonding in between the phases (see e.g. [28]), are identified as main failure mechanisms of dual-phase steels. Martensite volume fraction is the key factor that determines the dominant failure type (see e.g. [26], [57]). Although the aforementioned damage and fracture processes are observed as physical initiation phenomenon at micro scale, it does not reflect directly to macro scale as the main failure mechanism. Many studies have concluded that ductile macroscopic failure by localized necking is the dominant mechanism for dual-phase steels (see e.g. [16], [18], [66]). Ductile failure in dual-phase steels starts with nucleation of micro voids, afterwards these nucleated voids grow, grown voids merge and finally cause material to rupture [17]. However the void initiation mechanism depends on the microstructure and martensite volume fraction.

This section aims to study the effect of triaxiality on the plastic localization and ductile damage initiation, which is directly linked to micro void nucleation, growth and coalescence which is a well-known fact nowadays. The effect of the triaxiality on the ductility has been studied in notched specimens under different triaxiality conditions (see e.g. [62], [70], [72], [86]). Triaxiality evolves throughout the deformation in tensile specimens. It actually stays constant as 1/3 till the onset of necking, then increases after necking and shows peak values in the presence of notches and cracks. Various studies concentrated on this issue in dual phase steels as well. As for the relation between the stress triaxiality and the evolution of ductile damage, it is found that, with increasing triaxiality, total volume fraction of voids show a considerable increase while nucleated voids distribute independent of stress triaxiality (see e.g. [66], [67]). Triaxiality and displacement values are obtained from shear, upsetting and tensile experiments. Initial and final data of each test are used to find average triaxiality values. Afterwards, numerical simulations are conducted by imposing average stress

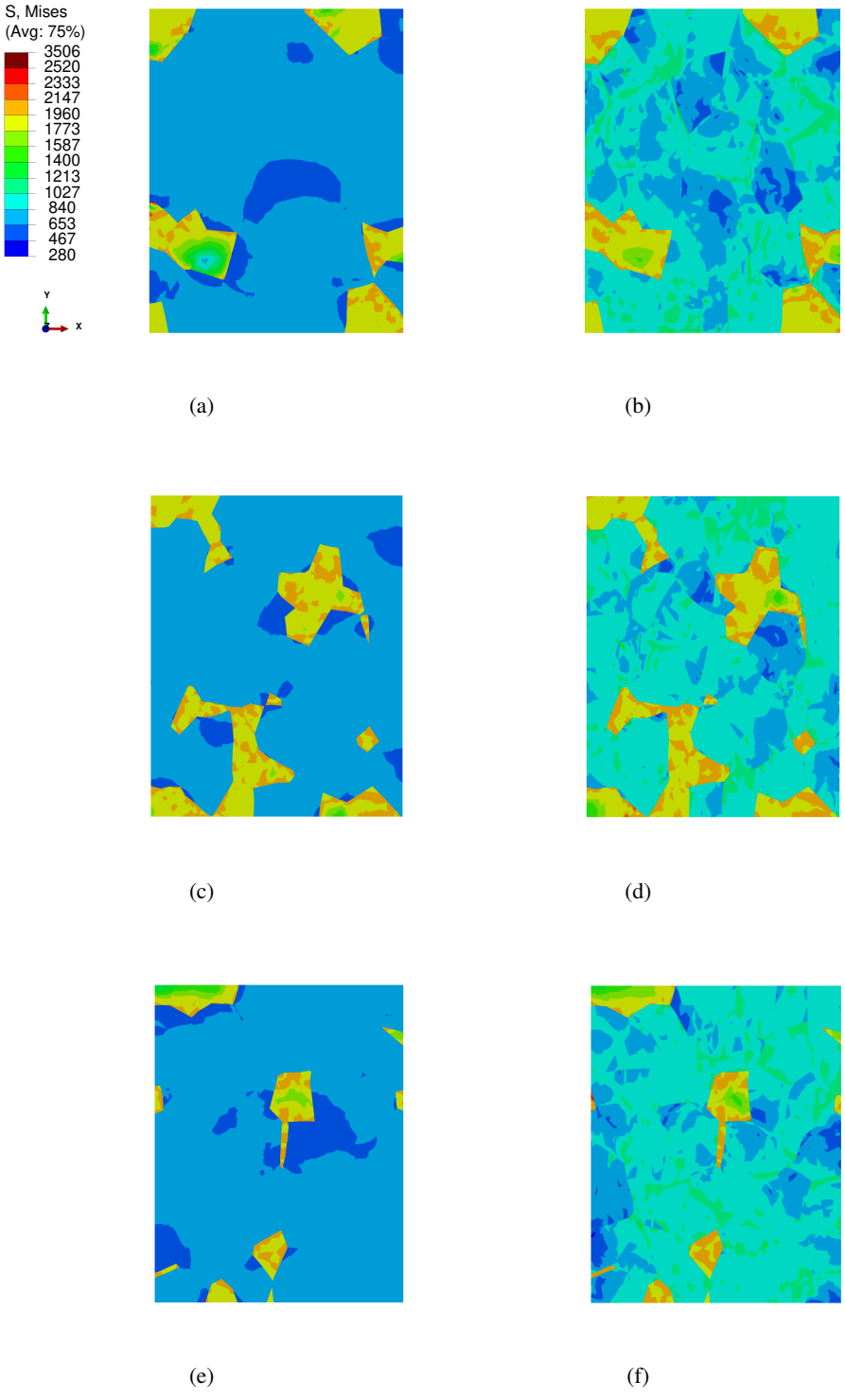

Figure 4.14: Comparison of equivalent von Mises stress distribution for DP2 obtained from J2 (a,c,e) and CPFEM (b,d,f).

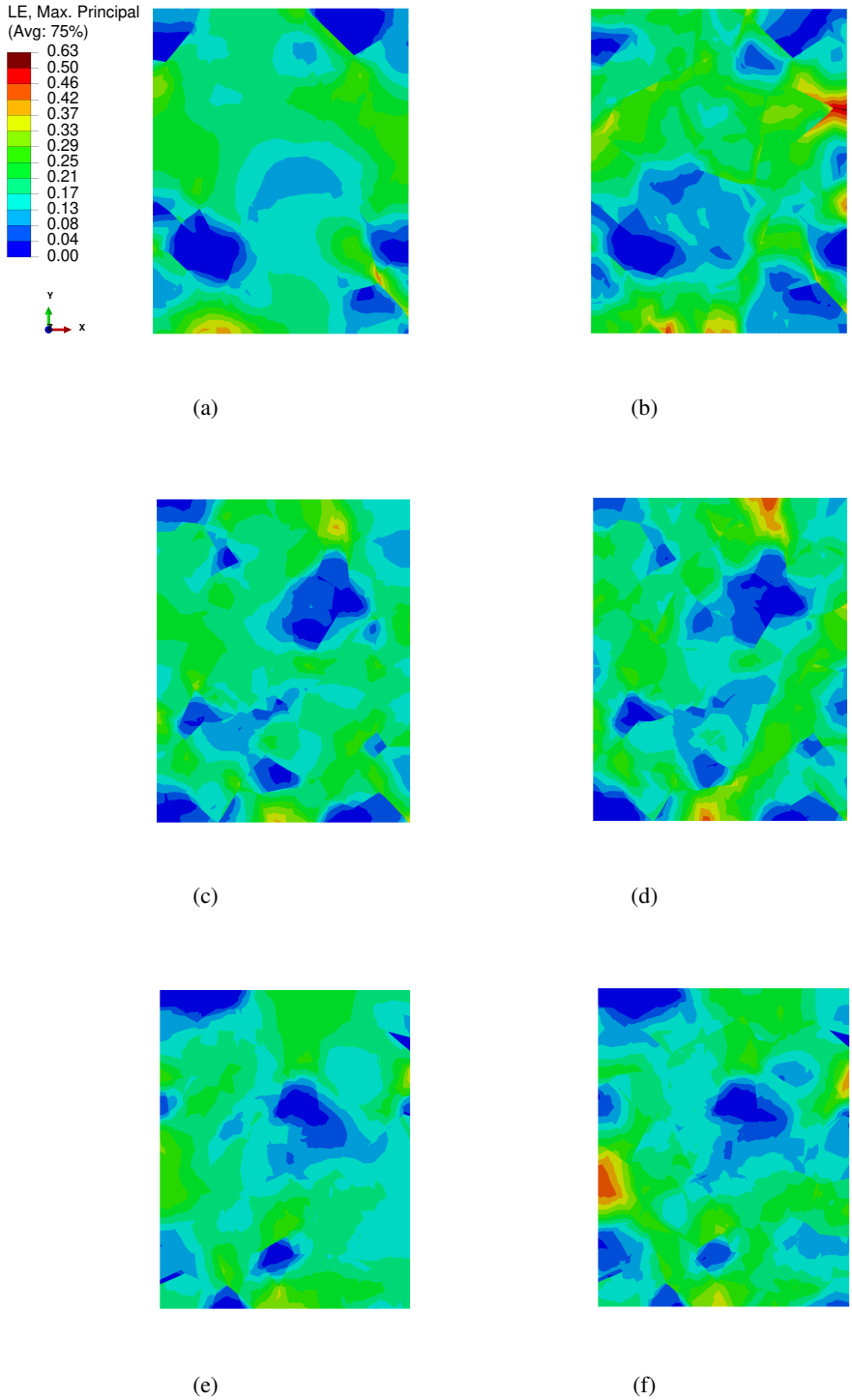

Figure 4.15: Comparison of logarithmic principal strain distribution for DP2 obtained from J2 (a,c,e) and CPFEM (b,d,f)

triaxiality values to the model. Correlation between experimental and simulated results are found to be satisfactory. It is observed that fracture ductility is inversely proportional to triaxiality. High triaxial stress states cause low fracture strains due to void formation in tensile tests (see e.g. [73], [87]).

In this context, the overall stress triaxiality in the RVE simulations is kept constant here in order to reflect its influence on the void formation, therefore on ductile damage and fracture. Keeping the stress triaxiality at a constant value is already studied in Section 3.3.2. It is suggested that proper transverse and axial loading is the key factor for obtaining constant stress triaxiality. Due to the application of simultaneous axial and transverse loads and resulting large displacements, instability in the stiffness behaviour occurs. To overcome the convergence issues caused by the unstable load displacement response Riks algorithm is used, which allows the application of incremental loads under displacement control. Transverse and axial stresses are applied to RVE surfaces in the forms of distributed loads by using "dload" of ABAQUS [56]. Transverse loading values vary according to chosen average T values 0.33, 0.5, 1, 1.5 and 3. Since the results for the different microstructures provide similar conclusions, only the results that belong to DP1, with lowest V_m, and DP4, with highest V_m, are presented. Equivalent stress and strain data from J2 plasticity and CPFEM solutions of DP1 steel is presented in Figure 4.16. The value of triaxiality does not affect the equivalent stress-strain response. That is because of the fact that constitutive behavior here is independent of varying triaxiality [34].

Stress-strain response plots in the axial loading direction are presented in Figure 4.17. The requirement for the use of Riks algorithm for different triaxiality values can be seen in this figure. Axial stress values increase dramatically with increasing stress triaxiality. In the case of T=0.33, Σ_{22} is equal to Σ_{eq}, as expected. As T value changes, Σ_{22} becomes higher than Σ_{eq}. Static general analysis solver of ABAQUS gives large displacements as the response of large loading scenarios which eventually leads to no or undesired results.

The validation of obtained triaxiality values throughout the deformation are presented for DP4 microstructure in Figure 4.18. Riks algorithm, J2 plasticity (through FEM) and CPFEM solutions provide satisfactory results and show an equivalent trend as

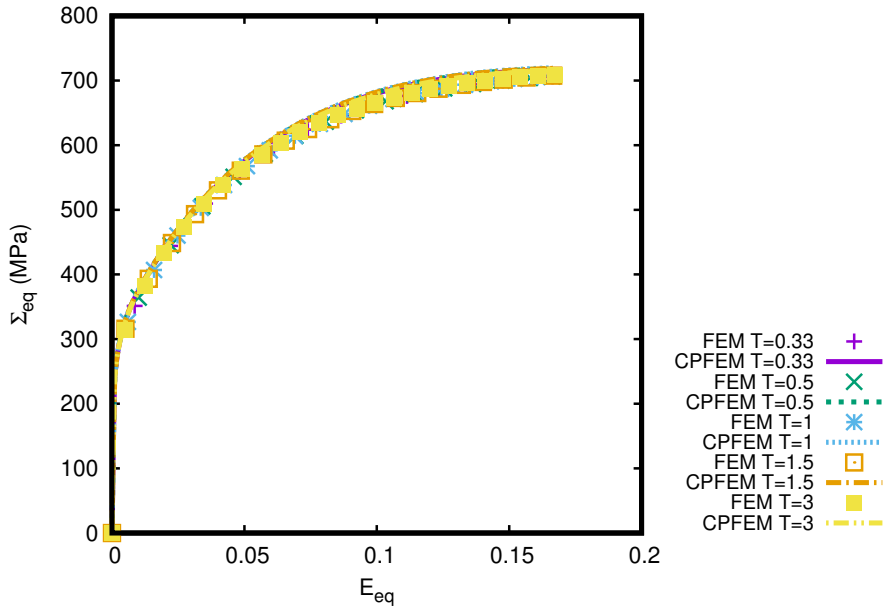

Figure 4.16: Comparison of J2 and CP equivalent stress strain responses for DP1 steel obtained for 0.33, 0.5, 1, 1.5 and 3 average triaxiality simulations.

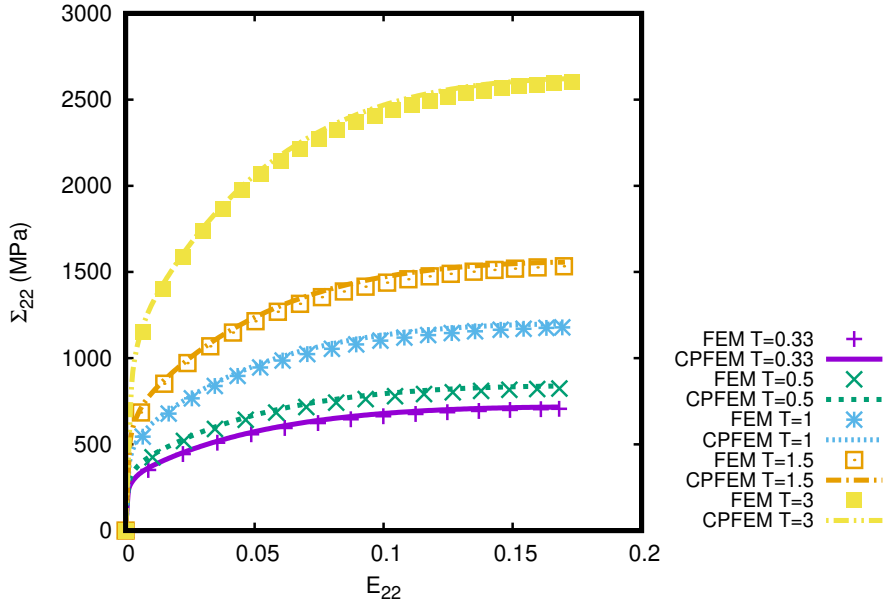

Figure 4.17: Comparison of axial stress strain responses for DP1 steel obtained from 0.33, 0.5, 1, 1.5 and 3 average triaxiality simulations.

presented previously in Figure 4.5(a) and Figure 4.11(a). Some small fluctuations are observed in CPFEM results due to the anisotropic nature of the crystal plasticity

model. However, applied boundary conditions give satisfactory results overall.

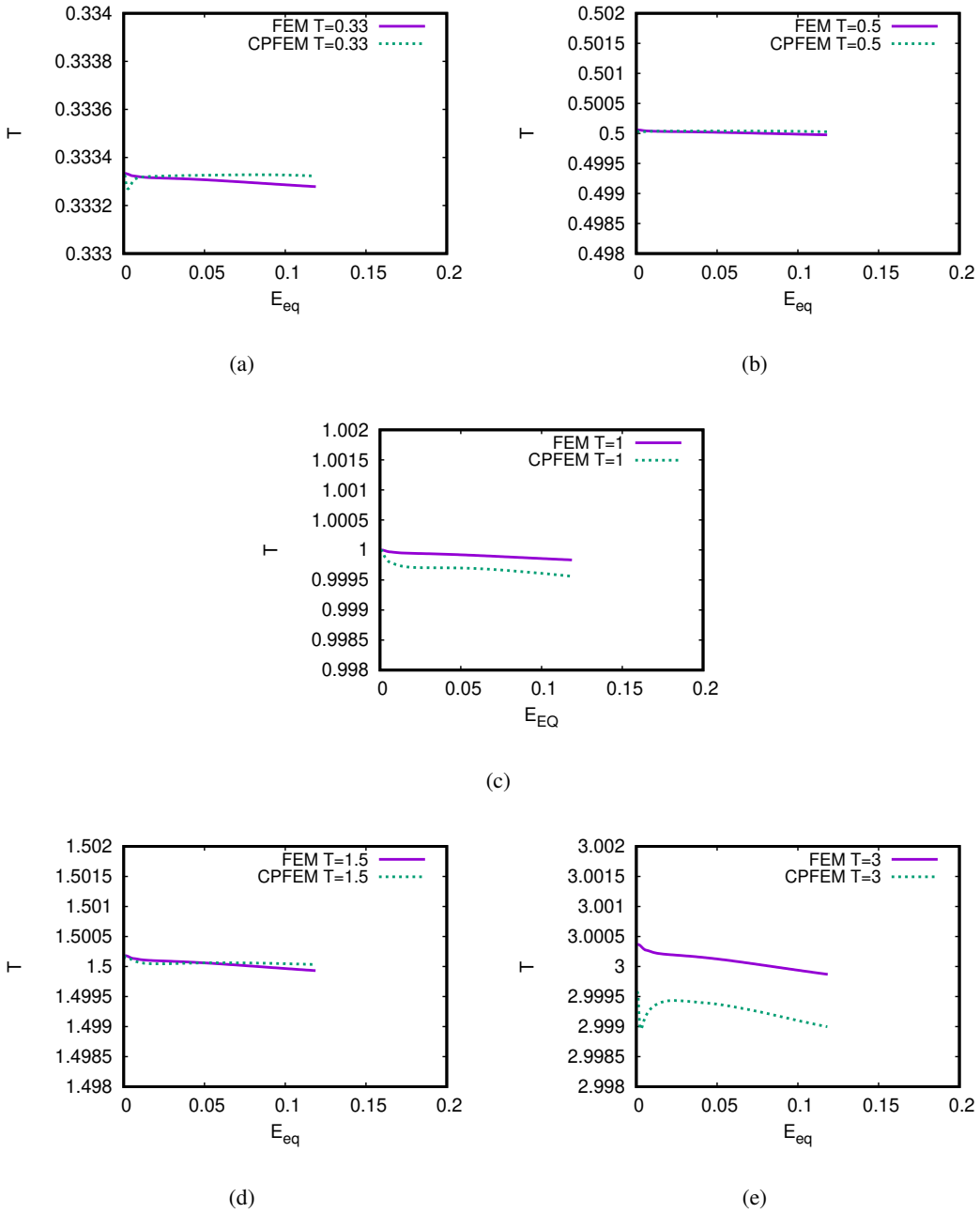

Figure 4.18: Comparison of triaxiality results for DP4 obtained from J2 and CPFEM simulations at 0.33 (a), 0.5 (b), 1 (c), 1.5 (d) and 3 (e).

The stress state evolution is analyzed here for DP1 and DP4 alloys for different triaxiality values. Pressure and logarithmic principle strain contour plots of both DP steels at mesoscopic strain level of E_{eq}=0.1 is compared in Figure 4.19 for DP1 and Figure

4.20 for DP4. For illustration purpose the martensite islands are removed from the microstructures since the void formation is observed in ferritic phase. Pressure distributions at different T are presented because negative internal pressure is actually equal to positive hydrostatic stress. As studied earlier under Section 3.3, the definition of stress triaxiality is the ratio of hydrostatic stress to von Mises equivalent stress. Positive hydrostatic stress indicates local high stress triaxiality and therefore possible void formation. Although overall T is kept constant through deformation, it is possible to observe the effect through locally different T values.

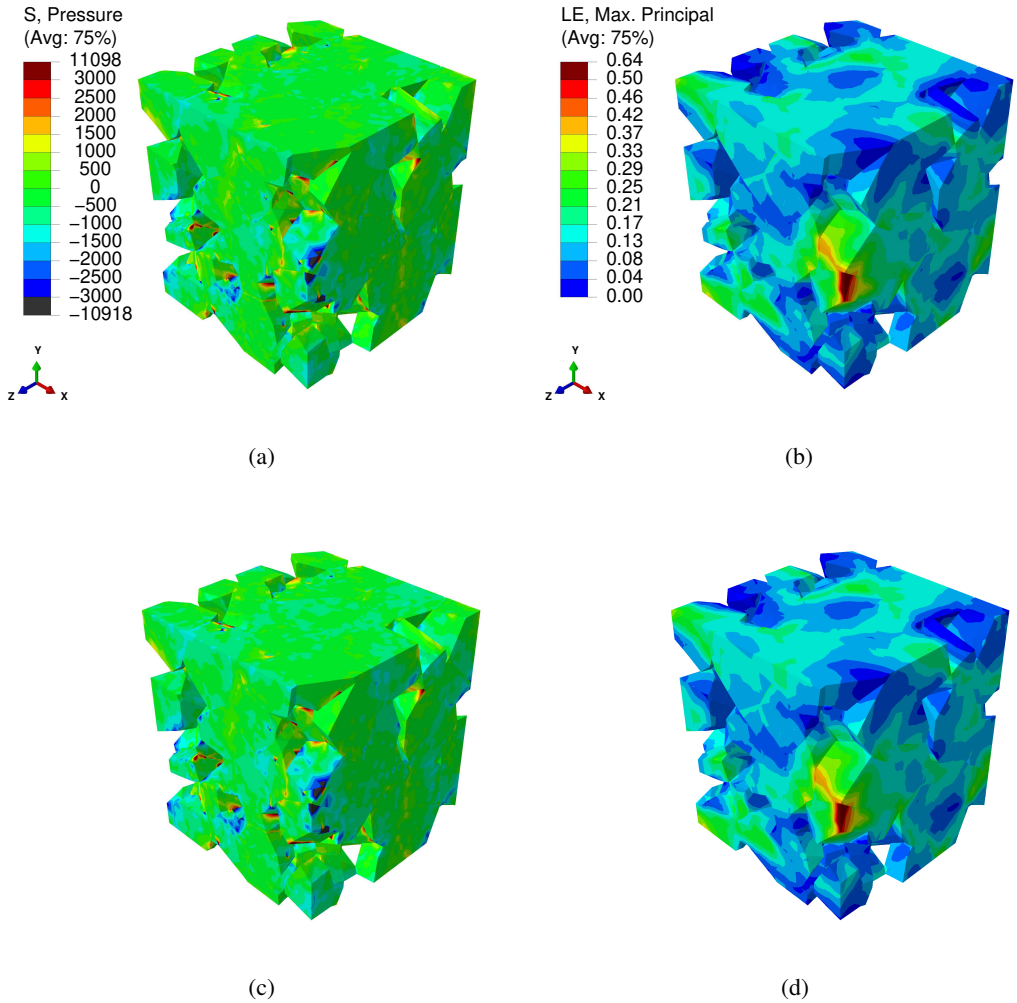

Figure 4.19: Pressure (a,c,e,g,i) and logarithmic principal strain (b,d,f,h,j) distributions of DP1 at mesoscopic E_{eq}=0.1 obtained for triaxiality values 0.33 (a-b), 0.5 (c-d), 1 (e-f), 1.5 (g-h) and 3 (i-j).

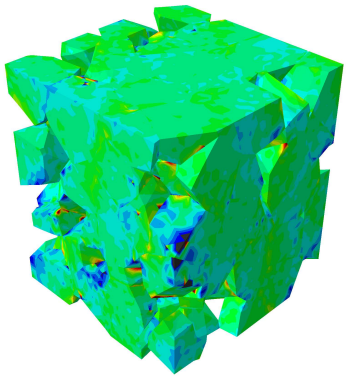

(e)

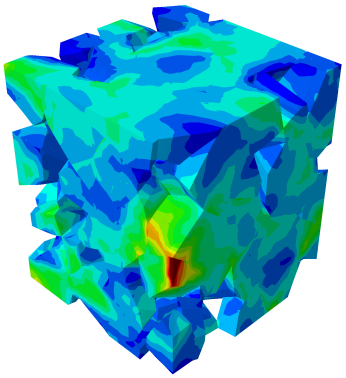

(f)

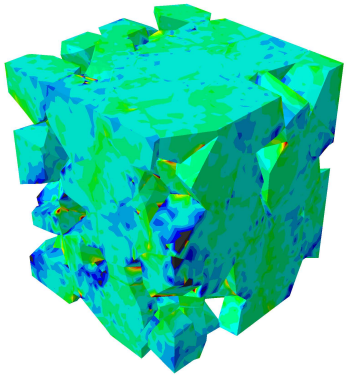

(g)

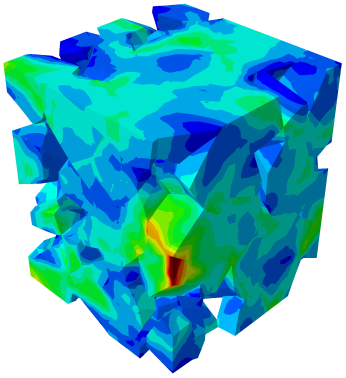

(h)

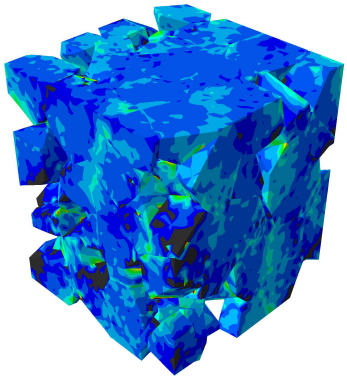

(i)

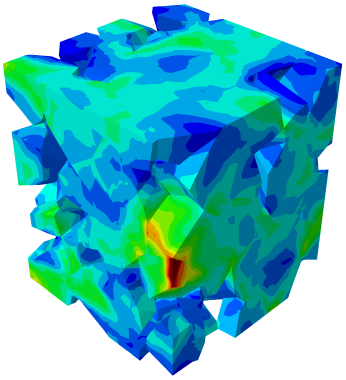

(j)

Figure 4.19: (continued)

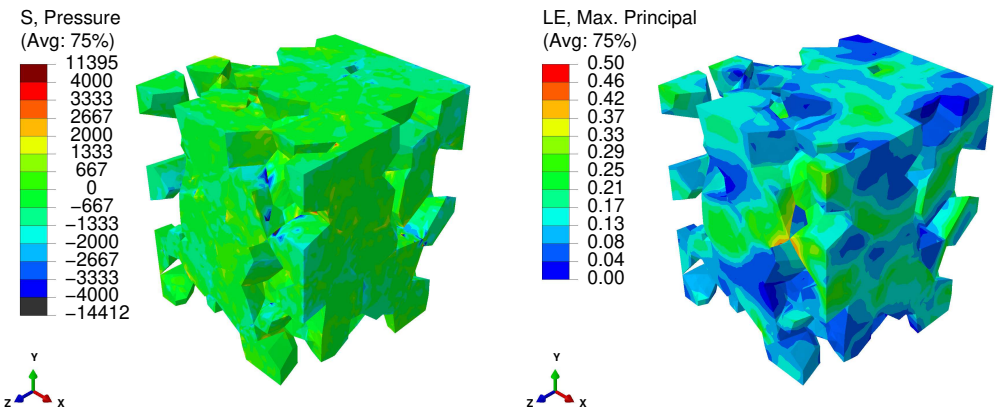

(a) (b)

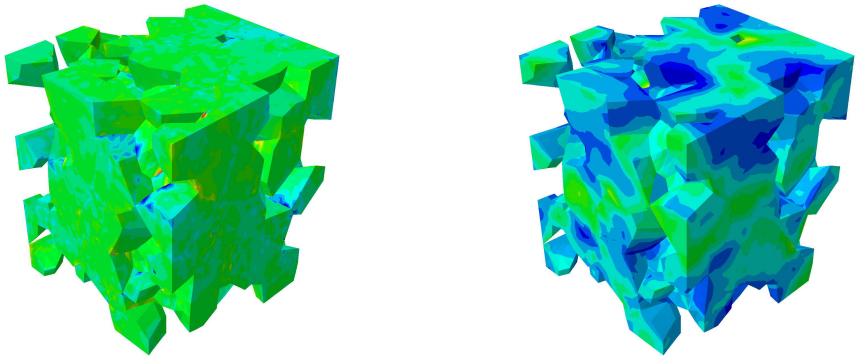

(c) (d)

Figure 4.20: Pressure (a,c,e,g,i) and logarithmic principal strain (b,d,f,h,j) distributions of DP4 at mesoscopic E_{eq}=0.1 obtained for triaxiality values 0.33 (a-b), 0.5 (c-d), 1 (e-f), 1.5 (g-h) and 3 (i-j).

Figure 4.19 shows contour plots that belong to DP1. Crystal plasticity grain orientations are kept same with the previous simulations. High negative pressure therefore high positive hydrostatic stress regions become observable first at ferrite-martensite grain boundaries and at locations where martensite has sharp ends. As the triaxiality increases negative pressure regions spread and also become observable along some ferrite-ferrite grain boundaries. Interestingly, strain localization do not show any prominent distinction. This shows that the orientation mismatch at grain boundaries might be the main driving force for the spatial strain evolution here. An appar-

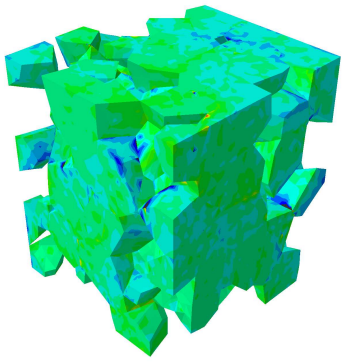

(e)

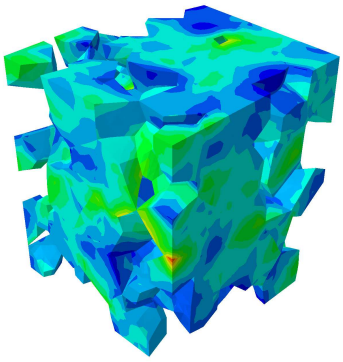

(f)

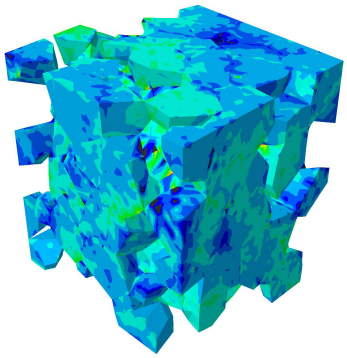

(g)

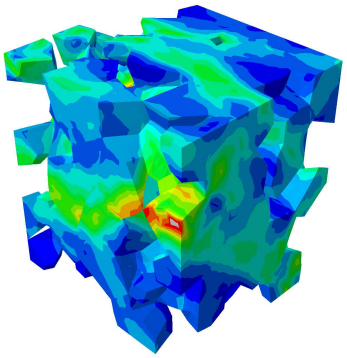

(h)

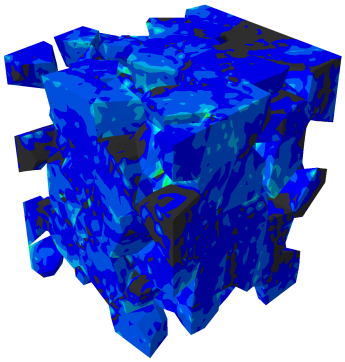

(i)

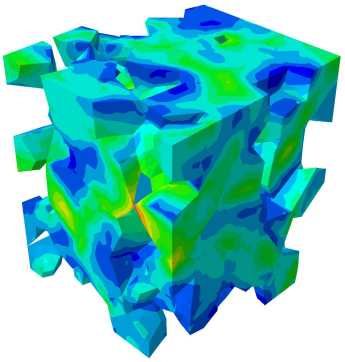

(j)

Figure 4.20: (continued)

ent strain localization (shown in red color) exists at a ferrite-ferrite grain boundary located in between two sharp ends of two different martensite islands, which happens to overlap with a high negative pressure region. Figure 4.20 shows contour plots that belong to DP4. Similar to DP1 contour plots, high negative pressure regions become observable initially on ferrite, at ferrite-martensite grain boundaries and at locations where martensite has sharp ends. High hydrostatic stresses are seen at the sharp ends of martensite due to the fact that martensite deforms less than ferrite. Strain localization locations are observed at different points mostly located at sharp ends of martensite grains or where two separate martensite sharp ends meet. Some localized strain regions overlap with negative internal pressure points. Although this is noticeable in most microstructures, it does not necessarily mean that strain localization regions possess high stress triaxiality. Both would lead separately to possible void initiation [16].

According to uniaxial tension studies conducted by Kadkhodapour et al., voids occur at long ferrite-ferrite grain boundaries in the direct neighbourhood of martensite islands. These voids initiate because of local stress accumulations caused by strain incompatibilities. They are found to propagate towards phase interfaces like a crack. Another type of void formation occurs at ferrite-martensite grain boundaries. This is observed when small martensite grains are closely packed with ferrite grains located in between. It is assumed that local high stress triaxiality causes this type of void formation [57]. As mentioned before, martensite keeps elastic as ferrite undergoes plastic deformation. Plastic deformation in ferrite is constrained by martensite islands located nearby. Martensite islands act as local barriers that constrain deformation of ferrite, inevitably causing build up of high triaxiality at grain boundaries [88]. Depending on the martensite dispersion inside ferrite matrix, level of constraint may differ [89]. Therefore different triaxiality values and void formation rates can be seen.

As presented in pressure distributions in Figure 4.19 and Figure 4.20, locally high hydrostatic stresses are observed initially at ferrite-martensite grain boundaries. High triaxiality regions propagate through ferrite-ferrite grain boundaries with increasing stress triaxiality. High stress and strain accumulation regions obtained here correlate well with experimental and simulated results reported in the literature (see e.g. [57],

[88]). errite-ferrite grain boundary void initiation is seen at higher T values of 1.5 and 3. Figures 4.19(i) and 4.20(i) show high hydrostatic pressure spread throughout the microstructure, indicating that this overall T=3 value is quite high and might be representing stress state of a specimen under severe deformation. This type of stress state may refer to the tip of a progressing crack. Starting from Figure 4.19(a) to (i) and Figure 4.20(a) to (i), as triaxiality increases, a dramatic increase in pressure, therefore void fraction is seen. At same strain levels, unusually high stresses accumulate throughout the microstructure with increasing T. When all microstructures in Figure 4.19 and 4.20 are compared, it is clear that the failure strain remarkably lowers as T value increases.

Section cuts from DP4 with different triaxiality values are plotted to investigate differences in pressure and strain evolutions. Figure 4.21 illustrate the comparison of pressure distribution. Ferrite in J2 plasticity solutions show less negative pressure distributions. Ferrite with crystal plasticity shows more spread high negative pressure. Occurrence of additional negative pressure regions are caused by randomly assigned orientations. Comparison of J2 and CPFEM logarithmic principal strain solutions are given in 4.22. Although the amount of strain show difference, interestingly, the strain localization regions that occur in J2 and crystal plasticity solutions are similar. It is believed that the axisymmetric loading affects the strain accumulations, while ferrite grain orientations affect the strain distribution in the previously discussed uniaxial tension case.

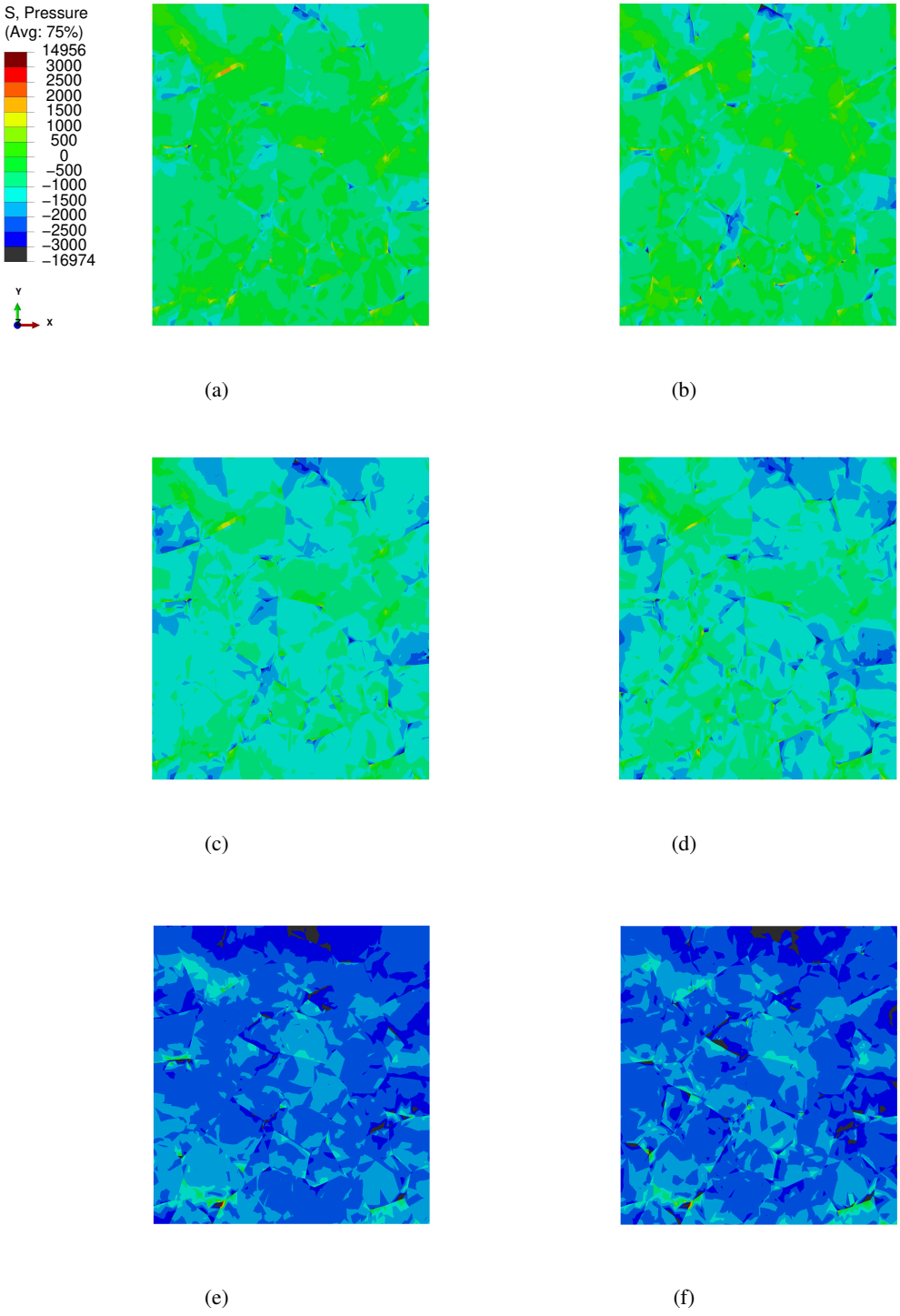

Figure 4.21: Comparison of pressure distribution for DP4 obtained from J2 (a,c,e) and CPFEM (b,d,f) at mesoscopic E_{eq}=0.1 for triaxiality values 0.5 (a-b), 1 (c-d) and 1.5 (e-f).

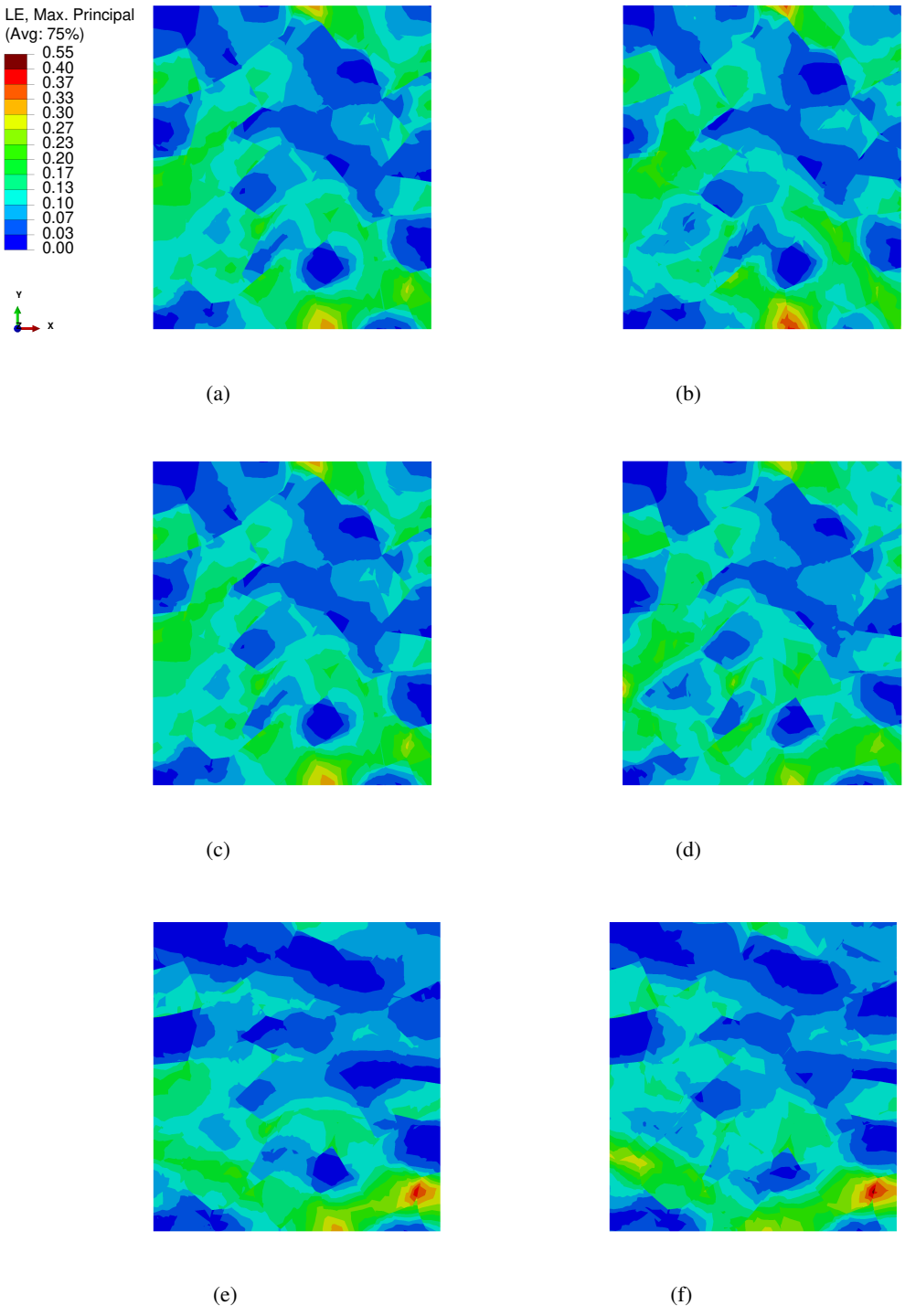

Figure 4.22: Comparison of equivalent logarithmic principal strain distribution for DP4 obtained from J2 (a,c,e) and CPFEM (b,d,f) at mesoscopic E_{eq}=0.1 for triaxiality values 0.5 (a-b), 1 (c-d) and 1.5 (e-f).

CHAPTER 5

SUMMARY, CONCLUSIONS AND OUTLOOK

A detailed micromechanical study on the plastic behaviour of dual phase steels is conducted in this thesis. These materials are composed of a ductile ferritic phase and a brittle martensitic phase and they have been favourable in automotive industry due to their satisfying strength and ductility properties. However their two phase microstructure makes them interesting from localization and failure points of view at micron scale. DP steels have been studied extensively in order to produce the optimum material with respect to strength and ductility. This work contributes to these studies in the context of micromechanical modelling focusing on the effect of triaxiality and microstructural aspects.

DP steel microstructural characteristics such as martensite volume fraction, martensite carbon content, ferrite grain size and martensite morphology are the main contributors to the overall behaviour and the key factors for designing an ideal dual-phase steel with better features. These microstructural traits are investigated at micro level by using RVEs which reflect the overall behaviour of the material at mesoscale. Different dual-phase steels having different martensite volume fractions of 15%, 19%, 28% and 37% (named as DP1, DP2, DP3 and DP4 respectively) are generated at micro scale by using Neper and classical J2 elastoplastic theory is assigned to each phase with the help of phenomenological flow equations. After the initial results, crystal plasticity is assigned to ferrite phase for a more detailed investigation. A parameter fitting procedure is carried initially for DP1 with 6.5 μm. This parameter set is used to model DP2, DP3 and DP4 which have different ferrite grain sizes. The obtained stress-strain response did not correlate well with experimental results presented in [18]. Therefore for each case new hardening parameters are identified for

each grain size and more accurate agreements are obtained.

The initial conclusion is that the stresses increase as martensite volume fraction V_m increases. Increased martensite volume fraction has a negative influence on the ductility. Steels with higher martensite volume fractions show higher stresses and higher number of localization regions compared to steels with lower martensite volume fractions at the same mesoscopic strain level. Also strain in martensite islands become observable at high V_m while little to no strain is seen at low V_m. Macroscopic response obtained from both models are quite close to each other.

It is observed that, even though the parameters of the both J2 and CP models are identified with respect to real experimental data for each phase separately, in the RVE calculations with a random microstructure and morphology crystal plasticity solutions slightly overestimates the final DP results. These results could be related to the fact that in CP simulations there is orientation mismatch between the grains which do not occur in J2 simulations. J2 is more advantageous for macroscopic observations which gives quick and good fit to experiments. However at the grain scale J2 plasticity is not able to give realistic results at all. It lacks capturing the relation between stress and microstructural traits. The heterogeneity between the ferrite grains is not captured through J2 at all. The differences between the two constitutive model in the evolution of deformation and stress of ferrite phase is reflected to the martensitic ones as well. Strain plots in this phase also show differences again due to random crystallographic orientations. More pronounced localizations exist in CPFEM solutions. It might be suggested that if grain scale effects are not in the scope, J2 plasticity theory should be preferred due to less computational cost.

At the final stage, localization and the initiation of ductile damage through void formation is studied focussing on the effect of stress triaxiality. J2 and crystal plasticity theories are assigned to previously generated microstructures and axial tension simulations are conducted by ABAQUS Riks algorithm where the stress triaxiality is kept constant throughout deformation. Models were subjected to different triaxiality states of 0.33, 0.5, 1, 1.5, 3 by proper imposition of boundary conditions and loading scenarios by considering the relationship between void formation and stress triaxiality. According to the results, possible void nucleation sites increase with increasing stress

triaxiality and high local stress triaxiality values are seen at sharp ends of martensite, ferrite-ferrite grain boundaries which are in the vicinity of sharp ended martensite islands and ferrite-martensite grain boundaries. These observations comply well with existing studies, where it is shown that ferrite goes into plastic region while martensite remains elastic. As martensite islands block the plastic deformation in ferrite, consequently high stress triaxiality values occur at phase grain boundaries, favouring ductile damage.

The outcome of the modelling and the simulation methodologies used in this thesis shows good agreement with the existing experimental results. Therefore, simulations may be preferred as an alternative way within the DP steel design and optimization process. Especially the RVE studies with realistic microstructures and physics based constitutive models would give important conclusions regarding the effect of microstructure on the overall constitutive response. In order to satisfy the demands of related industries, various different DP steel design processes may be analysed by using aforementioned approaches, providing time and cost efficient applications.

Main conclusions together with tips for future studies can be summarized as follows:

- Even though the RVEs are generated based on certain mechanical assumptions, the homogenized results show quite good fit with respect to experimental ones. Note that in these simulations only the parameters of pure ferrite and pure martensite flow curves are identified. The generated finite element models do not have any information about the real microstructure and phase morphology. This effect could be quite pronounced for the physics based simulations with crystal plasticity model. But the results are quite satisfactory with respect to experimental ones.

- In local crystal plasticity simulations, one has to identify the ferrite phase parameter for each different grain size case. It has been observed that with a single parameter set, which is identified with respect to biggest grain size, the RVE simulations do not give good correspondence for the other martensite volume fraction examples which include smaller ferrite size. Use of strain gradient crystal plasticity models, which are inherently size dependent, could give satisfactory results with one ferrite parameter set. The model for the martensite uses

always the phenomenological approach and it would not require any additional effort in these simulations.

- Even though the parameters of J2 and CPFEM simulations are fitted with respect to real experimental data, in RVE calculations, which includes a random morphology and orientation distributions, the crystal plasticity results show more hardening compared to J2 ones. This could be due to the orientation difference between different ferrite phase that result in stress concentrations at the grain boundaries. J2 simulations do not feel this phenomenon since there is no orientation information of the grains at all. This reality is reflected in the stress values observed in the martensite islands as well which are higher in CP simulations than the ones in J2 plasticity results.

- There are pronounced differences in the spatial evolution of both stress and strain between J2 and CP simulations. While J2 is cheaper and satisfactory for macroscopic conclusions, CP gives more realistic results at the micro scale, yet it is numerically more expensive. The users should choose the model based on the needs at micro and macro levels.

- As studied in the last section of the thesis, all types of boundaries (ferrite-ferrite, martensite-ferrite) play crucial role for the crack initiation in dual phase steels. For a more thorough study one has to incorporate cohesive zone elements at the grain boundaries and the parameters of the cohesive zone models should be identified based on the nature of the boundary. Such a study could give interesting conclusions regarding the failure of DP steels at this length scale. This is a necessity to obtain solid conclusions for failure initiation. Yet, the identification of cohesive parameters between different grain boundaries requires certain effort. The mismatch between the grain boundaries would automatically include certain physics for the evolution of traction thanks to crystal plasticity model.

REFERENCES

[1] N. Fonstein. Dual-phase steels. In R. Rana and S. Singh, editors, *Automotive Steels: Design, Metallurgy, Processing and Applications*, pages 169–216. Woodhead Publishing, 2017.

[2] C.C. Tasan, M. Diehl, D. Yan, M. Bechtold, F. Roters, L. Schemmann, C. Zheng, N. Peranio, D. Ponge, M. Koyama, K. Tsuzaki, and D. Raabe. An overview of dual-phase steels: Advances in microstructure-oriented processing and micromechanically guided design. *Annual Review of Materials Research*, 45(1):391–431, 2015.

[3] L. Madej, J. Wang, K. Perzynski, and P. D. Hodgson. Numerical modeling of dual phase microstructure behavior under deformation conditions on the basis of digital material representation. *Computational Materials Science*, 95:651–662, 2014.

[4] M. Mazinani and W. J. Poole. Effect of martensite plasticity on the deformation behavior of a low-carbon dual-phase steel. *Metallurgical and Materials Transactions A: Physical Metallurgy and Materials Science*, 38(2):328–339, 2007.

[5] Y. Granbom. *Structure and mechanical properties of dual phase steels – An experimental and theoretical analysis*. PhD thesis, School of Industrial Enginnering and Management - Division on Mechanical Metallurgy, Stockholm Sweden, 2010.

[6] J.H. Hollomon. Tensile deformation. *Transactions of the Metallurgical Society of AIME*, pages 268–290, 1945.

[7] P. Ludwik. *Elemente der Technologischen Mechanik*. Springer-Valag, 32 edition, 1909.

[8] H.W. Swift. Plastic instability under plane stress. *Journal of the Mechanics and Physics of Solids*, 1(1):1–18, 1952.

[9] E. Voce. The relationship between stress and strain for homogeneous deformation. *Journal of the Institute of Metals*, 74:537–562, 1948.

[10] C. C. Tasan, J. P. M. Hoefnagels, M. Diehl, D. Yan, F. Roters, and D. Raabe. Strain localization and damage in dual phase steels investigated by coupled in-situ deformation experiments and crystal plasticity simulations. *International Journal of Plasticity*, 63:198–210, 2014.

[11] A. Bag, K. K. Ray, and E. S. Dwarakadasa. Influence of martensite content and morphology on tensile and impact properties of high-martensite dual-phase steels. *Metallurgical and Materials Transactions A: Physical Metallurgy and Materials Science*, 30(5):1193–1202, May 1999.

[12] J. Kadkhodapour, S. Schmauder, D. Raabe, S. Ziaei-Rad, U. Weber, and M. Calcagnotto. Experimental and numerical study on geometrically necessary dislocations and non-homogeneous mechanical properties of the ferrite phase in dual phase steels. *Acta Materialia*, 59(11):4387–4394, 2011.

[13] S.-H. Choi, E.-Y. Kim, W. Woo, S.H. Han, and J.H. Kwak. The effect of crystallographic orientation on the micromechanical deformation and failure behaviors of dp980 steel during uniaxial tension. *International Journal of Plasticity*, 45:85 – 102, 2013.

[14] M. Jafari, S. Ziaei-rad, N. Saeidi, and M. Jamshidian. Micromechanical analysis of martensite distribution on strain localization in dual phase steels by scanning electron microscopy and crystal plasticity simulation. *Materials Science & Engineering A*, 670:57–67, 2016.

[15] X. Sun, K. S. Choi, W. N. Liu, and M. A. Khaleel. Predicting failure modes and ductility of dual phase steels using plastic strain localization. *International Journal of Plasticity*, 25(10):1888–1909, 2009.

[16] J. Kadkhodapour, A. Butz, S. Ziaei-Rad, and S. Schmauder. A micro mechanical study on failure initiation of dual phase steels under tension using single crystal plasticity model. *International Journal of Plasticity*, 27(7):1103–1125, 2011.

[17] E. Ahmad, T. Manzoor, K. L. Ali, and J. I. Akhter. Effect of microvoid formation on the tensile properties of dual-phase steel. *Journal of Materials Engineering and Performance*, 9(3):306–310, 2000.

[18] Q. Lai, L. Brassart, O. Bouaziz, M. Gouné, M. Verdier, G. Parry, A. Perlade, Y. Bréchet, and T. Pardoen. Influence of martensite volume fraction and hardness on the plastic behavior of dual-phase steels: Experiments and micromechanical modeling. *International Journal of Plasticity*, 80:187–203, 2016.

[19] A. P. Pierman, O. Bouaziz, T. Pardoen, P. J. Jacques, and L. Brassart. The influence of microstructure and composition on the plastic behaviour of dual-phase steels. *Acta Materialia*, 73:298–311, 2014.

[20] L. F. Ramos, D. K. Matlock, and G. Krauss. On the deformation behavior of dual-phase steels. *Metallurgical Transactions A*, 10(2):259–261, Feb 1979.

[21] V. Uthaisangsuk, S. Muenstermann, U. Prahl, W. Bleck, H. P. Schmitz, and T. Pretorius. A study of microcrack formation in multiphase steel using representative volume element and damage mechanics. *Computational Materials Science*, 50(4):1225–1232, 2011.

[22] S. Sodjit and V. Uthaisangsuk. Microstructure based prediction of strain hardening behavior of dual phase steels. *Materials and Design*, 41:370–379, 2012.

[23] M. Erdogan and R. Priestner. Effect of martensite content, its dispersion, and epitaxial ferrite content on bauschinger behaviour of dual phase steel. *Materials Science and Technology*, 18(4):369–376, 2002.

[24] Chang Peng-Heng and A.G. Preban. The effect of ferrite grain size and martensite volume fraction on the tensile properties of dual phase steel. *Acta Metallurgica*, 33(5):897 – 903, 1985.

[25] Z. Jiang, Z. Guan, and J. Lian. Effects of microstructural variables on the deformation behaviour of dual-phase steel. *Materials Science & Engineering A*, 190(1):55–64, 1995.

[26] Q. Lai, O. Bouaziz, M. Gouné, L. Brassart, M. Verdier, G. Parry, A. Perlade, Y. Bréchet, and T. Pardoen. Damage and fracture of dual-phase steels : In

fl uence of martensite volume fraction. *Materials Science & Engineering A*, 646:322–331, 2015.

[27] M. Erdogan. The effect of new ferrite content on the tensile fracture behaviour of dual phase steels. *Journal of Materials Science*, 37(17):3623–3630, 2002.

[28] M. Sarwar and R. Priestner. Influence of ferrite-martensite microstructural morphology on tensile properties of dual-phase steel. *Journal of Materials Science*, 31(8):2091–2095, Jan 1996.

[29] G. Cheng, K.S. Choi, X. Hu, and X. Sun. Determining individual phase properties in a multi-phase qp steel using multi-scale indentation tests. *Materials Science & Engineering A*, 652:384 – 395, 2016.

[30] A. Ramazani, A. Schwedt, A. Aretz, and U. Prahl. Failure Initiation in Dual-Phase Steel. *Key Engineering Materials*, 586:67–71, 2013.

[31] V. Colla, M. De Sanctis, A. Dimatteo, G. Lovicu, A. Solina, and R. Valentini. Strain hardening behavior of dual-phase steels. *Metallurgical and Materials Transactions A: Physical Metallurgy and Materials Science*, 40(11):2557–2567, 2009.

[32] A. Ramazani, M. Abbasi, S. Kazemiabnavi, S. Schmauder, R. Larson, and U. Prahl. Development and application of a microstructure-based approach to characterize and model failure initiation in DP steels using XFEM. *Materials Science & Engineering A*, 660:181–194, 2016.

[33] M. Luo and T. Wierzbicki. Numerical failure analysis of a stretch-bending test on dual-phase steel sheets using a phenomenological fracture model. *International Journal of Solids and Structures*, 47(22-23):3084–3102, 2010.

[34] S. Qin, R. McLendon, V. Oancea, and A. M. Beese. Micromechanics of multiaxial plasticity of DP600: Experiments and microstructural deformation modeling. *Materials Science & Engineering A*, 721(February):168–178, 2018.

[35] R.-M. Rodriguez and I. Gutiérrez. Unified formulation to predict the tensile curves of steels with different microstructures. *Materials Science Forum*, 426:4525–4530, 01 2003.

[36] V. Uthaisangsuk, U. Prahl, and W. Bleck. Stretch-flangeability characterisation of multiphase steel using a microstructure based failure modelling. *Computational Materials Science*, 45(3):617–623, 2009.

[37] T. Sirinakorn, S. Wongwises, and V. Uthaisangsuk. A study of local deformation and damage of dual phase steel. *Materials and Design*, 64:729–742, 2014.

[38] M. Amirmaleki, J. Samei, D. E. Green, I. van Riemsdijk, and L. Stewart. 3D micromechanical modeling of dual phase steels using the representative volume element method. *Mechanics of Materials*, 101:27–39, 2016.

[39] H. Hosseini-Toudeshky, B. Anbarlooie, and J. Kadkhodapour. Micromechanics stress-strain behavior prediction of dual phase steel considering plasticity and grain boundaries debonding. *Materials and Design*, 68:167–176, 2015.

[40] V. Uthaisangsuk, U. Prahl, and W. Bleck. Modelling of damage and failure in multiphase high strength DP and TRIP steels. *Engineering Fracture Mechanics*, 78(3):469–486, 2011.

[41] N Vajragupta, V Uthaisangsuk, B Schmaling, S Münstermann, A Hartmaier, and W Bleck. A micromechanical damage simulation of dual phase steels using XFEM. *Computational Materials Science*, 54(1):271–279, 2012.

[42] T. W. J. de Geus, F. Maresca, R. H. J. Peerlings, and M. G. D. Geers. Microscopic plasticity and damage in two-phase steels: On the competing role of crystallography and phase contrast. *Mechanics of Materials*, 101:147–159, 2016.

[43] C. W. Du. *Micro-plasticity characterization of martensite, ferrite, and dual-phase steel*. PhD thesis, Technische Universiteit Eindhoven - Department of Mechanical Engineering, 2016.

[44] S. Mahmoody. *Micromechanical modelling of dual-phase steel using a rate-dependent crystal plasticity model*. PhD thesis, McGill University - Department of Mechanical Engineering, 2007.

[45] C. Pu and Y. Gao. Crystal plasticity analysis of stress partitioning mechanisms and their microstructural dependence in advanced steels. *Journal of Applied Mechanics*, 82, 03 2015.

[46] W. Woo, V. T. Em, E. Kim, S. H. Han, Y. S. Han, and S. Choi. Stress–strain relationship between ferrite and martensite in a dual-phase steel studied by in situ neutron diffraction and crystal plasticity theories. *Acta Materialia*, 60(20):6972–6981, 2012.

[47] R. J. Asaro. Micromechanics of crystals and polycrystals. volume 23 of *Advances in Applied Mechanics*, pages 1–115. Elsevier, 1983.

[48] R. Hill and J.R. Rice. Constitutive analysis of elastic-plastic crystals at arbitrary strain. *Journal of the Mechanics and Physics of Solids*, 20(6):401 – 413, 1972.

[49] S. R. Kalidindi, C. A. Bronkhorst, and L. Anand. Crystallographic texture evolution in bulk deformation processing of FCC metals. *Journal of the Mechanics and Physics of Solids*, 40(3):537–569, 1992.

[50] R. J. Asaro and A. Needleman. Texture development and strain hardening in rate dependent polycrystals. *Acta Metallurgica*, 33(6):923–953, 1985.

[51] Y. Huang. A user-material subroutine incorporating single crystal plasticity in the abaqus finite element program. Technical report, Harvard University - Division of Engineering and Applied Sciences, 1991.

[52] T. Yalcinkaya, W. A. M. Brekelmans, and M. G. D. Geers. BCC single crystal plasticity modeling and its experimental identification. *Modelling and Simulation in Materials Science and Engineering*, 16(8):085007, 2008.

[53] A. Ramazani, A. Schwedt, A. Aretz, U. Prahl, and W. Bleck. Characterization and modelling of failure initiation in DP steel. *Computational Materials Science*, 75:35–44, 2013.

[54] N. H. Abid, R. K. Abu Al-Rub, and A. N. Palazotto. Computational modeling of the effect of equiaxed heterogeneous microstructures on strength and ductility of dual phase steels. *Computational Materials Science*, 103:20–37, 2015.

[55] R. Quey, P. R. Dawson, and F. Barbe. Large-scale 3D random polycrystals for the finite element method: Generation, meshing and remeshing. *Computer Methods in Applied Mechanics and Engineering*, 200(17-20):1729–1745, 2011.

[56] Dassault Systèmes Simulia. Abaqus 6.12. *Analysis User's Guide, Dassault Systems*, 2012.

[57] J. Kadkhodapour, A. Butz, and S. Ziaei Rad. Mechanisms of void formation during tensile testing in a commercial, dual-phase steel. *Acta Materialia*, 59(7):2575–2588, 2011.

[58] J. H. Kim, M. G. Lee, J. H. Kang, C. S. Oh, and F. Barlat. Crystal plasticity finite element analysis of ferritic stainless steel for sheet formability prediction. *International Journal of Plasticity*, 93:26–45, 2017.

[59] H. F. Al-Harbi. *Crystal plasticity finite element simulations using discrete Fourier transforms*. PhD thesis, Georgia Institute of Technology - George W. Woodruff School of Mechanical Engineering, 2014.

[60] T. Yalcinkaya, W. A. M. Brekelmans, and M. Geers. A composite dislocation cell model to describe strain path change effects in bcc metals. *Modelling and Simulation in Materials Science and Engineering*, 17:064008, 08 2009.

[61] C. Du, F. Maresca, M.G.D. Geers, and J.P.M. Hoefnagels. Ferrite slip system activation investigated by uniaxial micro-tensile tests and simulations. *Acta Materialia*, 146:314–327, 3 2018.

[62] F. A. McClintock. A Criterion for Ductile Fracture by the Growth of Holes. *Journal of Applied Mechanics*, 35(2):363–371, 1968.

[63] T. Pardoen and J.W. Hutchinson. An extended model for void growth and coalescence. *Journal of the Mechanics and Physics of Solids*, 48:2467–2512, 12 2000.

[64] V. Tvergaard. On localization in ductile materials containing spherical voids. *International Journal of Fracture*, 18(4):237 – 252, 1982.

[65] V. Tvergaard. Material failure by void growth to coalescence. volume 27 of *Advances in Applied Mechanics*, pages 83 – 151. Elsevier, 1989.

[66] E. Maire, O. Bouaziz, M. Di Michiel, and C. Verdu. Initiation and growth of damage in a dual-phase steel observed by X-ray microtomography. *Acta Materialia*, 56(18):4954–4964, 2008.

[67] G. Requena, E. Maire, C. Leguen, and S. Thuillier. Separation of nucleation and growth of voids during tensile deformation of a dual phase steel using synchrotron microtomography. *Materials Science & Engineering A*, 589:242–251, 2014.

[68] N. Saeidi, F. Ashrafizadeh, B. Niroumand, M.R. Forouzan, and F. Barlat. Damage mechanism and modeling of void nucleation process in a ferrite–martensite dual phase steel. *Engineering Fracture Mechanics*, 127:97 – 103, 2014.

[69] A. L. Gurson. Continuum Theory of Ductile Rupture by Void Nucleation and Growth: Part I—Yield Criteria and Flow Rules for Porous Ductile Media. *Journal of Engineering Materials and Technology*, 99(1):2, 1977.

[70] J. R. Rice and D. M. Tracey. On the ductile enlargement of voids in triaxial stress fields. *Journal of the Mechanics and Physics of Solids*, 17(3):201–217, 1969.

[71] J.C. Lautridou and A. Pineau. Crack initiation and stable crack growth resistance in a508 steels in relation to inclusion distribution. *Engineering Fracture Mechanics*, 15(1):55 – 71, 1981.

[72] D. Anderson, S. Winkler, A. Bardelcik, and M.J. Worswick. Influence of stress triaxiality and strain rate on the failure behavior of a dual-phase dp780 steel. *Materials & Design*, 60:198 – 207, 2014.

[73] Y. Bao and T. Wierzbicki. On fracture locus in the equivalent strain and stress triaxiality space. *International Journal of Mechanical Sciences*, 46(1):81–98, 2004.

[74] R. C. Lin, D. Steglich, W. Brocks, and J. Betten. Performing RVE calculations under constant stress triaxiality for monotonous and cyclic loading. *International Journal for Numerical Methods in Engineering*, 66(8):1331–1360, 2006.

[75] V. Kouznetsova, W. A. M. Brekelmans, and F. P. T. Baaijens. Approach to micro-macro modeling of heterogeneous materials. *Computational Mechanics*, 27(1):37–48, Jan 2001.

[76] C. Tekoglu. Representative volume element calculations under constant stress triaxiality, Lode parameter, and shear ratio. *International Journal of Solids and Structures*, 51(25-26):4544–4553, 2014.

[77] W. Brocks, D. Z. Sun, and A. Hönig. Verification of the transferability of micromechanical parameters by cell model calculations with visco-plastic materials. *International Journal of Plasticity*, 11(8):971–989, 1995.

[78] D. Steglich and W. Brocks. Micromechanical modelling of the behaviour of ductile materials including particles. *Computational Materials Science*, 9(1):7 – 17, 1997.

[79] H. Ghassemi-Armaki, R. Maaß, S. Bhat, S. Sriram, J.R. Greer, and K. Kumar. Deformation response of ferrite and martensite in a dual-phase steel. *Acta Materialia*, 62:197–211, 01 2014.

[80] S. K. Paul. Micromechanics based modeling of Dual Phase steels: Prediction of ductility and failure modes. *Computational Materials Science*, 56:34–42, 2012.

[81] R. K. Abu Al-Rub, M. Ettehad, and A. N. Palazotto. Microstructural modeling of dual phase steel using a higher-order gradient plasticity-damage model. *International Journal of Solids and Structures*, 58:178–189, 2015.

[82] H. Ghadbeigi, C. Pinna, and S. Celotto. Failure mechanisms in DP600 steel: Initiation, evolution and fracture. *Materials Science & Engineering A*, 588:420–431, 2013.

[83] Yalcinkaya T. Strain gradient crystal plasticity: Thermodynamics and implementation. In George Z. Voyiadjis, editor, *Handbook of Nonlocal Continuum Mechanics for Materials and Structures*, pages 1–32. Springer International Publishing, Cham, 2017.

[84] T. Yalcinkaya, W.A.M. Brekelmans, and M.G.D. Geers. Deformation patterning driven by rate dependent non-convex strain gradient plasticity. *Journal of the Mechanics and Physics of Solids*, 59(1):1 – 17, 2011.

[85] T. Yalcinkaya, W.A.M. Brekelmans, and M.G.D. Geers. Non-convex rate dependent strain gradient crystal plasticity and deformation patterning. *International Journal of Solids and Structures*, 49(18):2625 – 2636, 2012.

[86] Y. Bao. Dependence of ductile crack formation in tensile tests on stress triaxiality, stress and strain ratios. *Engineering Fracture Mechanics*, 72(4):505 – 522, 2005.

[87] L. Siad, M. Ould Ouali, and A. Benabbes. Comparison of explicit and implicit finite element simulations of void growth and coalescence in porous ductile materials. *Materials and Design*, 29(2):319–329, 2008.

[88] M. R. Ayatollahi, A. Ch. Darabi, H. R. Chamani, and J. Kadkhodapour. 3D Micromechanical Modeling of Failure and Damage Evolution in Dual Phase Steel Based on a Real 2D Microstructure. *Acta Mechanica Solida Sinica*, 29(1):95–110, 2016.

[89] S. K. Paul. Effect of martensite volume fraction on stress triaxiality and deformation behavior of dual phase steel. *Materials and Design*, 50:782–789, 2013.

APPENDIX A

EK A

A.1 Matlab script for grouping surface elements according to their faces

```
fname='inputFile.inp';
fid=fopen(fname,'rt');
S=textscan(fid, '%s', 'Delimiter', '\n');
S=S{1};

%find start of nodes
idxS=strfind(S,'Node');
idx1=find(not(cellfun('isempty',idxS)));

%find start of elements(elements start when nodes end)
idxS=strfind(S,'Element');
idx2=find(not(cellfun('isempty',idxS)));

%end of elements
idxS = strfind(S, '*Elset');
idx3 = find(not(cellfun('isempty', idxS)));

%store the node number and its coordinates
nodes=S(idx1+1:idx2-1);
nodes=cell2mat(cellfun(@str2num,nodes,'UniformOutput',false));

%store elements and its corresponding nodes
```

```
elements = S(idx2+1:idx3(1)-1) ;
ele = cell(length(elements),1) ;

for i = 1:length(elements)
      ele{i,1} = [elements{i}];
end

ele = cell2mat(cellfun(@str2num,ele,'UniformOutput',false));
ele = ele(:,1:5);

%group nodes as face nodes, edge nodes and vertice nodes
%1=node number, 2=x-cord, 3=y-cord, 4=z-cord

for i = 1:length(nodes)
%% find surface nodes
%% X1 AND X0
    if (nodes(i,2)==0)
        X0(i)=nodes(i,1);
        X0(X0==0)=[];
    end

    if (nodes(i,2)==1)
        X1(i)=nodes(i,1);
        X1(X1==0)=[];
    end
%% Y1 AND Y0
    if (nodes(i,3)==0)
        Y0(i)=nodes(i,1);
        Y0(Y0==0)=[];
    end

    if (nodes(i,3)==1)
        Y1(i)=nodes(i,1);
```

```
        Y1(Y1==0)=[];
    end
%% Z1 AND Z0
    if (nodes(i,4)==0)
        Z0(i)=nodes(i,1);
        Z0(Z0==0)=[];
    end

    if (nodes(i,4)==1)
        Z1(i)=nodes(i,1);
        Z1(Z1==0)=[];
    end
end

%% find elements at X0 and X1 surfaces
%X0
[lia,locb]=ismember(ele(:,2:5),X0(:));

for i=1:length(lia)
    %face 1
    if lia(i,1)==1 && lia(i,2)==1 && lia(i,3)==1
        X0_P1(i)=i;
        X0_P1(X0_P1==0)=[];
    end
    %face 2
    if lia(i,1)==1 && lia(i,2)==1 && lia(i,4)==1
        X0_P2(i)=i;
        X0_P2(X0_P2==0)=[];
    end
    %face 3
    if lia(i,2)==1 && lia(i,3)==1 && lia(i,4)==1
        X0_P3(i)=i;
        X0_P3(X0_P3==0)=[];
```

```
    end
    %face 4
    if lia(i,1)==1 && lia(i,3)==1 && lia(i,4)==1
        X0_P4(i)=i;
        X0_P4(X0_P4==0)=[];
    end
end
%%
%X1
[lia,locb]=ismember(ele(:,2:5),X1(:));

for i=1:length(lia)
    %face 1
    if lia(i,1)==1 && lia(i,2)==1 && lia(i,3)==1
        X1_P1(i)=i;
        X1_P1(X1_P1==0)=[];
    end
    %face 2
    if lia(i,1)==1 && lia(i,2)==1 && lia(i,4)==1
        X1_P2(i)=i;
        X1_P2(X1_P2==0)=[];
    end
    %face 3
    if lia(i,2)==1 && lia(i,3)==1 && lia(i,4)==1
        X1_P3(i)=i;
        X1_P3(X1_P3==0)=[];
    end
    %face 4
    if lia(i,1)==1 && lia(i,3)==1 && lia(i,4)==1
        X1_P4(i)=i;
        X1_P4(X1_P4==0)=[];
    end
end
```

```
%% find elements at Y1 surface
%Y1
[lia,locb]=ismember(ele(:,2:5),Y1(:));

for i=1:length(lia)
    %face 1
    if lia(i,1)==1 && lia(i,2)==1 && lia(i,3)==1
        Y1_P1(i)=i;
        Y1_P1(Y1_P1==0)=[];
    end
    %face 2
    if lia(i,1)==1 && lia(i,2)==1 && lia(i,4)==1
        Y1_P2(i)=i;
        Y1_P2(Y1_P2==0)=[];
    end
    %face 3
    if lia(i,2)==1 && lia(i,3)==1 && lia(i,4)==1
        Y1_P3(i)=i;
        Y1_P3(Y1_P3==0)=[];
    end
    %face 4
    if lia(i,1)==1 && lia(i,3)==1 && lia(i,4)==1
        Y1_P4(i)=i;
        Y1_P4(Y1_P4==0)=[];
    end
end

%% find elements at Z0 and Z1 surfaces
%Z0
[lia,locb]=ismember(ele(:,2:5),Z0(:));

for i=1:length(lia)
    %face 1
```

```
    if lia(i,1)==1 && lia(i,2)==1 && lia(i,3)==1
        Z0_P1(i)=i;
        Z0_P1(Z0_P1==0)=[];
    end
    %face 2
    if lia(i,1)==1 && lia(i,2)==1 && lia(i,4)==1
        Z0_P2(i)=i;
        Z0_P2(Z0_P2==0)=[];
    end
    %face 3
    if lia(i,2)==1 && lia(i,3)==1 && lia(i,4)==1
        Z0_P3(i)=i;
        Z0_P3(Z0_P3==0)=[];
    end
    %face 4
    if lia(i,1)==1 && lia(i,3)==1 && lia(i,4)==1
        Z0_P4(i)=i;
        Z0_P4(Z0_P4==0)=[];
    end
end
%%
%Z1
[lia,locb]=ismember(ele(:,2:5),Z1(:));

for i=1:length(lia)
    %face 1
    if lia(i,1)==1 && lia(i,2)==1 && lia(i,3)==1
        Z1_P1(i)=i;
        Z1_P1(Z1_P1==0)=[];
    end
    %face 2
    if lia(i,1)==1 && lia(i,2)==1 && lia(i,4)==1
        Z1_P2(i)=i;
```

```
        Z1_P2(Z1_P2==0)=[];
    end
    %face 3
    if lia(i,2)==1 && lia(i,3)==1 && lia(i,4)==1
        Z1_P3(i)=i;
        Z1_P3(Z1_P3==0)=[];
    end
    %face 4
    if lia(i,1)==1 && lia(i,3)==1 && lia(i,4)==1
        Z1_P4(i)=i;
        Z1_P4(Z1_P4==0)=[];
    end
end

%% RESHAPE VECTORS FOR ABAQUS INPUT FILE FORMAT AND PRINT
.
.
.
```

APPENDIX B

EK B

B.1 Python script for homogenization

```
#THIS SCRIPT CALCULATES STRESSES, STRAINS AND
#TRIAXIALITY FROM AN ABAQUS .ODB
#WRITES TO A .TXT FILE

from odbAccess import *
import odbAccess
from abaqusConstants import *
import sys
import operator
import numpy as np
import math
from timeit import default_timer as timer

#GET ODB NAME FROM USER
dir = raw_input("TYPE .ODB NAME WITHOUT EXTENSION: ")
type(dir)

#TIC
START = timer()

#OPEN .ODB
odb = openOdb(path = dir + '.odb')
```

```
#GET NAME OF THE ASSEMBLY, RETRIEVE AND RENAME THE
#MASTER NODE SET
myAssembly = odb.rootAssembly
ins=odb.rootAssembly.instances['TESS-1']
master = ins.nodeSets['MASTER']

#OPEN THE FILE TO WRITE OUTPUT DATA
Filename = dir+'.txt'
fout = open(Filename,'w')
fout.write('#S11(1) S22(2) S33(3) S12(4) S13(5) S23(6) Seq(7)
            Smean(8) T(9) E11(10) E22(11) E33(12) Eeq(13)')
fout.write('\n')
keys = odb.steps.keys()

for stp in keys: #LOOP OVER STEPS
    step = odb.steps[stp]
    frameRepository = step.frames
    numFrames = len(frameRepository)

    #LOOP OVER FRAMES
    for fr in range(0, numFrames):
        STRESS=[0,0,0,0,0,0]
        frame = step.frames[fr]

        #CALL STRESS AND IVOL DATA FOR EVERY ELEMENT
        #AND INTEGRATION POINT
        S = frame.fieldOutputs['S'].getSubset(region=ins,
                        position=INTEGRATION_POINT,
                        elementType='C3D10')

        IVOL = frame.fieldOutputs['IVOL'].getSubset(region=ins,
                        position=INTEGRATION_POINT,
```

```
                elementType='C3D10')

#CALL DISPLACEMENTS AT THE MASTER NODE
DISP = frame.fieldOutputs['U'].getSubset(region=master)

#ARRANGEMENT FOR STRESS, IVOL AND DISP VALUES
sValues = S.values
iValues = IVOL.values
dValues = DISP.values[0]

#GET DISPLACEMENTS OF THE MASTER NODE AT X, Y, Z
U1 = dValues.data[0]
U2 = dValues.data[1]
U3 = dValues.data[2]

#CALCULATE THE LENGTH AT X(L_1), Y(L_2), Z(L_3)
#1 IS THE INITIAL LENGTH OF EACH SIDE
L_1 = U1 + 1
L_2 = U2 + 1
L_3 = U3 + 1

#CALCULATE THE VOLUME OF THE RVE
VOL = L_1*L_2*L_3

#LOOP OVER INTEGRATION POINTS
for i in range(0,len(sValues)):
    STRESS[0] = STRESS[0] +
                ((sValues[i].data[0])*(iValues[i].data))
    STRESS[1] = STRESS[1] +
                ((sValues[i].data[1])*(iValues[i].data))
    STRESS[2] = STRESS[2] +
                ((sValues[i].data[2])*(iValues[i].data))
    STRESS[3] = STRESS[3] +
```

```
                ((sValues[i].data[3])*(iValues[i].data))
    STRESS[4] = STRESS[4] +
                ((sValues[i].data[4])*(iValues[i].data))
    STRESS[5] = STRESS[5] +
                ((sValues[i].data[5])*(iValues[i].data))
np.seterr(divide='ignore', invalid='ignore')
STRESS=(STRESS/VOL)

#HYDROSTATIC STRESS CALCULATION
sig_h = (STRESS[0] + STRESS[1] + STRESS[2])/3

#EQUIVALENT VON MISES STRESS CALCULATION
s1 = (STRESS[0]-STRESS[1])**2
s2 = (STRESS[1]-STRESS[2])**2
s3 = (STRESS[2]-STRESS[0])**2
t = (STRESS[3]**2 + STRESS[4]**2 + STRESS[5]**2)
sig_von = ((s1+s2+s3+6*t)/2)**(0.5)

#TRIAXIALITY CALCULATION
T = (sig_h/sig_von)

#LOGARITHMIC STRAINS E11, E22 AND E33 CALCULATION
E11 = 2*np.log(L_1/1)
E22 = np.log(L_2/1)
E33 = 2*np.log(L_3/1)

#EQUIVALENT VON MISES STRAIN CALCULATION
e1 = (E11-E22)**2
e2 = (E22-E33)**2
e3 = (E33-E11)**2
Eeq= (((e1 + e2 + e3)/2)**(0.5))*2/3

#CONCATENATE ALL OUTPUT DATA AND PRINT TO FILE
```

```
        data = np.concatenate((STRESS, sig_von, sig_h, T ,
               E11 ,E22 ,E33, Eeq), axis=None)
        D =  np.array(data).reshape((1,13))
        np.savetxt(fout, D, delimiter=' ')
    fout.close()

#TOC
END = timer()
print "TIME ELAPSED=" , END-START
```